Development of FPGA controlled diagnostics on the MAST fusion reactor

BILLY KIAT HUANG

HUANG, BILLY KIAT (2013) Development of FPGA controlled diagnostics on the MAST fusion reactor. Doctoral thesis, Durham University.

Durham University

Development of FPGA controlled diagnostics on the MAST fusion reactor

by Billy Huang

A thesis submitted for the degree of
Doctor of Philosophy

in the
Centre for Advanced Instrumentation
Department of Physics

September 2013

Declaration of Authorship

I, Billy Huang, declare that this thesis titled:

"Development of FPGA controlled diagnostics on the MAST fusion reactor" and the work presented in it are my own. I confirm that:

- This work was done wholly or mainly while in candidature for a research degree at this University.
- Where any part of this thesis has previously been submitted for a degree or any other qualification at this University or any other institution, this has been clearly stated.
- Where I have consulted the published work of others, this is always clearly attributed.
- Where I have quoted from the work of others, the source is always given. With the exception of such quotations, this thesis is entirely my own work.
- I have acknowledged all main sources of help.
- Where the thesis is based on work done by myself jointly with others, I have made clear exactly what was done by others and what I have contributed myself.

Signed: Billy Huang

Date: 9th December 2013

UNIVERSITY OF DURHAM

Abstract

Centre for Advanced Instrumentation
Department of Physics

Development of FPGA controlled diagnostics on the MAST fusion reactor

by

Field Programmable Gate Array technology (FPGA) is very useful for implementing high performance digital signal processing algorithms, data acquisition and realtime control on nuclear fusion devices. This thesis presents the work done using FPGAs to develop powerful diagnostics. This has been achieved by developing embedded Linux and running it on the FPGA to enhance diagnostic capabilities such as remote management, PLC communications over the ModBus protocol and UDP based ethernet streaming. A closed loop real-time feedback prototype has been developed for combining laser beams onto a single beam path, for improving overall repetition rates of Thomson Scattering systems used for plasma electron temperature and density radial profile measurements. A controllable frequency sweep generator is used to drive the Toroidal Alfvén Eigenmode (TAE) antenna system and results are presented indicating successful TAE resonance detection. A fast data acquisition system has been developed for the Electron Bernstein Wave (EBW) Synthetic Aperture Microwave Imaging system and an active probing microwave source where the FPGA clock rate has been pushed to the maximum. Propagation delays on the order of 2 nanoseconds in the FPGA have been finely tuned with careful placement of FPGA logic using a custom logic placement tool. Intensity interferometry results are presented on the EBW system with a suggestion for phase insensitive pitch angle measurement.

Acknowledgements

I would like to thank many people for working with me during my 3.5 years of my PhD at Culham Centre for Fusion Energy. Firstly I must the two people who have taught me the most.

Dr. Graham Naylor has taught me an incredible amount about FPGAs, feedback control, signal processing, synchronous detection and so much more. I have pestered him on innumerable occasions on how to do such and such a thing and his ability to point out errors, such as seeing bytes swapped on a sine wave has no doubt saved me many grey hairs. He has given me much time and enthusiastically explained the answers to many interesting problems. He also has given me on multiple occasions given me biscuits and excellent coffee which greatly improved my FPGA coding abilities.

Dr. Vladimir Shevchenko has also taught me an incredible amount. He has been very patient with me, taking the time to explain things, in between my interruptions and has encouraged me to take my time, instead of jumping out of my seat to start work on something. Other valuable lessons include not getting too excited about results since they're probably not right, and on the slim chance they are, they've probably already been done before or not as exciting as I first thought. He also taught me that if I think something will take me 2 hours (like intensity interferometry), it can actually take me a year! He also provided me with multiple energy boosts in the form of cake (thank you Marina Shevchenko).

Many thanks to Professor Ray Sharples who has been an excellent supervisor and given me the right nudges at the right times, and especially for a fantastic effort in reviewing this thesis and substantially improving its quality. He has supported me throughout my whole PhD, in fact 2 months before I started, by encouraging me to intern at Fusion For Energy and also beyond the end of my PhD. I owe many thanks to Dr. Simon Freethy for many very interesting and useful daily coffee chats, about flying, synthetic aperture imaging, microwaves and much more. He has explained things to me very clearly and I have learned much from him. Thanks to Dr. Roddy Vann for encouraging me to join his project, I have really enjoyed working with him and the opportunity to work with FPGAs on the EBW SAMI system. My thanks also to Dr. Nizar Ben Ayed who worked with me on the TAE system and inspired me with his enthusiasm, can-do attitude and determination to see a project through, the results from these experiments would never have been gained without his great efforts. Thanks to Robert Stephenson and Stuart

Bray of the CCFE electronics department for teaching me much about electronics and helping me with much hardware. There are many more people I should thank and I list some names here, if I have neglected to acknowledge anyone here don't worry no one will read this. Thanks to Hyun Tae Kim, Tom O'Gorman, Jack Snape, Andy Allen, Llion Evans, Sarah Elmore, Lee Morgan, Lucy Wilson, Ed Hall, Richard Lake, Rory Scannell, Nigel Thomas-Davies, Brian Lloyd, Howard Wilson, Richard Myers, Kieran Gibson, Nigel Dipper, Sunita Khilar, Geof Cunningham, Sergei Sharapov, Sarah Newton and Twohedul Azam. I thank the MAST Team, CCFE, EPSRC and RCUK Energy. Ich möchte sagen danke für meine Liebe Marta Ludwiniak.

Contents

List of Figures

List of Tables

Abbreviations

ADC	**A**nalogue **D**igital **C**onverter
BES	**B**eam **E**mmision **S**pectroscopy
CLB	**C**onfigurable **L**ogic **B**lock
COTS	**C**ommercial **O**f **T**he **S**helf
DAC	**D**igital **A**nalogue **C**onverter
DDR	**D**ouble **D**ata **R**ate
DMA	**D**irect **M**emory **A**ddress
DSP	**D**igital **S**ignal **P**rocessing
EBW	**E**lectron **B**ernstein **W**ave
ECCD	**E**lectron **C**yclotron **C**urrent **D**rive
ECE	**E**lectron **C**yclotron **E**mission
ECRH	**E**lectron **C**yclotron **R**esonance **H**eating
FFT	**F**ast **F**ourier **T**ransform
FIR	**F**inite **I**mpulse **R**esponse
FMC	FPGA **M**ezzanine **C**onnector
FPGA	**F**ield **P**rogrammable **G**ate **A**rray
GAE	**G**lobal **A**lfvén **E**igenmodes
HBT	**H**anbury **B**rown **T**wiss
HCR	**H**olmes **C**auchy **R**iemann
HLS	**H**igh **L**evel **S**ynthesis
HPC	**H**igh **P**in **C**ount
ICRH	**I**on **C**yclotron **R**esonance **H**eating
IIR	**I**nfinite **I**mpulse **R**esponse
II	**I**ntensity **I**nterferometry
IO	**I**nput **O**utput

I	**I**nphase
JET	**J**oint **E**uropean **T**orus
LFSR	**L**inear **F**eedback **S**hift **R**egister
LHCD	**L**ower **H**ybrid **C**urrent **D**rive
LO	**L**ocal **O**scillator
LPC	**L**ow **P**in **C**ount
LUT	**L**ook **U**p **T**able
MAST	**M**ega **A**mp **S**pherical **T**okamak
MC	**M**ode **C**onversion
MHD	**M**agneto**h**ydro**d**ynamics
NBI	**N**eutral **B**eam **I**njection
NIB	**N**eutral **I**njection **B**eam
NTM	**N**eoclassical **T**earing **M**ode
PLC	**P**rogrammable **L**ogic **C**ontroller
PUCF	**P**erformance **U**ser **C**onstraints **F**ile
QPD	**Q**uadrant **P**hoto **D**iode
Q	**Q**uadrature
RMS	**R**oot **M**ean **S**quare
SAI	**S**ynthetic **A**perture **I**maging
SAMI	**S**ynthetic **A**perture **M**icrowave **I**maging
SBS	**S**ide **B**and **S**eparation
SNR	**S**ignal to **N**oise **R**atio
SSB	**S**ingle **S**ide **B**and
TAE	**T**oroidal **A**lfvén **E**igenmode
TCP	**T**ransmission **C**ontrol **P**rotocol
TFTP	**T**rivial **F**ile **T**ransfer **P**rotocol
TS	**T**homson **S**cattering
UCF	**U**ser **C**onstraints **F**ile
UDP	**U**ser **D**atagram **P**rotocol
VCZ	**V**an **C**ittert **Z**ernike
VHDL	**V**erilog **H**ardware **D**escription **L**anguage
XPS	**X**ilinx **P**latform **S**tudio

For Dad

Preamble

Every form of life is engaged knowingly or unknowingly in the quest to reverse the seemingly universal order of increasing entropy (also referred to as disorder or randomness). Life needs energy in this ongoing quest. With this mysterious quantity crustaceans can turn randomly ordered solutions of sodium carbonate into highly structured shells, some of which follow a mathematical constant known as the golden ratio. Energy allows continents to form mountains; bacteria to propel themselves with their flagellum; clouds of interstellar gas inconvievably vast to collapse, over the incredibly long time scales into stars, planets and objects at the boundaries of our comprehension. Energy is what drives this creation and destruction and one thing is clear: that the most abundant fuel in the universe is hydrogen. The stars formed from this fuel a long time ago. Over billions upon billions of years they slowly heated up and began to glow whilst they sucked up surrounding hydrogen crushing and heating in their core to temperatures over ten hundred million degrees. Our own sun has for billions of years beamed a steady power of 10^{26} Watts, enough power to boil all the water on earth in under 1.5 seconds [1] . Just think about that next time you put on the kettle!

As the stars did this they gave out radiation which we perceive this as light and heat. We appreciate this when we see the stars, and during the day as we look at the sun. We cannot exist without the light and heat from our nearest star the sun and in fact if we look even further back in time we would find that the very atoms that make up our bodies, such as carbon, nitrogen, oxygen and iron were all made in the nuclear furnances at the centres of stars and that was all powered by hydrogen. We are in essence all made of nuclear waste, however it is far more romantic to refer to ourselves as being comprised of star dust. There is a clear distinction when considering nuclear waste - that which is radioactive and produces high energy particles and radiation that damages the fragile ensemble of proteins, molecules and many other components comprising the cells of our bodies. This leaves the other waste, the non-radioactive elements that are stable and make up everything that we are familiar with, carbon, oxygen, nitrogen and everything else which we can see, in what is known as the periodic table. We worry about radioactive nuclear waste but embrace non-radioactive nuclear waste, which is the material which we and everything we make and use is made of. But how do we get rid of radioactivity? Or better still can we avoid it completely?

All stable elements have their radioactive counterparts, even carbon which makes up organic life. That radioactivity can be useful for dating ancient fossils using carbon

---

[1] Incident solar power area density at top of atmosphere is 1.37 kW/m^2 which means the solar power output is 3.9×10^{23}kW. Earth's mass of water is 1.34×10^{21} kg. The heat capacity of water is 4.2 kJ/kG/K. The time to boil all of Earth's water is given by the equation: Time = Mass × 4.2 × 100 / Power = $1.34 \times 10^{21} \times 4.2 \times 100/(3.9 \times 10^{23}) = 1.44$ seconds.

dating. Over time, depending on the element, radioactive elements decay on timescales ranging from fractions of a second to times significant when compared to the age of the universe. Radiocative decay eventually converts elements from unstable states to new stable elements. Modern nuclear reactors burn fuel which is semi-stable, in that with the right amount of kick it can spontaneously form a chain reaction releasing huge quantities of energy but at the same time splitting the atoms of the fuel into smaller radioactive pieces. It is these pieces that can remain for hundreds of thousands of years unless appropriately dealt with. This is fission. The energy of the stars burns hydrogen creating heavier elements. This is fusion.

The difference between fusion and fission is like the difference between marriage and divorce. They may come from the same phenomenon, but they are opposites. Fusion is marriage of hydrogen to atoms to other hydrogen atoms. Fisson is the splitting of larger atoms. There is an ongoing debate about whether fusion or fission is fundamentally better for mankind. Of course this always depends on who you ask, and there are people who say fusion is impossible. I would say those people to go out one night on a clear night and take a long look up into the sky at all the beautiful, bright, burning fusion reactors. The dream is limitless energy using clean fuel with low level waste that is below background levels after 100 years.

Chapter 1

Introduction

1.1 What is fusion?

What is fusion? It is the joining of lighter atoms (such as hydrogen) to create heavier atoms (such as helium) releasing energy in the process. This process is a nuclear reaction. It is cleaner than fission but much harder to do. There are many different machines attempting to take advantage of different physical phenomena and reactions. All of these approaches have their own unique and valid contributions to the mission, which is to achieve a fusion power plant. The way fusion is done now, may be very different in a hundred years from now, as technology has evolved so have our approaches. This thesis focuses on the Tokamak, the type of machine where most money is spent in fusion research. To be more exact, most of fusion research money is in fact now being spent on one machine, ITER in Cadarache, France. Humankind's costliest terrestrial research project, a Tokamak designed to output ten times its input energy. This is an ambitious goal, and if achieved a gigantic step towards commercial fusion power.

Fusion research began in earnest in Britain in 1957 with the operation of the ZETA device. Later the Tokamak was developed, the first of which was led by Lev Artsimovich at the Kurchatov Institute, Russia in 1956. The year is now 2012, over 60 years later and for me the first questions were: why has it taken so long? is it worth me contributing? and if so what can I contribute?

Fusion research needs to cross a formidable barrier, one of the greatest barriers in the universe, the Coulomb barrier. It is this that stops atoms from collapsing in on each other. Thankfully this barrier exists or our universe would probably not support life. When it comes to fusion however we need break this barrier, we need the atoms to collide with sufficient energy and sufficiently often. So how can this be done? We can increase the temperature of the atoms so much so that they become plasma and more energetic. We can put more of these in a smaller place so that the plasma density increases. We can increase the amount of time that the plasma nuclei spend colliding into each other. These are three crucial parameters: temperature, density and confinement time. The product of which unsurprisingly is called the triple product (see Fig. 1.4) is a measure Tokamak performance. Over the decades this value has increased over 10,000,000 fold and with it the potential for success in reaching fusion power. It has taken so long because it has taken this amount of time to achieve these impressive gains. In 1997 JET suceeded in generating 16MW of fusion power. In the 2020's ITER aims to generate 500MW of fusion power which will demonstrate to the world that fusion is approaching reactor scale power.

The modern tokamak is an intriguing device simple in its fundamental design and complemented by a complex array of heating and diagnostic systems. Systems can have such a rich history of design and expertise that they are evolving experiments in their own right. Whilst the goal of fusion power must be to create a fusion power plant it is clear that there is rich field of research for almost any researcher or engineer to be involved. Such a diverse field with a clear mission led me to begin the journey of a contribution to this great endeavour.

1.2 Fusion physics

1.2.1 Calculating fusion power

The key measurable in fusion is the power that a fusion reactor can produce. Here I present some fundamental and well known theory [7] but using improved cross section formulae [8]. This fundamental measurement should be understood by any researcher and in particular helps the researcher to understand the dependence of parameters that a device depends on, in order to get out the most fusion power.

Fusion occurs when the coulomb barrier is overcome between two light nuclei fusing to form a heavier element and releasing energy. To measure the energy being released in a fusion device it is necessary to know the reaction rate. The scattering cross section (σ) of a reaction type is a measure of the probability of a reaction occuring (see Fig. 1.1) and thus a key component of the reaction rate.

Formally the reaction rate at relative velocity (v') per unit volume between two particle species is defined as:

$$\sigma(v')v'f(v') \tag{1.1}$$

The relative velocity distribution $f(v')$ allows us to simply write the above equation as:

$$\sigma(v')v'f(v_1,v_2) = \sigma(v')v'f(v_1)f(v_2) \tag{1.2}$$

Where $v' = v_1 - v_2$, σ is the cross section and $f(v_j)$ is the species velocity probability distribution. This equation definition is formed by contemplating the factors which affect the rate of reaction between two different species with random independent velocity probability distributions.

In plasma the ions will quickly reach thermal equilibrium due to their high collision rate compared to the time scales of injected power and particle loss. However the collision rate between the species is assumed to be low enough and consistent with the assumption of random independent velcocity probability distribution functions. Therefore their velocity distribution is Maxwellian in Magnetic Confinement Fusion (MCF).

The Maxwellian velocity distribution is:

$$f_j(v_j) = n_j\left(\frac{m_j}{2\pi T}\right)^{3/2} e^{-E_j/T} \tag{1.3}$$

Note that often kT is omitted and T is shown instead. The total reaction rate per unit volume is the integral over all velocities:

$$R = \int\int \sigma(v')v'f_1(v_1)f_2(v_2)d^3v_1d^3v_2 \tag{1.4}$$

This integration can be solved by a transformation of variables using the reduced mass method. $\mu = m_1m_2/(m_1+m_2)$:

$$R = 4\pi n_1n_2\left(\frac{\mu}{2\pi T}\right)^{3/2}\int \sigma(v')v'^3 exp\left(-\frac{\mu v'^2}{2T}\right)dv' \tag{1.5}$$

The reaction rate can then be re-written in terms of the energy of a bombarding particle:

$$\epsilon = \frac{1}{2}m_1v'^2 \tag{1.6}$$

Giving:

$$R = \left(\frac{8}{\pi}\right)^{1/2} n_1 n_2 \left(\frac{\mu}{T}\right)^{3/2} \frac{1}{m_1^2} \int \sigma(\epsilon)\, \epsilon\, exp\left(-\frac{\mu\epsilon}{m_1 T}\right) d\epsilon \tag{1.7}$$

1.2.2 Ignition

The charged reaction products of the reaction energy and can be confined within the magnetic fields of the tokamak. This means the charged reaction products will heat the fuel. This reduces the need for external heating. Given the correct reactor configuration the power loss will be balanced by the power produced. In the same way you can light a piece of coal with a blowtorch, but once it is burning you can remove the blowtorch and it will burn itself. This is called ignition.

A self-sustaining nuclear reaction occurs when the internally generated power is greater than the power lost:

$$P_{th} > P_{loss} \tag{1.8}$$

The power lost is related to the amount of energy stored in the plasma:

$$\tau_E = \frac{W}{P_{loss}} = \frac{3n_e T}{P_{loss}} \tag{1.9}$$

Where $W = 3n_e T$. The thermonuclear power $P_{th} = R\xi$. $R = n_1 n_2 \langle\sigma v\rangle$ is the cross section integrand (see Fig. 1.2), and n_j is the density of the particle species. Considering fractional densities, $n = n_1 + n_2$. The fusion power is maximised with a 50%/50% mixture, so $P_{th} = \frac{1}{4} n^2 \langle\sigma v\rangle \xi$. Assuming electrical neutrality $n_e = n$.

Where ξ is the energy of the charged fusion reaction products which can contribute to the heating of the plasma.

$$\frac{1}{4} n^2 \langle\sigma v\rangle \xi \geq \frac{3nT}{\tau_E} \tag{1.10}$$

1.2.3 Lawson criterion

This power balance leads to the Lawson criterion, a useful measure of the ignition condition for different fusion reactions:

$$n\tau_E \geq \frac{12}{\xi} \frac{T}{\langle\sigma v\rangle} \tag{1.11}$$

Figure 1.3 and Table 1.1 show the lawson criterion for the different fusion reactions.

1.2.4 Triple product

Another useful indicator to the ignition condition is the triple product. The temperature and density can vary over a large range. However since $P \propto nT$ by including the factor of T, the triple product is now additionally a function of the physical quantity pressure which makes the equation applicable to a wider range of devices and therefore a more useful measure of the ignition requirement:

$$nT\tau_E \geq \frac{12}{\xi}\frac{T^2}{\langle \sigma v \rangle} \tag{1.12}$$

Figure 1.4 and Table 1.2 show the triple product for the different fusion reactions.

1.2.5 Key fusion reactions

$$\mathrm{D}_1^2 + \mathrm{T}_1^3 \rightarrow \mathrm{He}_2^4 + \mathrm{n}_0^1 \tag{1.13}$$

^{4}He: 3.5 MeV, n: 14.1 MeV

$$\mathrm{D}_1^2 + \mathrm{D}_1^2 \rightarrow \mathrm{T}_1^3 + \mathrm{p}_1^1 \tag{1.14}$$

50% T: 1.01 MeV, p: 3.02 MeV

$$\mathrm{D}_1^2 + \mathrm{D}_1^2 \rightarrow \mathrm{He}_2^3 + \mathrm{n}_0^1 \tag{1.15}$$

50% ^{3}He: 0.82 MeV, n: 2.45 MeV

$$\mathrm{D}_1^2 + \mathrm{He}_2^3 \rightarrow \mathrm{He}_2^4 + \mathrm{p}_1^1 \tag{1.16}$$

^{4}He: 3.6 MeV, n: 14.7 MeV

For 50%/50% D-T, 20% of the alpha energy is electrically charged and magnetically confined heating the fuel and 80% of the energy is given to neutrons which escape and heat the blanket.

The nuclear cross sections here uses Xing Li's 3 parameter formula [8] which has been proven to be better than the Naval Research Laboratory's 5 parameter formula [9] giving improved estimates of fusion reaction cross sections.

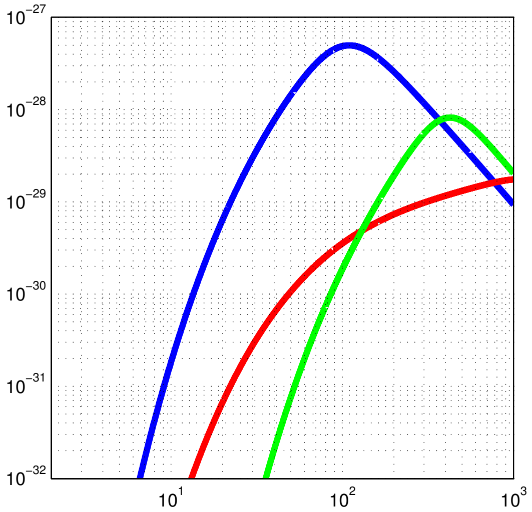

FIGURE 1.1: The scattering cross section. $\sigma(\varepsilon)$ (m^2) vs. T (keV). D-T (blue), D-D (red) and D-^{3}He (green).

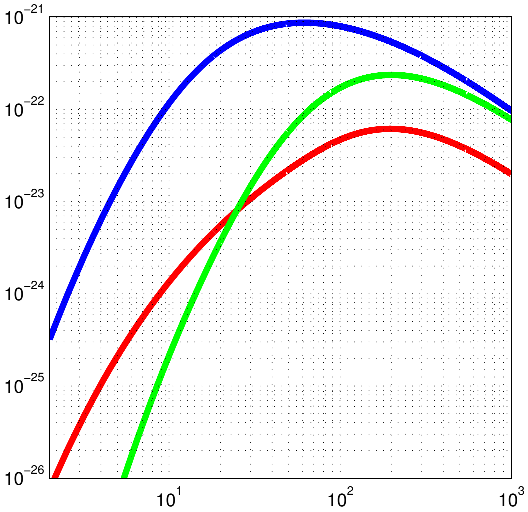

FIGURE 1.2: The cross section integrand where $R = n_1 n_2 \langle \sigma v \rangle$. $\langle \sigma v \rangle$ $(m^3 s^{-1})$ vs. T (keV). D-T (blue), D-D (red) and D-^{3}He (green).

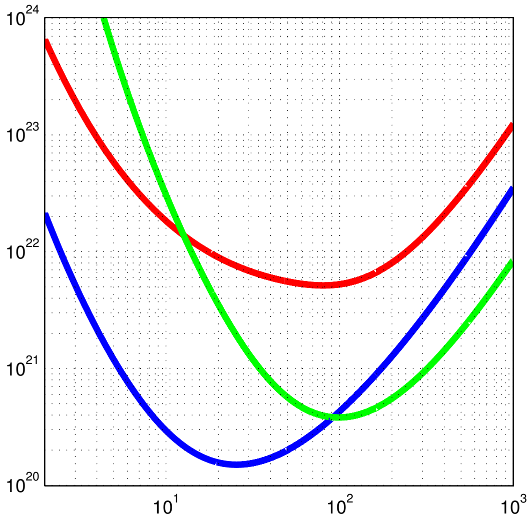

FIGURE 1.3: The Lawson criterion. $n\tau_\varepsilon$ (s/m^3) vs. T (keV) D-T (blue), D-D (red) and D-^{3}He (green).

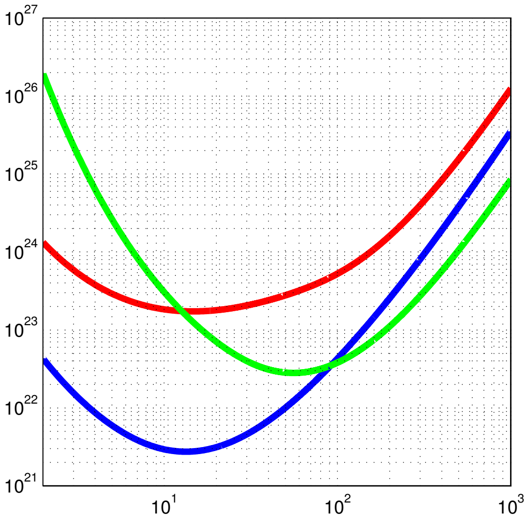

FIGURE 1.4: The triple product. $nT\tau_\varepsilon$ (keV s/m^3) vs. T (keV) D-T (blue), D-D (red) and D-^{3}He (green).

TABLE 1.1: Lawson Criterion

	D-T	D-D	D-^{3}He
$n\tau_\epsilon$(s/m^3)	1.50×10^{20}	5.15×10^{21}	3.81×10^{20}
T_{min} (keV)	25.4	80.4	98.6

Table 1.2: Triple Product

	D-T	D-D	D-^{3}He
$nT\tau_\epsilon$(keV s/m^3)	2.74×10^{21}	1.73×10^{23}	2.81×10^{22}
T_{min} (keV)	13.4	14.7	55.8

1.3 Power producing reaction

It has been shown and is well known that the D-T ignition condition is much easier to achieve and occurs at a lower temperature, 25.4 keV according to the Lawson criterion and 13.4 keV according to the triple product.

1.4 Abundance of fuel

Deuterium is available in great abundance in the universe and we have a virtually inexhuastible (more than millions of years) supply on earth. Tritium does not naturally occur in nature due to its short half life (12.3 years). However Tritium can be created in a reactor from Lithium which is also in plentiful supply on earth.

Tritium is a strictly controlled nuclear material and has special handling requirements due to it's 12.3 year half-life. In a tokamak reactor D-T is the reaction that will be used for sustained fusion energy generation. In research it is much more common that Deuterium is used 100% rather than a 50%/50% Deuterium/Tritium mix.

It is the abundance of fuel and lower radioactivity than fission means that if fusion can be harnessed economically it would solve humanities energy needs for at least the next millenia.

1.5 The Tokamak

A tokamak is one type of magnetic confinement fusion device. It constists of three primary sets of coils. The solenoid coil (Figure 1.5), the toroidal field (TF) coils (Figure 1.6), and the poloidal field (PF) coils (Figure 1.8). The TF and PF are ideally driven by a constant current. The solenoid coil is designed to produce a current in the plasma. The solenoid does this by acting as the primary winding on a transformer and the plasma acting as the secondary. However in order for this to occur a changing current needs to run through the solenoid which means that a tokamak is inherently a pulsed device. Increasingly more research is looking at bulding reactors without a solenoid. Instead of a solenoid different methods for current drive are being investigated to avoid using a solenoid thus making the device continually current driven and non-pulsed.

Advances to Tokamaks can use superconducting coils to increase the field strength and therefore confinement time of the plasma and supercapacitors to increase the pulse lengths.

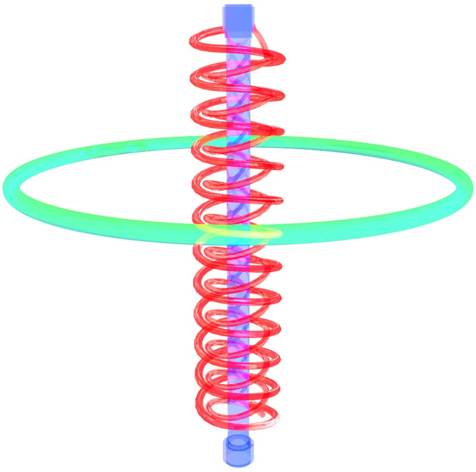

FIGURE 1.5: Solenoid coil. The large green ring represents the induced plasma current.

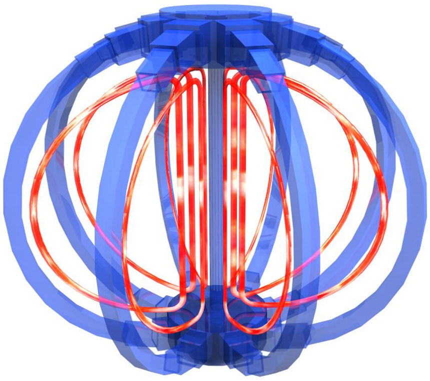

FIGURE 1.6: Toroidal Field (TF) coils

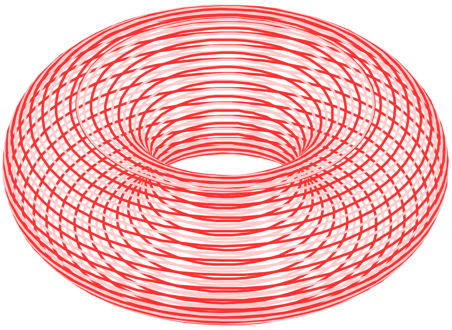

FIGURE 1.7: Toroidal Field

1.5.1 Path to fusion

The path to fusion has been and continues to be a difficult road largely due to the technological hurdles, lack of political motivation, foresight, economics and public awareness. We are trying to secure humanities energy needs for the forseeable future, which is no small feat. But we are making good progress and ITER (Figure 1.10) will demonstrate up to 500 MW of fusion power.

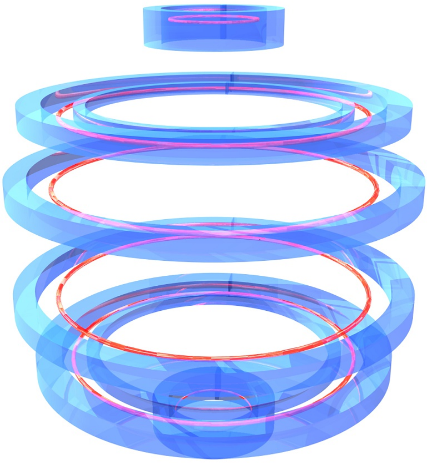

FIGURE 1.8: Poloidal Field (PF) coils

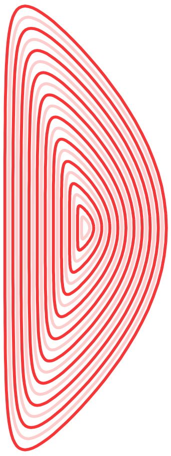

FIGURE 1.9: Poloidal flux surfaces

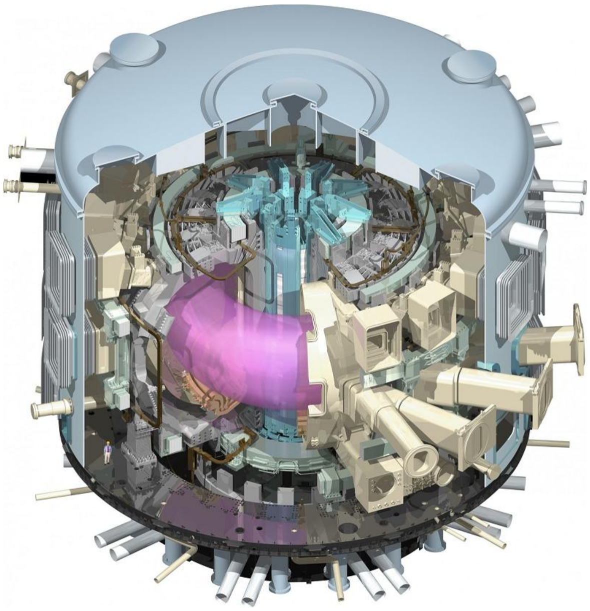

FIGURE 1.10: ITER vessel cutaway.

1.6 Other fusion devices

The are many other fusion devices and the small amount of space used to mention them here is by no means representative of the relative research investement or potential in comparison to tokamaks. Other magnetic devices include stellerators, reverse field pinches, laser intertial confinement fusion (NIF, LMJ).

1.7 The Mega Amp Spherical Tokamak (MAST)

This is the machine on which I have done most of my research. A spherical tokamak has a higher aspect ratio ($a = r/R$, see Fig. 4.8). These type of tokamaks have a higher beta which is the ratio of plasma to magnetic pressure.

$$\beta = \frac{P_{\text{plasma}}}{P_{\text{magnetic}}} = \frac{nk_BT}{B^2/2\mu_0} \tag{1.17}$$

Beta is broadly speaking a measure of economic efficiency, so potentially spherical tokamaks are more economic than lower aspect ratio tokamaks.

Table 1.3: Example MAST Parameters [5, 6]

Parameter	**Value**
Plasma Current	1 MA
Major radius	0.85 m
Minor radius	0.65 m
Plasma radius	1.4 m
Toroidal field at major radius	.52 T
Pulse length	0.5 s
NBI power	3.3 MW
Density (n)	$2 \times 10^{19}/\text{cm}^3$
Temperature (T)	1.5 keV
Neutron yield	10^{14} n/s
Q ($P_{\text{in}}/P_{\text{neutron}}$)	10^{-4}

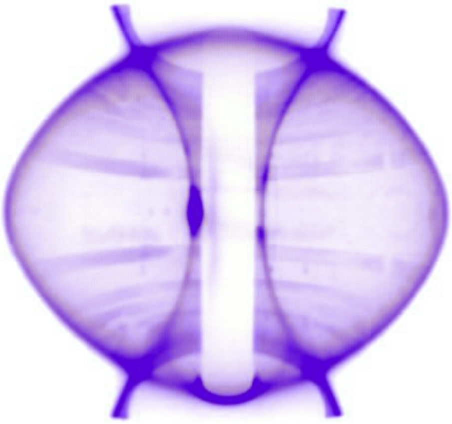

Figure 1.11: An example MAST plasma. The "tin can" shape of the MAST vessel allows a wide angle view.

1.8 Content of the thesis

The thesis covers developments of real-time systems applied to fusion tokamaks. I mention only briefly here that an FPGA (Field Programmable Gate Array) is a component of the real-time systems which I have assisted in developing and these devices will be discussed in detail. Details are given on the hardware and software development of three systems. Results from the TAE (see Ch. 4) system and simulations of the EBW array (see Ch. 5) are discussed. The reader would benefit from having a basic understanding of tokamak physics, real-time control, digital signal processing, Thomson scattering, toroidal Alfvén eigenmodes, electron Bernstein waves and interferometry.

1.8.1 Chapter 2: FPGA System Development.

This chapter introduces the FPGA systems on MAST followed by the various tools for FPGA development. Embedded Linux on FPGAs is discussed including tests performed on systems developed during the thesis. Improving system accessibility and remote management using embedded Linux is also mentioned. The chapter ends with a section on future developments including the capability to program FPGAs with C/C++ code.

1.8.2 Chapter 3: Laser Beam Combiner Prototype for ITER Thomson Scattering.

The goal of this project was to implement a closed loop FPGA feedback control of a laser reflected from a mechanical scanning mirror at 67 Hz and investigate the achievable microradian pointing stability. After the FPGA system was developed a pointing stability much below the required pointing stability was achieved and demonstrated the capability to combine multiple lasers onto a single beam path for ITER (and other tokamaks) to increase the overall repetition rate.

1.8.3 Chapter 4: Toroidal Alfvén Eigenmode (TAE) Antenna.

The goal of the project was to excite TAE modes within the plasma for which very good evidence has been obtained. The TAE antenna diagnostic is a complex system and there were significant challenges in implementing the hardware. The primary result was to detect a signal increase due to the plasma, which is in itself is a good achievement and the first such confirmed results on MAST.

1.8.4 Chapter 5: Electron Bernstein Wave (EBW) Microwave Imaging.

The goal of this project was two fold: To implement a record breaking continuous streaming systeam using FPGAs and data acquisition software, and to reconstruct a picture of the plasma using intensity intereferometry. A comparison is presented between different image reconstruction methods. It was found that the eight antenna system is not enough to obtain a pitch angle measurement using intensity information alone, but that a future system based on 16 antennas would be sufficient, provided the plasma emission is two bright windows as the EBW theory predicts.

1.9 Publications

A list of publications completed during the work of this thesis can be found in Appendix C.1.

Chapter 2

FPGA System Development

2.1 Introduction

This chapter will introduce Field Programmable Gate Arrays (FPGAs) (see Fig. 2.1) and the applications to projects on MAST which are in progress or have been completed between 2010-2013. A description is given of the tools used for FPGA development and the usefulness of hardware standards. The difference between soft and hard processors is described and the benefit of running embedded linux on such processors. Using embedded linux is useful for remote configuration, operation and maintenance of FPGA systems and some examples are provided. Future FPGA technology developments are discussed with emphasis on programming FPGAs with C/C++ code.

There are many different technologies for doing real-time feedback. A few will be discussed with their advantages and drawbacks. Programmable Logic Controllers (PLCs) are used extensively in many industries and can be found in places such as factories and power plants. They are good for their reliability, long term support and wide availability but are lacking in their speed. This can depend on the protocol used for communication ($\sim$100 Hz for ModBus $\sim$1 kHz for EtherCAT). GPUs are good for doing parallel floating point calculations at high speed (GHz) however they are generally limited in their ability to interface to "the real world" through digital and analogue I/O. This means that they have mainly been applied in running optimised algorithms to provide dramatic speed up of code that would traditionally run on a PC, such as particle simulations. Real-time operating systems use interrupts to force the processor to execute important code as quickly as possible, which provides lower latency response times. Their main benefit is the ability to use standard programming code (such as C) and tools for real-time algorithms. One drawback is that for a heavily loaded system processing multiple interrupts the latency of a process can increase.

In all of the cases mentioned so far, the systems do not have a deterministic latency and therefore closed loop cycle times. Deterministic latency and cycle time is one of the primary benefits of an FPGA. Logical behaviour can be precisely defined, and circuitry can be driven by multiple clocks. Additionally interfaces to the real-world are well developed and can operate at very high speed (GHz). An FPGA is also capable of significant parallel processing capability with the largest (as of 2013) chips capable of 10^{12} Multiply-Accumulates (MACs) a second. Additionally some areas of the FPGA chip, such as serial transceivers operate at multi gigabit per second rates. The drawback with FPGAs is that much of the chip will run at lower speeds (∼200 MHz) than a CPU or GPU and programming them can require a significant learning curve, however there are graphical tools (such as System Generator) that allows simple systems to be developed with relative ease. Overall however compared to the other mentioned systems, the benefits of FPGAs outweigh the drawbacks of many other systems, particularly in the field of fusion diagnostics. For systems using waveforms for control (see Chapter 3 or Chapter 4) FPGAs are useful . For some high performance systems (see Chapter 5) FPGAs are a necessity.

2.2 FPGAs on MAST

2.2.1 FPGA usage in fusion

Field Programmable Gate Arrays (FPGAs) are reconfigurable hardware that are increasingly being used in fusion (see Table 2.1). An essential element is the configurable logic block (CLB, see Fig. 2.2) that contains a lookup table (LUT). For example consider two inputs which are two bits (say X, Y) which can select one of four outputs (say A, B, C, D). If we set A=0, B=0, C=0, D=1 then we have programmed the result of the LUT as an AND gate (X & Y). Any logical behaviour can be programmed this way. The next key functionality is the ability to route inputs to outputs and vice versa using routing (see Fig. 2.3).

FPGAs can be used to process large amounts of digital information and for input/output processing. Typical examples include logic for reading analogue to digital converters (ADCs) and digital signal processing (DSP) such as fast Fourier transforms (FFTs), matrix multiplication and digital filters. Additionally lookup tables can be loaded for waveform generation and other applications where different arrays of coefficients are needed.

Table 2.1: FPGAs in fusion.

Reference	**Machine**	**Description**
[10]	Tore Supra	Monitoring of infrared radiation on high flux targets controlling injected heating power or radiation cooling
[11]	NSTX	Clock distribution and 1 MHz time base to encode system and plasma events
[12]	KSTAR	Time synchronization system
[13]	Alcator C-Mod	Hard X-ray diagnostic upgrade
[14]	ASDEX Upgrade	Data acquisition
[15]	JET	Image processing for hot spot detection
[16, 17]	HBT-EP	Feedback suppression of external MHD modes
[18]	MAST	Synchronisation of TS measurements
[19]	JT-60SA	Supervisory control system
[20]	TEXTOR	Plasma stabilisation
[21]	EAST	Upgrade of the distributed synchronization and timing system
[22]	TJ-II	Continuous plasma density with infrared interferometery

Fusion diagnostics can make use of FPGAs by taking advantage of their fast speeds. It is possible to purchase ADCs and DACs which operate into the GS/s regime. They can be used for real-time data acquisition of high speed ADCs and real-time triggering. Real-time acquisiton from plasma diagnostic instruments allows action in real-time such as for real-time triggering, control of plasma actuators (e.g. coil currents, heating, etc.) and protection interlocks for plant protection and safety.

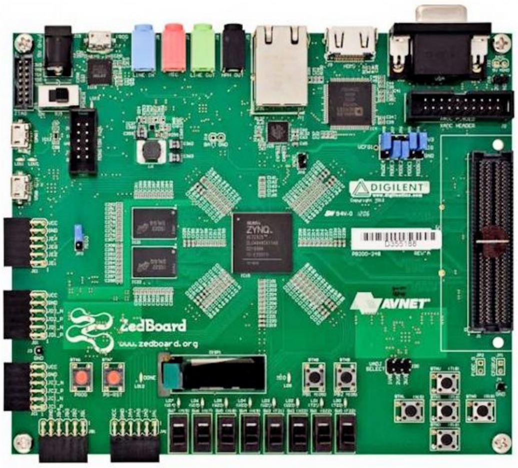

Figure 2.1: An example of an FPGA board (Zedboard). The FPGA is the chip in the centre (Xilinx ZYNQ) which is connected to all of the board hardware components.

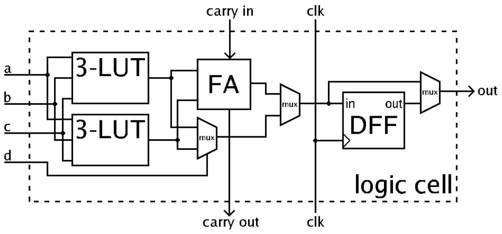

FIGURE 2.2: An example of a configurable logic block (CLB), a fundamental element of an FPGA. Credit: Peter Källström.

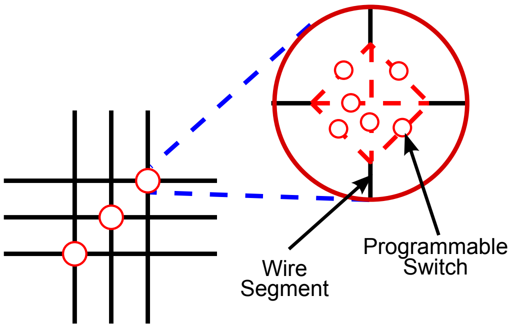

FIGURE 2.3: An example of a routing logic. Credit: Ed Stannered.

2.2.2 Projects on MAST

A large number of projects have been started and many completed on MAST using FPGAs during this thesis. Some of the projects listed below have been developed in conjunction with different team members, many of the projects have been developed solely with the work completed during the thesis and all of the projects have at least had some input from the research of this thesis, varying from the use of embedded Linux to development tools. The first 3 projects listed in Table 2.2 have their own dedicated chapter.

TABLE 2.2: MAST FPGA Projects

Project	**Status**	**Chapter**
ITER Laser Beam Combiner Prototype	Completed	Ch. 3
TAE Diagnostic	Completed	Ch. 4
EBW Microwave Imaging	Completed	Ch. 5
Vertical Stabilisation	Completed	
Thomson Laser Triggering	Completed	
Fast Timer	Completed	
1/10 MHz Clock Distributor	Completed	
Bolometer Upgrade	MAST Upgrade	
Interferometer Upgrade	MAST Upgrade	
Machine Protection	MAST Upgrade	
Event Timer	MAST Upgrade	
LEM TF Voltage Monitor Prototype	MAST Upgrade	

2.3 FPGA development

2.3.1 Firmware

One output of any FPGA project is firmware, sometimes referred to as intellectual property (or IP Cores). Firmware is the compiled logic code that is loaded into the FPGA which defines all the logical interconnections for the FPGA to perform its desired digital operations (such as signal processing and timing). The firmware can be developed using low level or high level tools (Figure 2.4). Low level tools provide a basic text based interface in which VHDL and Verilog code can be written. In general this should be avoided except in cases where the developer is accustomed to working at the code level for wrapping together high level "blocks" or where clock control is needed. High level tools provide schematic representations of logic blocks that can be joined to describe the overall system digital logic and can hugely simplify the process of developing a complex design.

2.3.2 Development tools

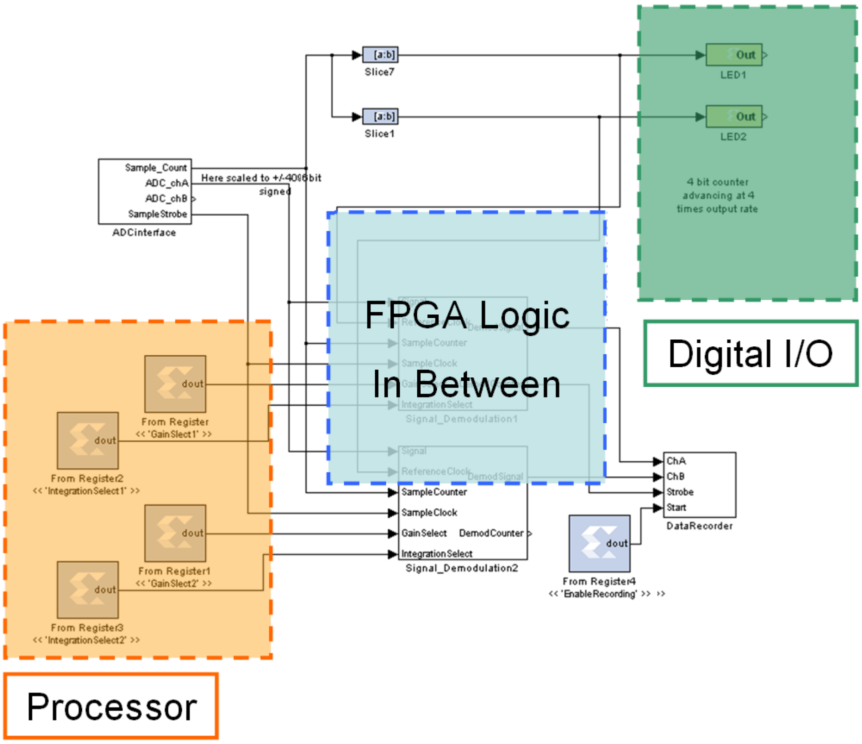

Figure 2.4: High level graphical FPGA programming tools.

High level graphical FPGA programming tools such as Xilinx System Generator and Altera DSP Builder help eliminate or reduce the need to write logic in Hardware Description Language (HDL) or Verilog. These tools greatly simplify the design of logic systems by using blocks which can perform complex signal processing operations in the Simulink environment of MATLAB. In addition these tools can be used to easily create a logic interface between FPGA logic and digital I/O of an embedded processor (such as the MicroBlaze or Nios) using registers or shared memory. For example the processor can be used to control the gain of an ADC or the signal of a waveform generator.

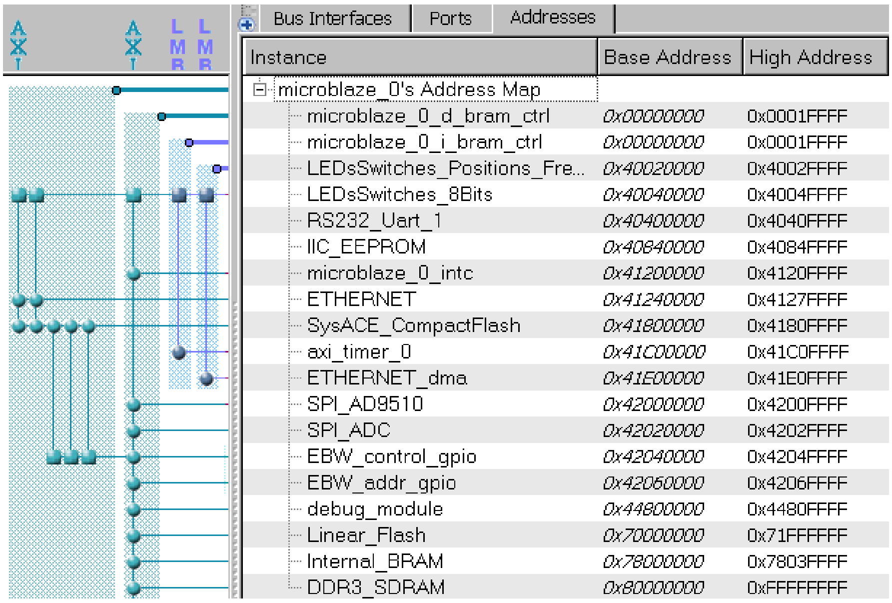

Instance	Base Address	High Address
microblaze_0's Address Map		
microblaze_0_d_bram_ctrl	0x00000000	0x0001FFFF
microblaze_0_i_bram_ctrl	0x00000000	0x0001FFFF
LEDsSwitches_Positions_Fre...	0x40020000	0x4002FFFF
LEDsSwitches_8Bits	0x40040000	0x4004FFFF
RS232_Uart_1	0x40400000	0x4040FFFF
IIC_EEPROM	0x40840000	0x4084FFFF
microblaze_0_intc	0x41200000	0x4120FFFF
ETHERNET	0x41240000	0x4127FFFF
SysACE_CompactFlash	0x41800000	0x4180FFFF
axi_timer_0	0x41C00000	0x41C0FFFF
ETHERNET_dma	0x41E00000	0x41E0FFFF
SPI_AD9510	0x42000000	0x4200FFFF
SPI_ADC	0x42020000	0x4202FFFF
EBW_control_gpio	0x42040000	0x4204FFFF
EBW_addr_gpio	0x42060000	0x4206FFFF
debug_module	0x44800000	0x4480FFFF
Linear_Flash	0x70000000	0x71FFFFFF
Internal_BRAM	0x78000000	0x7803FFFF
DDR3_SDRAM	0x80000000	0xFFFFFFFF

FIGURE 2.5: Setting the register addresses on the processor bus.

The interface for setting processor register and memory addresses in Xilinx Platform Studio (XPS) allows read/write access by both the FPGA logic and processor (see Figure 2.5). These register and memory addresses are then directly written to using pointers in a C/C++ (or other language) program which is then compiled with embedded Linux. This enables a program/service to directly drive the FPGA logic/IO and vice versa.

2.3.3 Standardisation

Standardisation of FPGA systems helps provide a set of tools to researchers and engineers on fusion devices which enable diagnostics, actuators and control systems to be easily produced, maintained and upgraded whilst not being costly. This can be done through a combination of using standard hardware (listed below) and standard development tools (section 2.3). There are still some open questions as to what are the best tools to cover the widest range of applications and with more research in the fusion FPGA community it is forseen that some of these questions can be answered. On MAST the Vita 57.1 FPGA Mezzanine Connector (FMC) standard has been used to enable the portability of different I/O mezzanine boards (such as DACs and ADCs) to different carrier boards with relative ease. The use of embedded Linux can also be considered a standard for controlling FPGA devices. Clearly some standards such as USB and Ethernet have stood the test of time and are likely to be around for a long time due to their ubiquitous usage in computing. It is evident that fusion will benefit from such standards by reducing the amount of work needed to port code to different hardware.

An FPGA system needs some basic components in addition to the FPGA in order to operate effectively: i) non-volatile storage space for firmware, ii) communication interface, iii) memory, iv) input/output (I/O), v) embedded Linux:

i **Non-volatile storage**: FLASH is a common choice for non-volatile storage , which can include chip sizes of above 2 GB. Although firmware is in the MB range this extra space can be useful for storing other information such as boot loaders, a Linux kernel and system configuration parameters.

ii **Communication interface**: Gigabit ethernet is an increasingly used communication interface. It is easily adapted into most existing network infrastructure. However where high data rates are needed PCI Express (PCIe) or 10GBASE-T may be a better solution. PCIe provides higher bandwidth (up to 128 Gbit/s) over shorter distances (<1m) and 10GBASE-T provides lower bandwidth (up to 10Gbit/s) over longer distances (100m). Aurora over SFP fibre provides high bandwidth (above 4 Gbit/s) over optical fibre with deterministic latency (370 ns has been demonstrated on MAST).

iii **Memory**: DDR RAM is high speed double-data rate memory, which reads/writes data on the rising and falling edges of the clock. FPGAs have the capability to drive logic at 400 MHz+ required for DDR3 chips or later generation memory chips.

iv **I/O**: The FPGA Mezzanine Carrier (FMC) is a high density FPGA specific I/O connector. Advantages include a very high pin count (up to 400 pins), 10 gigabit/s transceivers and high speed LVDS signalling. Additionally since it is an open standard it helps allow internal hardware support for control systems [23]. Disadvantages are that in lower acquisition rate situations, in order to acquire many analogue channels or control signals an additional break-out board is necessary. There is a limitation on the number of supply voltages provided by the standard (such as no

±15V) resulting in some mezzanine boards resorting to external power supplies via additional connectors.

v **Embedded Linux**: This is the only non-hardware component of the discussed standardisation. Linux is being used on FPGA systems for two reasons: It provides powerful infrastructure for expanding the capability of FPGA systems and it is well supported by both leading FPGA manufacturers: Xilinx and Altera.

2.4 Soft and hard processors

A soft processor resides within the configurable logic of the FPGA, where as a hard processor is contained in dedicated silicon. Generally a soft processor is ten times slower ($\sim$ 100 MHz) than a hard processor ($\sim$ 1 GHz). This sacrifice in speed is the result of having an optional, programmable and configurable processor. One such processor is the MicroBlaze, a 32-bit processor equipped with a Memory Management Unit (MMU) and therefore capable of running Linux. The main advantage of a soft processor over a hard processor is design portability. An FPGA design using a soft processor can be targeted to another FPGA therefore requiring only minimal changes (pin reassignments) to the design. This portability is an extremely useful feature when maintaining or upgrading systems and compensates for the slow speed of the soft processor compared to the hard processor.

Microcontrollers generally run at slow speeds ($\sim$ 20 MHz), and the Microblaze can run at higher speeds and out perform many microcontrollers. The tools used to develop an FPGA to perform microcontroller functions are not generally as simple to the new user, however for the advanced user a Microblaze can be used to develop higher performance systems with relative ease.

2.5 Embedded Linux

Embedded Linux describes a Linux which runs on embedded computer systems such as an FPGA with an embedded processor. The EBW digitiser (see Ch. 5) uses the MicroBlaze$^{\mathrm{TM}}$ soft processor. This processor is in the mainline Linux kernel. The distribution of Linux completed during the work of the thesis for use in MicroBlaze FPGA systems is called TokaLin. Embedded Linux gives the key capability of directly controlling the FPGA logic from the embedded processor by setting the appropriate registers (see Figure 2.4 and Figure 2.5). TokaLin includes a web server, ssh and many other standard Linux applications which provides the added benefit of not needing an extra PC to perform these functions.

The Microblaze soft processor although part of the mainline Linux system and so relatviely well supported from a kernel point of view is still not as well supported as the kernel for the ARM system. Additionally the operating systems (libraries and packages) that have been compiled and supported for the ARM hard processor (now in the Zynq FPGA) are much larger which means that an FPGA system using the Zynq FPGA has immediate access to the full software suite that one would expect from a Linux PC, so for example you can plug in a wireless USB and operate the device over a wireless network.

2.5.1 Memory streaming

A significant achievement of the MAST EBW digitiser system (see Ch. 5) is to acquire data from the 16 ADC channels at a sustained rate of 8 GB/s for 0.5 seconds whilst ensuring that the memory is accessible to the embedded Linux. This was made possible by using a modified AXI bus memory controller which can switch the data pins of the ADC between the ADC acquisition logic and the processor logic. Achieving these speeds is difficult due to the high frequency (250 MHz for ADC logic, 400 MHz for memory logic) at which the logic is driven making it difficult to meet timing requirements.

2.5.2 User Datagram Protocol streaming with StarkStream

FPGAs can acquire large amounts of data in a small amount of time. A key requirement is to transfer these large quantities in the least possible time and with the least delay. For this reason a low latency User Datagram Protocol (UDP) streaming protocol (called StarkStream) has been developed in the embedded Linux to quickly transfer data from the FPGA system memory to a receiving server.

2.5.2.1 Low latency

The latency over a dedicated gigabit ethernet private network is measured by sending a 1024 byte data payload UDP packet from the server, through a switch, to an FPGA, back through the switch and back to the server PC. This total round trip time is divided by 2 to give the one-way latency. This test was repeated 30 times and the standard deviation given for the latency jitter. The measured latency is 129 ± 13 μs, which corresponds to approximately a 10% latency jitter. The jitter is an indication of the determinism for data arriving at its destination. It is important to know the jitter when you need to be sure that data will arrive within a specified time period. For example in meeting the cycle time requirement of a closed loop feedback cycle. A lower latency can be achieved in future by performing a direct FPGA to FPGA measurement with a preemptible kernel since this would bypass the network stack at both ends.

2.5.2.2 Throughput measurement

The FPGA is running at a low clock frequency of 100 MHz. Without using StarkStream the UDP based TFTP program was very slow at 0.5 MB/s as it is largely limited by the processor frequency. The Linux kernel was modified to add StarkStream to the ethernet driver with Direct Memory Address (DMA). This driver monitors the connection for a StarkStream read request and sends data out over the ethernet device entirely in the kernel driver. This greatly increased the raw throughput (Figure 2.6) to 83 MB/s when using 4kB jumbo packets. We routinely transfer data sequentially at 40+ MB/s however the protocol needs refinement to operate efficiently towards the 80+ MB/s. This result shows that using a low level kernel based streaming protocol in an ethernet driver with DMA can lead to a 160+ speed up factor. The theoretical limit of Gigabit ethernet is approximately 110 MB/s. We achieve up to 75% of this figure which is a very good result considering that only a slow processor is used.

A future test will involve a direct FPGA to FPGA ethernet test where both boards are running embedded Linux. This should give a lower latency measurement since the packet will not need to traverse the network stack of a PC.

2.5.3 PLC Modbus control

Embedded Linux can use the Modbus library to create Modbus compatible systems. Modbus is one of the most widely supported PLC communication protocols but other protocols can similarly be adapted to the embedded Linux. Having embedded Linux on an FPGA systems allows it to behave as either a Modbus master or slave. Since the FPGA system is running embedded Linux there is the possibility to perform other communications (HTTP/SSH/etc) in addition to PLC communications.

Latencies of 6.6ms with 0.38ms deviation (with 995 tests) have been achieved. An error rate of 3.4×10^{-6} errors/write found after approximately 35 million writes. An error is not a catastrophic failure in that the PLC master will just attempt the write again if a

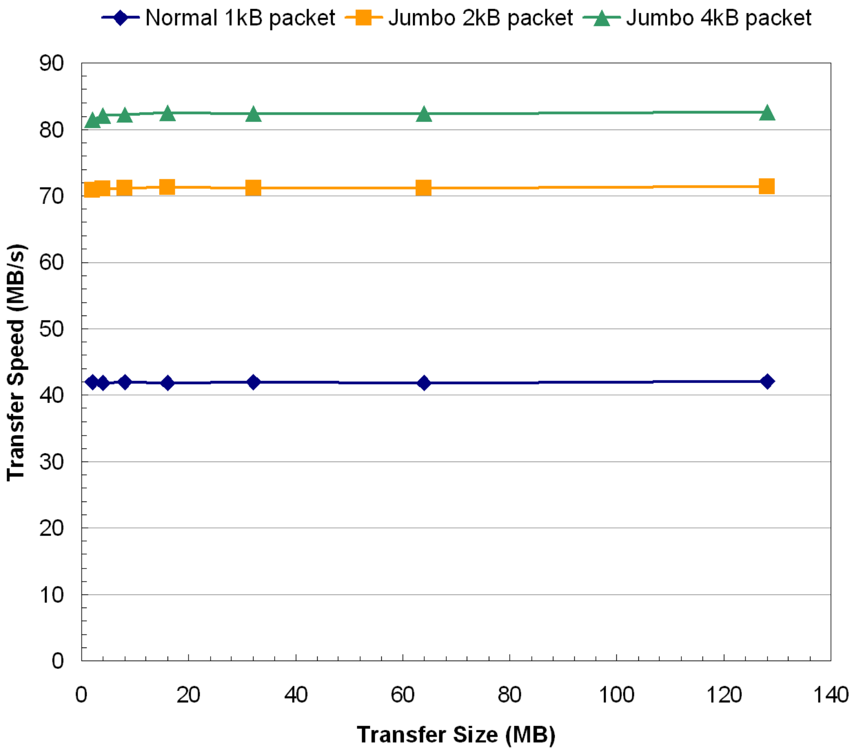

Figure 2.6: Streaming data with jumbo frames using StarkStream, a low level UDP streaming protocol. Tests have been performed using larger ethernet frames knows as "jumbo frames" on supported hardware. The speed up over the original 0.5 MB/s using TFTP is approximately 160+, resulting in raw throughput rates up to 83 MB/s, a great result on a 100 MHz MicroBlaze processor.

failure (such as a timeout) occurs. An average poll rate of $\sim$ 130 Hz is achieved over a period of 72 hours, resulting in a long term polling rate of at least 100 Hz.

The Modbus Controlled FPGA which directly interfaces with a PLC for configuration (see Fig. 2.7) demonstrates the capability of such an FPGA system to be incorporated into systems with PLCs and this technology has been used for the MAST Upgrade Fast Timer (completed) which will be a critical device of the MAST Upgrade tokamak.

2.6 Remote management

Remote management by Modbus using a PLC, a web interface, UART or other interface is a very important capability. There are two primary types of remote management, control management and development management. Generally any system will need some level of control (the simplest being a trigger) and is easy to implement. Much more challenging is full remote management for complete remote debugging and upgrade capabilities. These are necessary in large distributed systems where upgrades can only

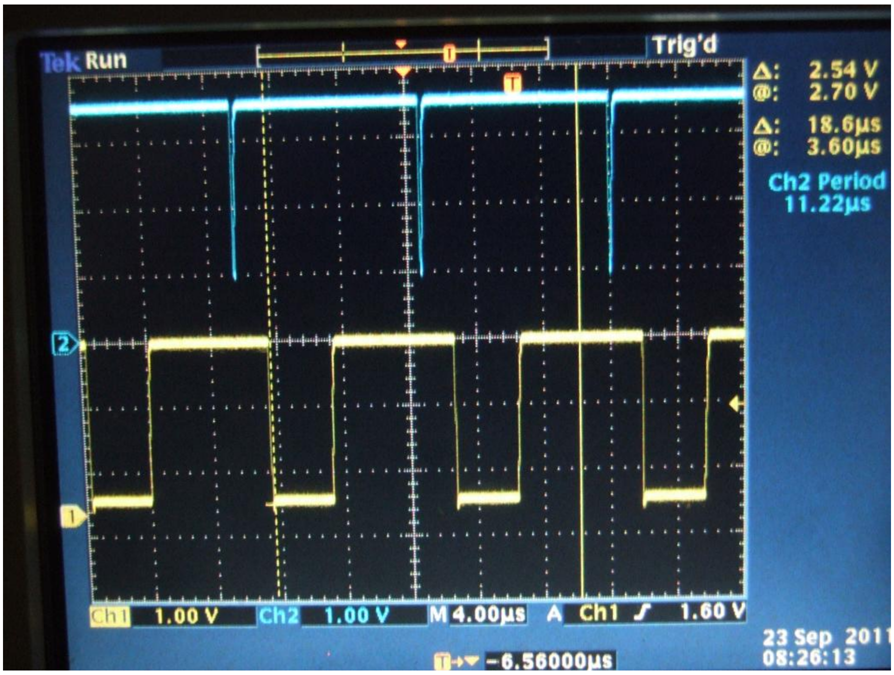

Figure 2.7: An oscilloscope screenshot of the Modbus FPGA System, with a configurable pulse delay and length controlled by a Schneider Modicon Quantum 140-CPU-651-60 PLC using Modbus. The two traces are examples of pulses generated with different delay and lengths.

be done remotely. Embedded Linux has been used to fully test this capability and is provided on the EBW Microwave Imaging diagnostic.

2.6.1 Remote hardware reset

Remote power control of an FPGA system (see Fig. 2.8) is crucial for two reasons: i) Many FPGA boards are designed such that the new firmware will only be loaded once a power cycle has been performed. ii) An FPGA system with an embedded processor may crash (as can happen to a standard PC running an operating system). In order to be able to have full control over this we take advantage of the ATX power supply which has two useful features, i) a permanent standby low current (∼100 mA) supply when the power is off and ii) an input for enabling/disabling the power.

2.6.2 Watchdog

An embedded Linux controlled watchdog (see Fig. 2.9) with the poll code implemented in the heartbeat section of the kernel ensures that in the event the Linux crashes the system will automatically reboot within a desired time period. This is useful for ensuring high system availability, particularly where the likelihood of customised hardware and therefore drivers can result in system crashes.

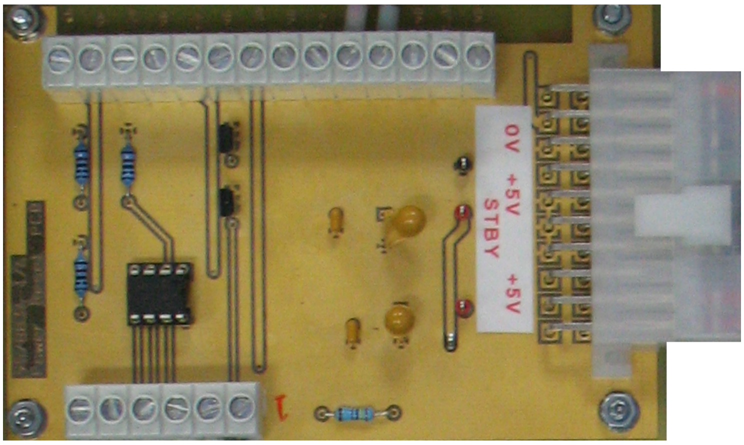

Figure 2.8: To enable full remote hardware reset capability we have created a board which does ATX 3.3V/5V/±12V power supply distribution. It enables power control via 3 inputs i) a hard wired optical receiver for optical reboot, ii) a digital I/O pin controlled by the FPGA soft processor and iii) a digital I/O controlled by the FPGA watchdog. Credit goes to Robert Stephen and Stuart Bray for developing this board. I have implemented associated electronics and FPGA firmware to use this board for the EBW digitiser system (see Section 5.4.3).

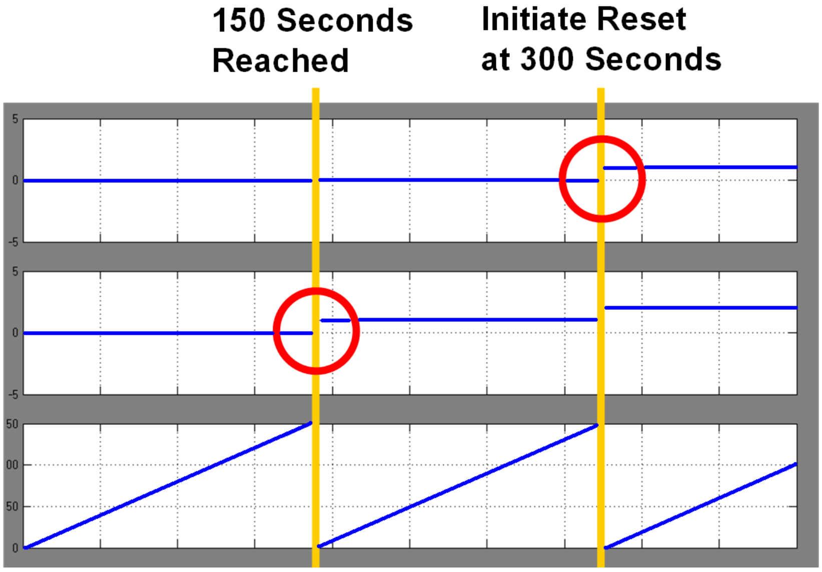

Figure 2.9: A Simulink simulation of the FPGA watchdog code which shows the counting ramp with a reset/reboot signal initiated after the processor has failed to poll the watchdog for 300 continuous seconds. The bottom trace is a ramp counter, the middle trace is a ramp that increments every 150 seconds and the top trace triggers a reset at 300 seconds.

2.6.3 Remote firmware updates

The remote firmware update uses the embedded Linux to access the storage area of the firmware (generally flash). Using embedded Linux on the FPGA provides a standard interface for updating FPGA firmware. By relying on the Linux drivers it is not necessary to develop custom drivers thus saving a lot of development time. A standard script can be used to write to the specific flash locations to perform the firmware update. The system is then power cycled using the remote reboot control capability.

2.7 Future developments

Technology continues to advance at a rapid pace and generally on a faster timescale than the development of tokamak systems, meaning between upgrades a significant technology advantage is gained. However advantages are to be gained on a continual basis due to the constant development of different systems in a research environment which push the limits of technology. It is therefore important to keep a look ahead and evaluate and test new technologies as they come out where resources permit. It is also important that designs are maintained at a high level of abstraction to allow re-porting of the design to higher performance hardware, but more importantly to allow re-porting following obsolescence of hardware.

2.7.1 High Level Synthesis

Vivado High Level Synthesis (HLS) used for Xilinx FPGAs allows a developer to write C/C++ code (see Appendix A.2) and have it converted directly into VHDL/Verilog with deterministic latency. HLS will allow code written in C/C++ to be ported to FPGAs much more easily. This is a very powerful concept and may change how FPGAs are used in the future. For example it will be easier for a developer to convert a C program analysing signals from a diagnostic to a real time processed output into (for example) a plasma control system. A HLS project can be converted to System Generator, an EDK PCore, or standard IP HDL netlist (the last two can be done from within System Generator or ISE). An AXI interface can also be added. This allows the HLS project to be developed using a familiar development chain.

2.7.2 Other developments

Increases in FPGA fabric frequency, logic size and pin count will no doubt continue. Tool improvements, which simplify the development cycle reducing the knowledge required to develop on an FPGA system, will have a big impact on project schedule and cost.

Chapter 3

Laser Beam Combiner for ITER Thomson Scattering

3.1 Introduction

The prototype laser beam combiner [24] is a system which demonstrates the ability to use a mirror moving (up to 100 Hz) under closed loop real-time control to combine the paths of multiple beams of lower repetition rate (e.g. 10 Hz) onto a single path. The requirement for the RMS pointing stability is $\pm 25\mu$rad. This may be important for ITER to increase the overall acquisition rate of the Thomson scattering system giving more frequent density and temperature profiles. This information can be used for the plasma control system and by physicists.

3.2 Instrumentation

3.2.1 System overview

The system operates in a closed loop feedback system, meaning that no other external inputs to the system are needed and the FPGA real-time monitors and corrects the actuator under control (the scanning mirror). The primary components of the system are a laser, mirror, FPGA, a Quadrant Photo Diode (QPD - see Section 3.2.2) to detect the laser position, ADC to read the output from the QPD and DAC to control the mirror. For a full list see Table 3.1. The general setup is shown in Fig. 3.1 and Fig. 3.2. The scanning mirror requires a differential output so one DAC with two channels provides both the positive and negative main driving waveform. The other DAC provides an offset correction waveform which is reduced in gain (by a factor of ~ 100) and summed onto the drive waveform. This allows fine control of the drive waveform which is necessary since a small change in the drive waveform results in a large change in the output voltage of the QPD. The interface electronics between the FPGA and the DACs and ADC are in Appendix B.1.

Table 3.1: Beam combiner instrumentation components.

Component
Galvanometer scanning mirror. Model: M3ST, GSIG Group Inc.
QPD x2. Model: PDQ80A, Thorlabs Inc.
Laser diode (class II, 650nm, continuous operation) and filters
Optical bench
Fastners (for securing devices to the optical bench)
Feedback control system
50-50 Beam splitter
Horizontal and vertical translation stages

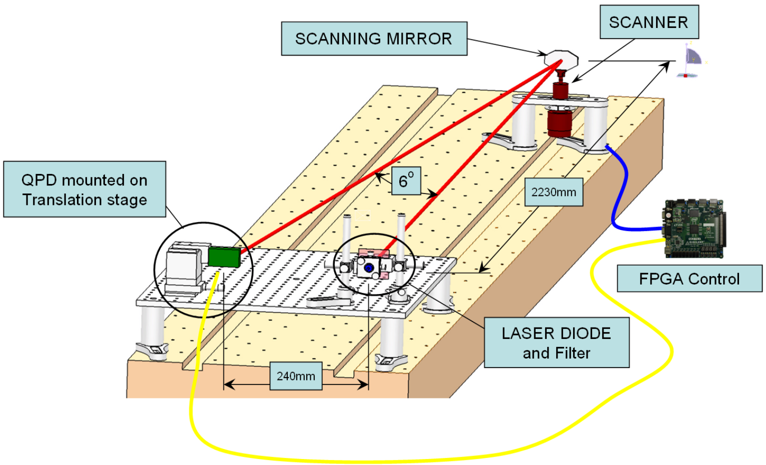

Figure 3.1: An overview of the prototype system setup showing the optical layout.

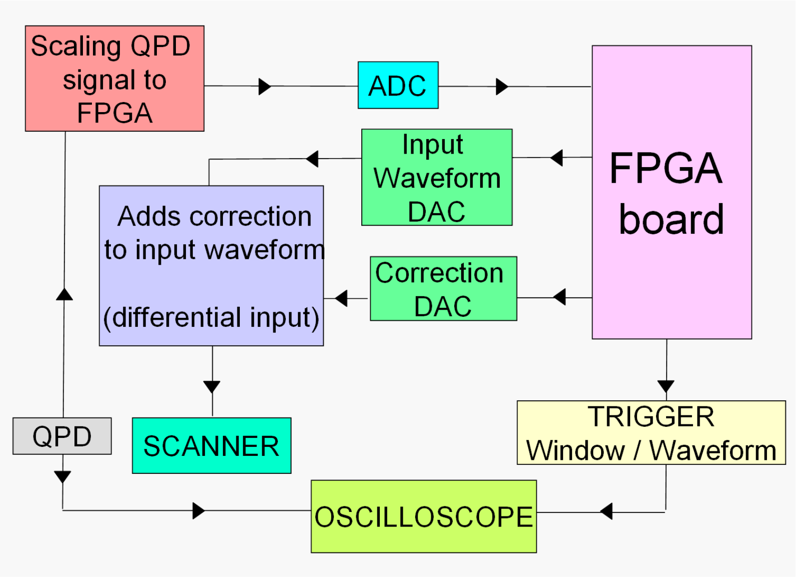

FIGURE 3.2: The entire prototype setup is shown including the inputs and outputs to the connected devices. Credit: Itziar Balboa.

3.2.2 Quadrant Photo Diode

The Quadrant Photo Diode (QPD) is a device which can be used to measure the location of an incident laser spot to a great degree of accuracy (1μrad or better). The output from a QPD is a voltage which is proportional to the laser position on the QPD. Fig. 3.3 shows a trace of this signal as the laser scans across the QPD. In order to convert calculate the pointing stability it is necessary to translate the QPD voltage into a physical position this is achieved by using the straight line fit to the curve shown in Fig. 3.4.

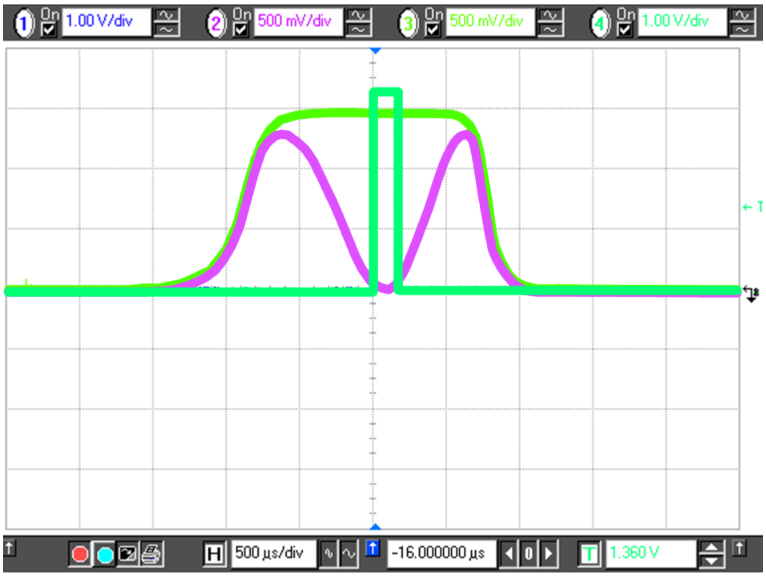

FIGURE 3.3: This image is a screen capture from the oscilloscope and shows the resultant motion of the mirror monitored on the QPD. The trigger pulse is shown in the centre. The flat peaked signal is related to the total power incident on the QPD. The double peak shows the laser beam as it travels from the edge to the centre and back to the edge. The signal returns to zero as the beam moves off the detector.

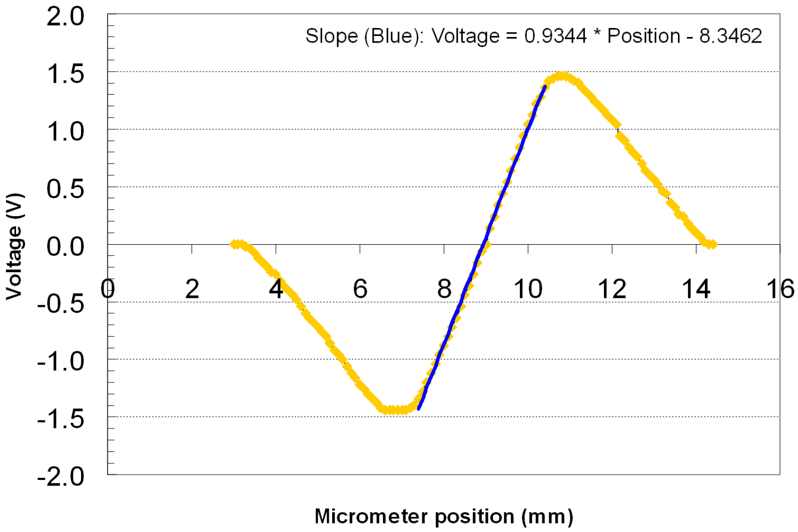

FIGURE 3.4: Moving the QPD horizontally on a translation stage reproduces the effect of a laser scanning across the QPD. A linear fit is shown that gives an equation relating QPD voltage to position. Credit: Itziar Balboa.

3.2.3 Extended setup

A second QPD is used for independent observation of the pointing stability. A 50-50 beamsplitter is used to split the signal to both QPDs, and the filter on the laser diode is reduced accordingly. Great care is taken to ensure that the QPDs are not saturated beyond its maximum ±2V as the detector will no longer give a linear output and could be damaged.

3.3 System operation

3.3.1 Mirror operation

As the mirror oscillates the laser sweeps left to right until it is brought to a stop (by stopping the mirror) to the centre of the QPD. Due to inherent unpredictable mechanical effects of the scanner, if not controlled in real time, the stopping point may randomly oscillate or drift about the true centre. This drifting is shown in the results section. Moving the scanning mirror through its full range requires ±3V differential signal. It was found that in order to stop the mirror and overcome its inertia it is necessary to slightly (but quickly) lower the final resting voltage. This is shown as a dip in the driving waveform (see Fig. 3.5).

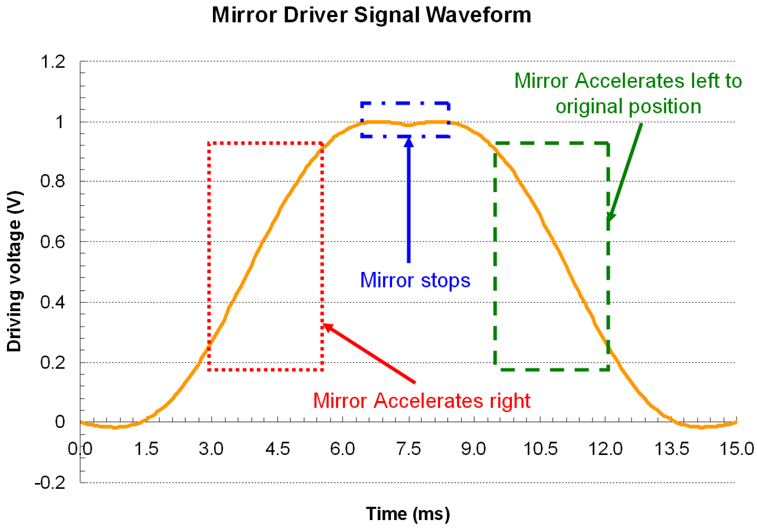

FIGURE 3.5: An example of the shape of the waveform used to drive the scanning mirror is shown. The FPGA produces a similar waveform whereby the differential output between the two channels resembles the waveform shown in the image.

3.3.2 FPGA operation

The control loop algorithm was developed in System Generator. The FPGA monitors precisely the accuracy of the laser position by averaging 8192 data points in a window 163.8μs wide about the stopping point. The FPGA then adjusts the next waveform sent to the QPD by adding or removing an offset to the driving waveform.

The control algorithm for adding the offset is basic but sufficient despite its simplicity. There are two types of offset, a large offset (10x the smaller offset) for when the laser is further off centre, and a smaller offset for when it is closer to the centre. The large offset applies when the QPD voltage is between below/above -/+ 100 mV respectively, and the low offset when the QPD voltage is between -/+ 50mV to -/+ 100mV respectively.

3.3.3 Vibration

The scanning mirror is greatly influenced by vibration. Originally there were items (laptop and other) on and near the optical bench which probably caused interference and caused the mirror to oscillate wildly beyond the correction capability of the FPGA. Removing these oscillations was a necessity otherwise it would not be possible to meet the pointing stability requirement. This was accomplished by keeping the optical bench and surrounding area clear, removing as much as possible potential sources of vibrational or electrical interference.

3.4 Results

The QPD output has 3 BNC cables. i) Y (transverse vertical) is unused, ii) sum is the total power which is recorded on the oscilloscope and iii) X which represents the horizontal laser position is split using a standard BNC T-Junction, with one output going to the FPGA to allow for the feedback, and one to the oscilloscope. A PC connected via a GPIB interface with a network cable hosts a control program. The control program was written in Python, and instructs the oscilloscope to record measurements within the trigger pulse window and record the average.

For measurements where no feedback is required an alternate version of the firmwire is loaded into the Feedback control system, which has feedback disabled. This means the FPGA will send the main waveform, but will not send any feedback corrected waveform. The comparison between the uncorrected and corrected (FPGA controlled) pointing stability measurements is shown in Figure 3.6 and a long term 6 hour acquisition is shown in Figure 3.7.

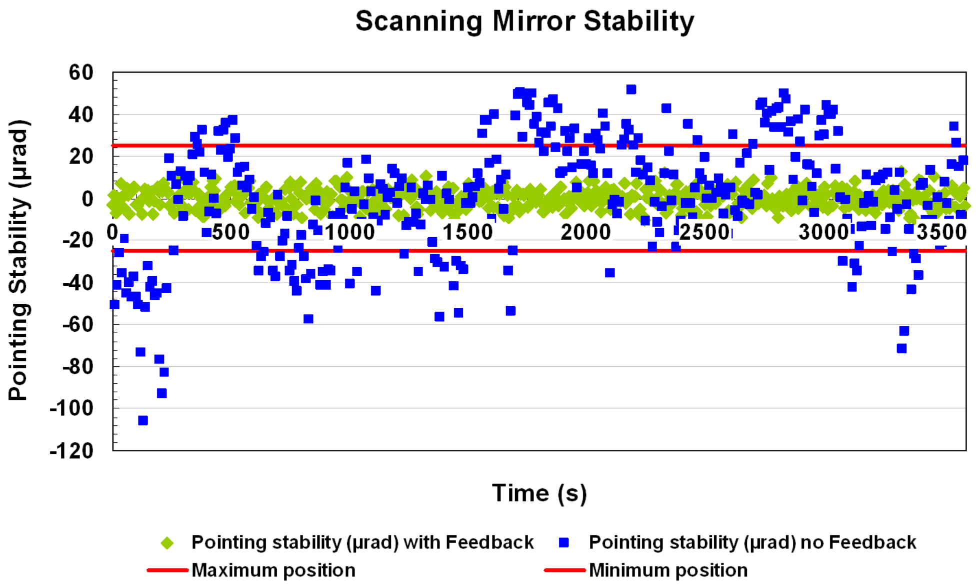

FIGURE 3.6: Shows a stability comparison with and without feedback control over a period of ~1 hr. Without active feedback the pointing stability oscillates and drifts.

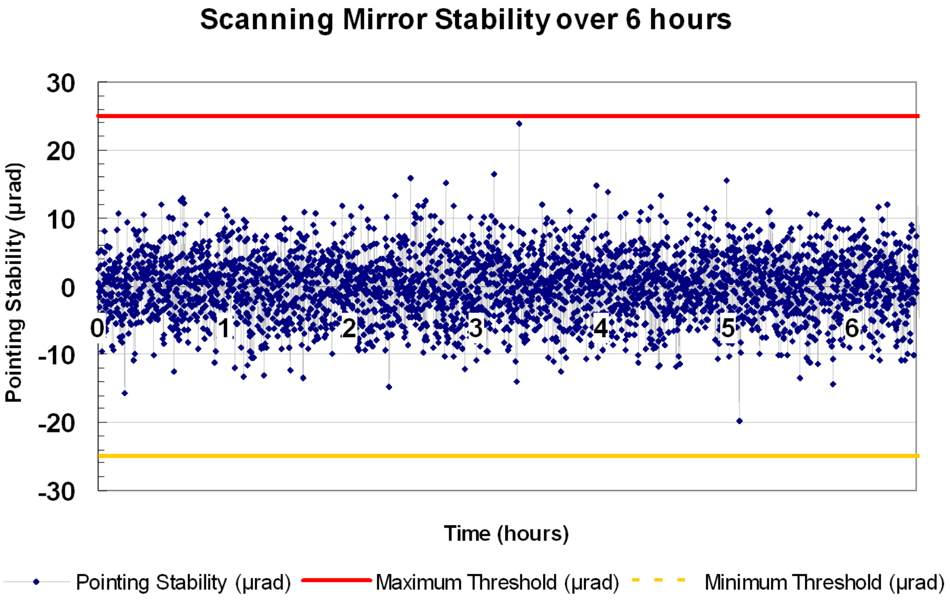

FIGURE 3.7: Shows the pointing stability with feedback control measured over 6 hours. The data sampling is 5s, this gives a total of ~4400 data points. The standard deviation is 7.6μrad and so is within the $\pm 25\mu$rad satisfying the design requirements.

By performing a Fourier transform on the two pointing stability signals (see Fig. 3.8), it is possible to identify if there are any parasitic modes induced by the feedback system. Since with feedback (green) the line is flat, we can deduce that no modes are introduced, and so the feedback system is behaving well. Without feedback (blue) there are undesirable modes, these cause the drift and oscillation of the laser stability. The full scale frequency is 10.03 Hz (calculated as 359 points [representing 3600 seconds] were operated on by the FFT).

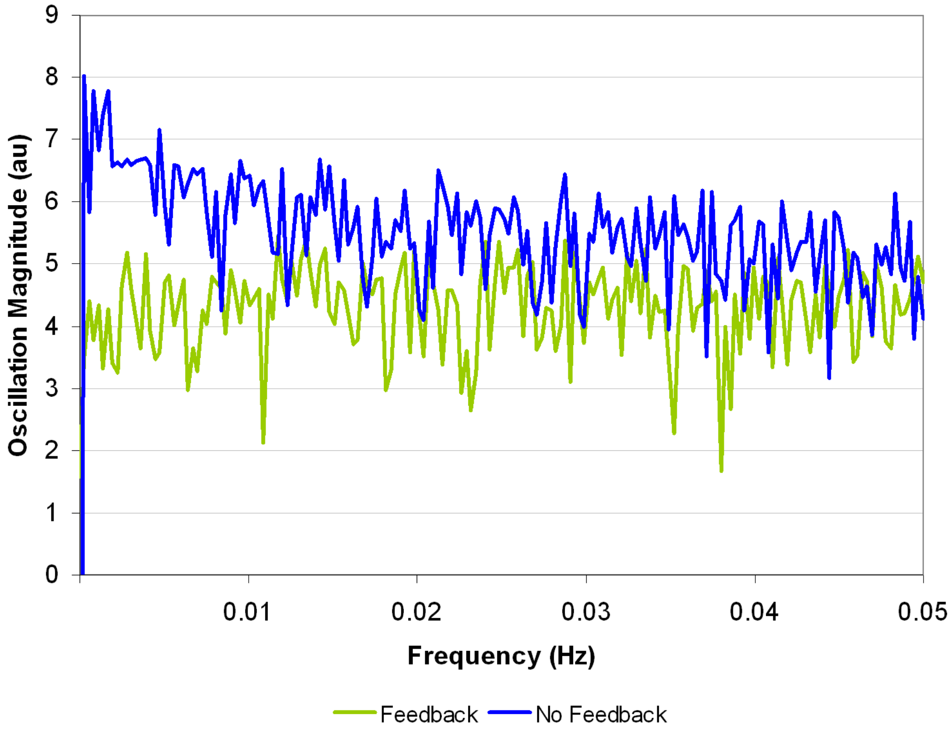

FIGURE 3.8: FFT analysis to highlight parasitic modes.

3.5 Summary

A mirror can be directed and controlled in real-time to point a laser substantially within the RMS pointing stability requirement of $\pm 25\mu$rad and time period of 15ms. The feedback system operates well and without inducing any parasitic system oscillations or instabilities. This is a significant achievement in itself however there are some limitations of the prototype that should be taken into consideration when scaling the system to multiple mirrors.

A single beam has been tested, however it is assumed the single mirror system will in principle scale when applied to multiple mirrors. The scaling may not be simple since the combination of multiple movements on previous mirrors will have a combined affect the correction. The frequency of moving the mirror was fixed at 66.67 Hz, thus expecting a fixed frequency laser pulse. The ITER specification [25] (see Fig. 3.9) is $\sim$100 Hz (using 7 lasers running at 15Hz) so this prototype is $\sim$30% slower than the ITER specification. The fixed frequency also means that using a mirror will hinder the ability to operate the lasers in burst mode with microsecond seperation which is done on MAST to view very fine timescales.

In sending a signal sent to drive the scanning mirror there will be an associated latency of about 4ms until the mirror is actually in the position. It has not been tested precisely if this latency varies. It would be an issue if the mirror was not in position during the $\sim$160us used in this prototype. However from what was seen by eye on the oscilloscope this did not occur and so what was not further investigated.

3.6 Further work

Correction on multiple lasers may need a different approach. The reason for this: In the case there are seven lasers, if scaling the described experiment above; any given correction would occur after the mirror has been moved and stopped 6 times. It is difficult in this case to say that any correction factor may still be valid after the 6 prior uncorrelated motions.

A suggested design could utilise a rotating multi-faceted object with flat mirrors on each face. The object would rotate to any defined speed which is actively controlled. Using this method the rotation is likely to be significantly more stable. Other calibration lasers can track the mirror; the moment the mirror is in the correct position (checked in real-time on one or multiple QPDs), the laser is instructed to fire. This will probably introduce microsecond level timing jitter to the laser firing as a sacrifice to having greater pointing stability. Another advantage is that a faster rate burst can be achieved by increasing the mirror rotation rate; allowing sub-millisecond laser spacing.

An alternative design could use fixed mirrors and FPGA controlled microactuators that would in real-time adjust the mirrors to compensate for any laser misalignment. In MAST the first part of the beam combination brings the lasers to a total width of 27mm and height of 7mm [26] using static mirrors alone. The advantage of such a system is that there are no lower limits to the laser spacing (neglecting optical loading which is present on any system). Additionally it may be simpler to construct and maintain with higher reliability.

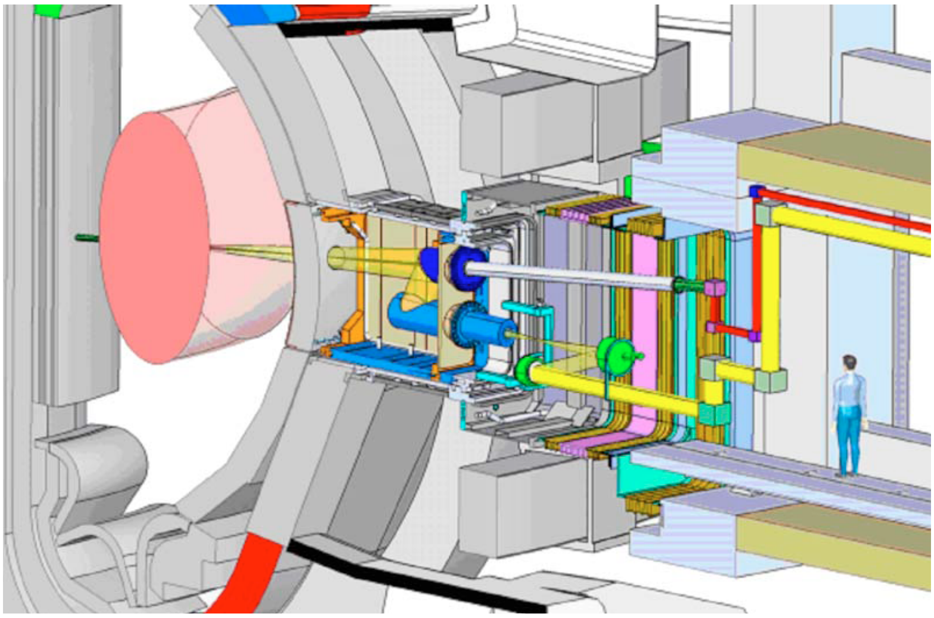

FIGURE 3.9: Outline schematic of the port plug area design for ITER [25]. It is approximately 30 metres from the laser to the plasma.

Chapter 4

Toroidal Alfvén Eigenmode Antenna

4.1 Introduction

4.1.1 Alfvén waves

Alfvén waves were considered by Hannes Olof Gösta Alfvén [27] as fluid waves, where movement of a conducting fluid (plasma) within a magnetic field will generate charge separation and electric currents which will in turn act on the fluid resulting in wave behaviour. These Alfvén waves are described using Magnetohydrodynamics (MHD) theory.

The field of Alfvén waves is rich with much physics particularly in fusion and astrophysics. In astrophysics Alfvén waves can provide information relating to the solar corona [28]. In fusion, these waves can tell us much about the plasma such as q-profile, plasma isotopes and plasma rotation [29–31]. There have been suggestions these waves could be used for plasma heating or current drive [32]. This chapter will focus on Toroidal Alfvén Eigenmodes (TAEs) which are Alfvén waves which arise in toroidal geometry (such as tokamaks, stellerators and other devices).

4.1.2 What is a TAE mode?

An Alfvén wave is a wave which satisfies ideal MHD in a magnetized plasma, of which there are three solutions. One of these solutions $\omega^2 = k_{\parallel}^2 v_A^2$ is an incompressible wave and can be thought of as a wave that exists due to tension of the magnetic field lines, like strings on a guitar. This wave is normally subject to continuum damping (resonant absorption) in homogeneous plasma and not easily excited (see Fig. 4.2). If the wave does not hit the continuum it can be driven to a large amplitude. However when a magnetized cylindrical plasma has a current through the plasma the frequency continuum forms an extremum (see Fig. 4.4) which at a radially localised part of the plasma has an extremum in the perpendicular refractive index. It is in this localised part of the plasma that a wave can exist in something like a waveguide (or fibre optic) and is weakly damped and so can be excited (destabilised) by external antennas (or fast particles). This is an Alfvén eigenmode. In the cylinder with finite length the wave continuum frequency is above zero and so the eigenmode can exist. However in a toroid the cylinder length (with periodic boundary conditions) can be thought of as infinite and so the continuum frequency can go to zero which means the eigenmode would encounter the continuum and be damped. However there are “gaps” in the continuum which form due to the periodicity of the potential the wave sees (See Section 4.2.3). It is in these gaps that Toroidal Alfvén Eigenmodes (TAEs) can exist as they do not encounter the continuum (see Fig. 4.6).

4.1.3 Motivation for studying TAE modes

In burning plasmas such as those expected in ITER, the majority of heating power will come from super Alfvénic 3.5 MeV alpha particles from D-T fusion reactions. Since $\upsilon_\alpha > \upsilon_A$ the particles can resonate as they slow down driving Alfvén modes. It is important to understand the impact that high energy (fast) alpha particles have on the plasma in order to ensure that burning plasma operation remains stable [33]. Fast particles resonantly interact with the plasma driving MHD activity such as TAEs [1, 33, 34] which can cause fast ion redistribution, pushing fast ions away from the core which reduces core neutron emission therefore potentially reducing reactor output.

Redistribution of deuterium beam due to TAEs has been seen on TFTR at $B < 1$ T [35] and many other machines as a drop of core neutron emission. Cross correlation of Mirnov (magnetic) signals to view dominant frequencies (an alternative method to adding in phase to boost SNR and attenuate incoherent noise) and radial structure measured by Beam Emmision Spectroscopy (BES) supports the conclusion of TAEs being the cause. Fast particle redistribution has been simulated by others using the HAGIS code [36]. An illustration of fast ion redistribution is shown in Fig. 4.1, is adapted from [33].

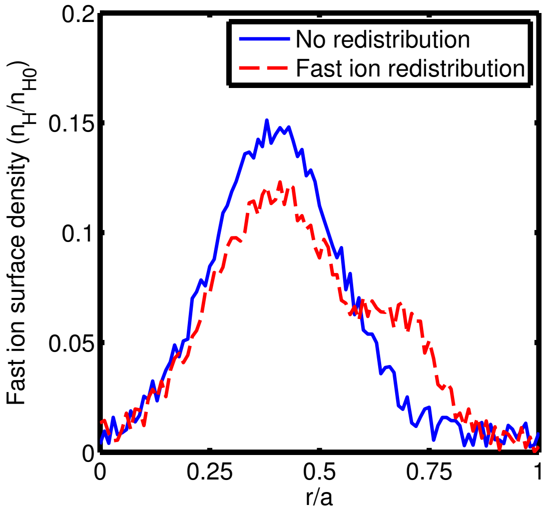

FIGURE 4.1: An illustration of fast ion redistribution. The effect of redistribution is to lower the core fast ion surface density and potentially reduce fast ion confinement.

Fast particles from heating sources such as ICRH [37] and NBI [38] can be used to drive TAE modes (and other MHD activity) [39]. On ITER the energy of the NBI ions is also designed to be 1MeV (33 MW total power) [40] which is much higher than injected ion energies in other tokamak devices and may have a significant impact on the plasma.

4.2 Theory

4.2.1 The wave equation

The ideal MHD equations are listed below. These are linearised and solved to find the Alfvén wave.

Continuity equation:

$$\frac{\partial \rho}{\partial t} + \boldsymbol{\nabla} \cdot (\rho v) = 0 \tag{4.1}$$

Momentum equation:

$$\frac{\rho D v}{D t} + \boldsymbol{\nabla} p - J \times B = 0 \tag{4.2}$$

Adiabatic equation of state:

$$\frac{D}{Dt}\left(\frac{p}{\rho^{\gamma}}\right) = 0 \tag{4.3}$$

Generalised Ohm's law:

$$E + v \times B = 0 \tag{4.4}$$

Faraday's law of induction:

$$\boldsymbol{\nabla} \times E + \frac{\partial B}{\partial t} = 0 \tag{4.5}$$

Ampère's law:

$$\boldsymbol{\nabla} \times B - \mu_0 J = 0 \tag{4.6}$$

Non-existence of magnetic monopoles:

$$\nabla \cdot B = 0 \tag{4.7}$$

Where ρ is mass density, J is current density, v plasma velocity, p is pressure, γ is adiabatic index, E is electric field, B is magnetic field and μ_0 is vacuum permeability.

Considering a homogeneous cylindrical plasma, it is possible to linearise the MHD equations and to re-write and simplify these equations [34, 37] so that they can be solved to obtain the allowable solutions (dispersion relations). The solutions to the linearised ideal MHD equations can be solved by writing the equations in matrix format, and solving the determinant below [34].

$$\begin{bmatrix} \omega^2 - k_\parallel^2 v_A^2 & 0 & 0 \\ 0 & \omega^2 - k_\perp^2 v_S^2 - k^2 v_A^2 & -k_\perp k_\parallel v_S^2 \\ 0 & -k_\perp k_\parallel v_S^2 & \omega^2 - k_\parallel^2 v_S^2 \end{bmatrix} \begin{bmatrix} \mathbf{E_x} \\ \mathbf{E_y} \\ \mathbf{E_z} \end{bmatrix} = \begin{bmatrix} 0 \\ 0 \\ 0 \end{bmatrix} \tag{4.8}$$

Where the Alfvén speed (v_A) and the sound speed (v_S) are given by:

$$v_A = \frac{B}{\sqrt{\mu_0 \rho}} \tag{4.9}$$

$$v_S = \sqrt{\frac{\gamma p}{\rho}} \tag{4.10}$$

This can also be solved in a similar manner which includes propagation at an angle to the magnetic field where $k = k' cos\theta$ with θ being the angle of the vector to the direction of propagation of the wave [32]. The resulting dispersion relations are the same. There are three solutions, the first two are given below:

$$\omega^2 = \frac{1}{2} k^2 \left(v_S^2 + v_A^2\right) \left(1 \pm \sqrt{1 - 4 \frac{k_\parallel^2}{k^2} \frac{v_A^2 v_S^2}{(v_A^2 + v_S^2)^2}}\right) \tag{4.11}$$

The first two solutions are referred to as the fast (or compressional Alfvén - CA) and slow magnetosonic waves. These waves depend on the sound speed. The third solution will be referred to as the shear Alfvén (SA) wave. The wave is incompressible and the waves propagation is analagous to the field line tension to strings in a guitar. Going forwards the waves mentioned will refer to this solution which is dependent on υ_A and not υ_S.

$$\omega^2 = k_{\parallel}^2 \upsilon_A^2 \tag{4.12}$$

This is a dispersionless wave that propagates along the magnetic field lines.

4.2.2 Background leading to the TAE

Global Alfvén Eigenmodes (GAEs) were discovered when first considering a magnetised cylindrical plasma with an axial current excited by antenna [37, 41]. The shear Alfvén wave satisfying $\omega^2 = k_{\parallel}^2 \upsilon_A^2$ becomes a TAE when considering the coupling of a propagating and counter propagating Alfvén wave in a magnetized plasma with axial current and toroidal geometry.

Initially one would expect that the toroidal geometry would not allow the TAE to exist, since the length the wave can travel through the plasma is essentially infinite due to toroidicity meaning the continuum frequency reaches down to zero. However gaps exist due to the periodicity induced by the wave travelling from a region of high to low magnetic field primarily due to the $1/r$ toroidal field. In spherical tokamaks the gradient of the magnetic field is larger, which may open up these gaps further than conventional large aspect ratio tokamaks. More will be explained about how these gaps form and the theory behind them but first a picture of the propagation of a wave in a magnetised cylinder, without current, then with current, then with toroidicity (for tokamaks) will be built up.

4.2.2.1 The Alfvén wave in a cylindrical magnetised plasma

The solution of the electromagnetic field in a cylinder is essentially a Bessel function. Bessel functions are also known as cylindrical harmonics as they are in the solution of Laplace's equation in cylindrical coordinates. A solution for the fast compressional mode matching a Bessel function is given below [32].

$$\frac{1}{r}\frac{d}{dr}\left(r\frac{dB_z}{dr}\right)+\left(k_c^2-\frac{m^2}{r^2}\right)B_z=0 \tag{4.13}$$

Broadly speaking the solutions of the excited waves in a cylinder relate to these Bessel functions. The theory describing excited waves by an external antenna is not given here but quoted. The Alfvén wave in cylindrical inhomogeneous plasma which can be written [34, 41]:

$$\frac{d}{dr}r^3\left(\frac{\omega^2}{v_A^2}-k_\parallel^2\right)\frac{\xi_r}{dr}-(m^2-1)r\left(\frac{\omega^2}{v_A^2}-k_\parallel^2\right)\xi_r=0 \tag{4.14}$$

Where ξ_r is the normalised eigenvalue. The solution of this equation gives the frequency continuum. The continuum and radial eigenfunctions for a cylindrical magnetised plasma are shown in Figure 4.2 and Figure 4.3.

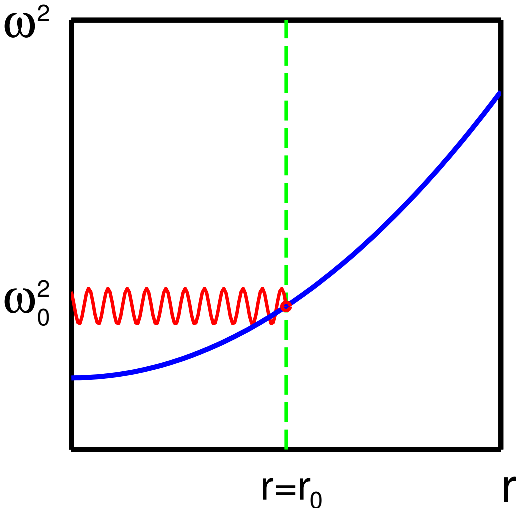

FIGURE 4.2: The Alfvén continuum in a cylindrical homogenous plasma neglecting parallel current. An externally applied antenna frequency at ω_0 is resonantly absorbed at $r = r_0$.

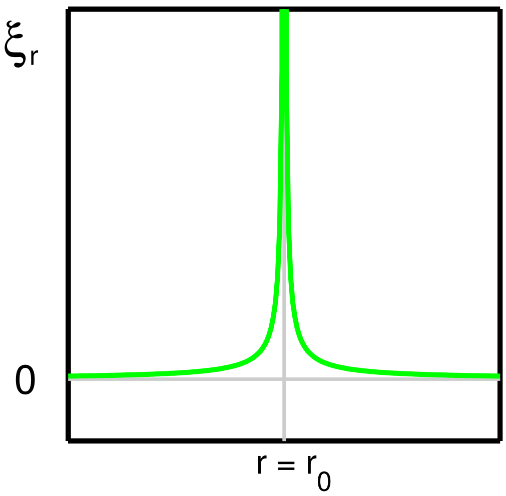

FIGURE 4.3: The eigenfunction at $r = r_0$ goes to infinity indicating resonant absorption.

4.2.2.2 The Alfvén wave in a cylindrical magnetised plasma with axial current

The current dependence introduces a dip in the Alfvén continuum (see Fig. 4.4), at the radial location of this dip at a frequency just below the continuum frequency is where the weakly damped GAE modes exist. The radial eigenmode (see Fig. 4.5) indicates where the radial location for relative absorption is highest.

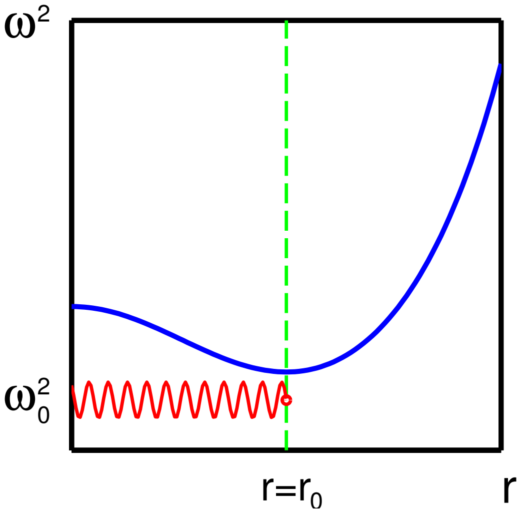

Figure 4.4: An external antenna excites a Global Alfvén Eigenmode in a cylindrical homogenous plasma with current just below the continuum extrenum. This wave is weakly damped so grows to a large amplitude.

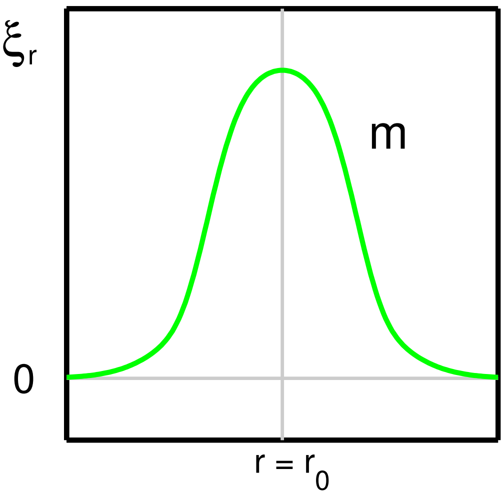

Figure 4.5: The radial eigenfunction of the GAE with poloidal number m.

4.2.2.3 The Alfvén wave in a cylindrical magnetised plasma with axial current and toroidicity induced coupling of poloidal harmonics

The parallel wavenumber as a function of tokamak geometry (n_{toroidal} and m_{poloidal}) can be written:

$$k_{\parallel} = \frac{1}{R_0}\left(n - \frac{m}{q}\right) \tag{4.15}$$

$$q = \frac{r}{R_0}\frac{B_{0\phi}}{B_{0\theta}} \tag{4.16}$$

q is the safety factor. Therefore:

$$\omega^2 = \omega_A^2 = \frac{v_A^2(r)}{R_0^2}\left(n - \frac{m}{q}\right)^2 \tag{4.17}$$

This defines the frequency and position at which a specific mode (of n, m) will experience an Alfvén resonance. The gap in the continuum is seen in Figure 4.6 and the radial eigenfunctions in Figure 4.7.

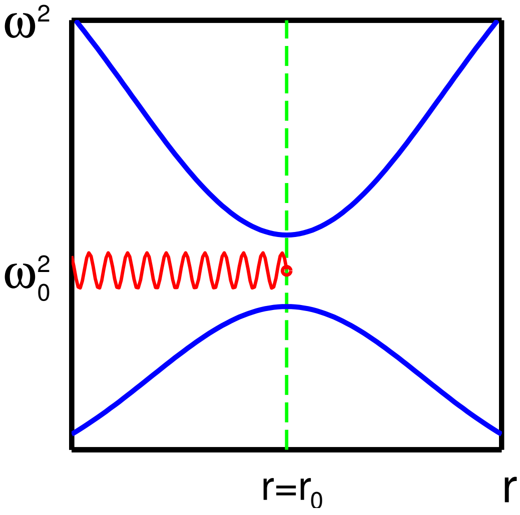

FIGURE 4.6: An Alfvén continuum with a gap due to coupling of the poloidal harmonics.

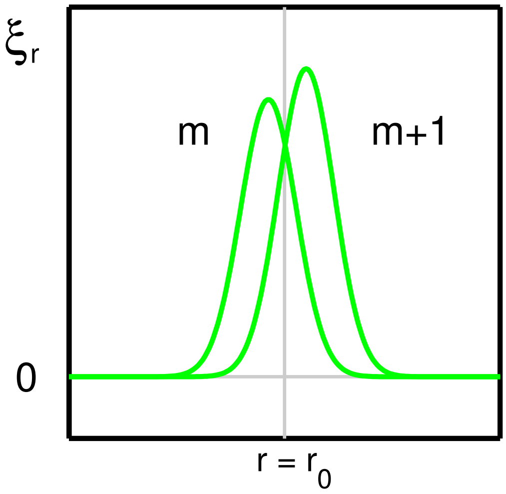

FIGURE 4.7: The radial eigenfunctions of two poloidal harmonics m and $m+1$.

4.2.3 Existence of the TAE gap

Formation of the TAE mode in a tokamak (with axial current) plasma is enabled through toroidicity induced coupling creating TAE gaps in the continuum. An increased understanding of these gaps is important since the location of these gaps defines the frequency at which one would expect to see a weakly damped TAE mode excited by an external antenna. First a qualitative description is given, followed by a more quantitative view.

4.2.3.1 Periodic potential

Assuming circular flux surfaces on a high aspect ratio tokamak we can write the toroidal magnetic field (B_ϕ):

$$B_\phi = B_{\phi 0}\frac{R_0}{R} \tag{4.18}$$

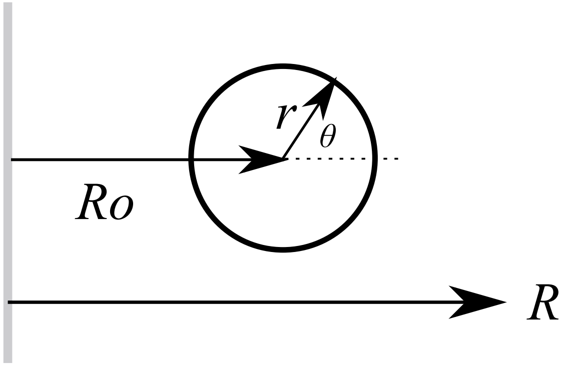

FIGURE 4.8: The equilibrium magnetic field for a circular cross section is shown to have a $cos\,\theta$ dependence by introducing the relation $R = R_0 + rcos\theta$.

Figure 4.8 gives the relation $R = R_0 + rcos\theta$ which leads us to write:

$$R = R_0 + r\,cos\theta \implies 1 = \frac{R_0}{R} + \epsilon\,cos\theta \implies \frac{R_0}{R} = 1 - \epsilon\,cos\theta \tag{4.19}$$

$$B_\phi = B_{\phi_0}(1 - \epsilon\,cos\theta) \tag{4.20}$$

The periodic potential is indicated by the $cos\,\theta$ term.

Keiras and Tataronis [42] build on previous work considering the wave on a flux surface, it is clear that the wave as it travels from the inner to the outer region of the flux surface will see a $cos\theta$ potential. To the wave this periodic potential can be considered as a lattice by using the analogy of the tokamak as an infinite periodic cylinder. The wave equation takes the form [43]:

$$\frac{\delta^2}{\delta\theta^2}\eta + [\Omega^2 - V(\theta)]\eta = 0 \tag{4.21}$$

Where η represents the eigenfunction in ballooning space, Ω is the normalised eigenvalue and V is the effective potential formed by variation of B. This equation is known as a Mathieu equation and is also used in physics to identify band gaps in crystals. See Figure 4.9 for a qualitative description. It is these band gaps that are equivalent to TAE gaps in the Alfvén continuum.

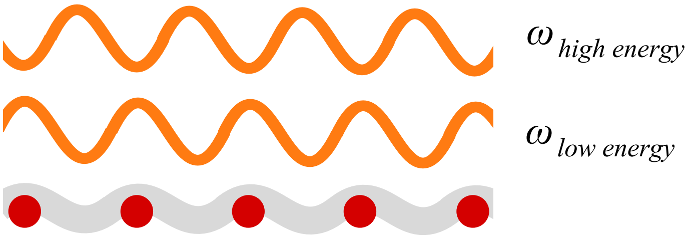

FIGURE 4.9: It can be understood why a TAE gap occurs giving two solutions by comparing the potential seen by the shear Alfvén wave to the potential seen by an electromagnetic wave interacting with atoms in a crystal. Imagine an electron travelling on a flux surface, it will oscillate between the outside (lower magnetic field) and inside (higher magnetic field) of the toroid. It will see a different B-field due to the $1/R$ toroidal field from the solenoid. This will result in a electron seing a sinusoidal periodic potential, like the potential in a lattice. If the wave is in phase, or anti-phase with the potential there will be two solutions; one of higher energy and lower energy.

4.2.3.2 Solving the coupled eigenmode functions

Quantitatively the TAE mode can be solved to show the gap [42] using quantum mechanical perturbation theory or solving the coupled eigenmode equations [1]. This section will focus on the quantitative way to solve the TAE gap using two coupled eigenfunctions, each equation representing each poloidal harmonic:

$$\begin{bmatrix} P_m & Q \\ Q & P_{m+1} \end{bmatrix} \begin{bmatrix} \xi_m \\ \xi_{m+1} \end{bmatrix} = 0 \tag{4.22}$$

$$P_m = \left(\frac{d}{dr} r^3 \left(\frac{\omega^2}{v_A^2} - k_{\parallel m}^2 \right) \frac{d}{dr} - (m^2 - 1) r \left(\frac{\omega^2}{v_A^2} - k_{\parallel m}^2 \right) + \frac{d}{dr} \left(\frac{\omega^2}{v_A^2} \right) r^2 \right) \tag{4.23}$$

$$Q = \left(\frac{5}{2}\varepsilon\frac{d}{dr}\frac{\omega^2}{\upsilon_A^2}\frac{r^4}{a}\frac{d}{dr}\right) \tag{4.24}$$

The solution is given by:

$$\omega_{\pm}^2 = \upsilon_A \frac{(k_{\parallel m}^2 + k_{\parallel m+1}^2) \pm \sqrt{(k_{\parallel m}^2 - k_{\parallel m+1}^2)^2 + 4\epsilon^2 x^2 k_{\parallel m}^2 k_{\parallel m+1}^2}}{2(1-\epsilon^2 x^2)} \tag{4.25}$$

where $x = r/r_p$. This equation according to Fu and Van Dam (see Fig. 4.10 and Fig. 4.11) is derived by assuming high aspect ratio ($R/a > 1$). It is the ideal MHD limit where the kinetic terms have been dropped from the above equations.

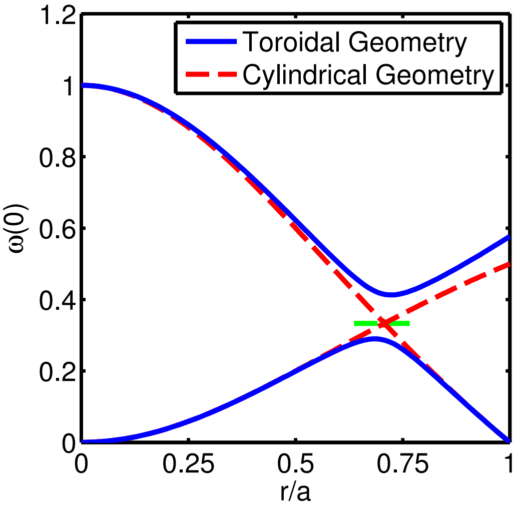

FIGURE 4.10: Calculated from Fu and Van Dam 1989 [1]. n=1,m=-1,-2 assuming the same parameters as mentioned in the paper. $\omega(0)$ is normalised frequency and r/a is normalised radius. The green dashed line is the TAE gap frequency (see Eq. 4.27).

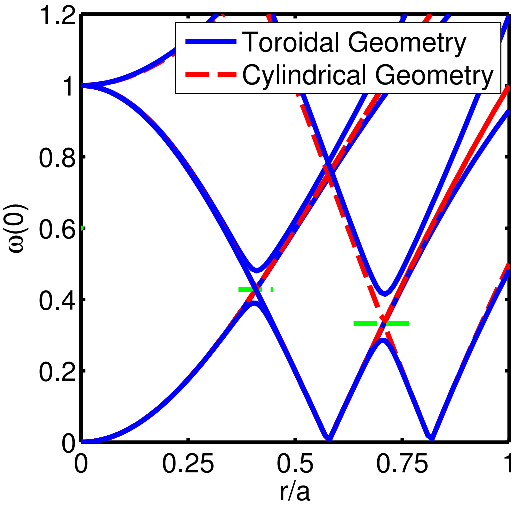

FIGURE 4.11: Calculated using the same paper. n=3, m=-2,-3,-4,-5. Using the same parameters as mentioned in the paper. It is important to note that some of the solutions overlap and a more advanced code is needed to combine these solutions together. This is provided by CSCAS [2]. $\omega(0)$ is normalised frequency and r/a is normalised radius. The green dashed line is the TAE gap frequency (see Eq. 4.27).

The CSCAS code [2] solves the MHD equations numerically. A limitation of the Fu and Van Dam paper is that the analytical solutions are for large aspect ratio, and so although suitable for JET may not be suitable for MAST. Some points however must be noted 1) It is the toroidal nature of the Tokamak that gives rise to the band gap. The higher the curvature the larger the band gap, so in principle for a spherical tokamak the band gaps allow a wider range of TAEs to exist. 2) The issue of a plasma with a seperatrix is not considered, as such the TAE experiments performed were limited on the centre column and had no X-points. 3) A code like CSCAS is needed to take into account realistic plasma conditions (q, density profile etc). The Eq 4.27 is a good estimator of the TAE frequency. An equation for the frequency shift introduced by Doppler shift due to plasma rotation is $f_n^{lab} = f_n^0 + nf_{rot(r)}$ [37].

4.2.3.3 Estimating the TAE gap frequency

The TAE frequency can be estimated using some basic equations. The TAE frequency is assumed to exist in the middle of the gap, which is sufficient for an estimate however taking into account a theory which is not limited by certain assumptions such as plasma cross section, plasma parameter profiles etc would give a more accurate TAE frequency and the different discrete modes which can exist.

Gaps exist at

$$q = \frac{(m + 1/2)}{n} \tag{4.26}$$

If this is substituted into Eq. 4.15, an equation for the TAE frequency gap is

$$\omega_0 = \frac{v_A(r_0)}{2R_0 q(r_0)} \tag{4.27}$$

At the crossing point the gap width is given by

$$\Delta\omega = \omega_+ - \omega_- \approx 2\epsilon x |v_A k_{\|m}| \tag{4.28}$$

$$\epsilon = 5r_p/2R_0 \tag{4.29}$$

In the following section a comparison will be given between the estimated TAE frequency, and that calculated by numerical modelling.

4.3 TAE antenna diagnostic on MAST

4.3.1 Diagnostic overview

The TAE antenna diagnostic is designed to create a magnetic pertubation ($\delta B/B$) to the magnetic field, which excites a TAE mode in the plasma. The TAE mode can be considered a resonance, which when excited by the correct resonant frequency from the TAE coils is driven to large amplitude and detectable by the magnetic sensors, such as Mirnov or OMAHA sensors. The drive frequency is provided by an FPGA system which sweeps through different frequencies attempting to hit a resonant frequency of a mode. One difficulty is the drive signal may be detected by the magnetic sensors and mask the plasma response. In order to obtain just the plasma response synchronous detection is used.

4.3.2 Synchronous detection

Synchronous (or phase sensitive) detection (see Eq. 4.30) takes the plasma signal from a sensor and the drive signal from the coil, and gives a narrow band signal about the drive and preserves phase information.

$$\cos\theta\,\cos\phi + i\cos\theta\,\sin\phi \implies [\text{lowpass}] \implies \cos(\theta-\phi) + i\sin(\theta-\phi) \tag{4.30}$$

Where $\cos\theta$ is the drive signal and $\cos\phi$ is the magnetic sensor signal. The resulting signal can be referred to as the complex synchronous detected signal. The advantage of having the complex form allows the instantaneous amplitude and phase to be viewed on an I-Q plot. The amplitude represents the magnitude of the signal about the drive frequency, but the only way to show that the frequency is not at the drive frequency is to show that the relative phase ($\Delta\phi$) is changing in time, which means the relative frequency between the drive and the detector is different. If there was no phase change with time, the frequencies are precisely the same and the detector is only seeing the drive signal. This would correspond to a point in the I-Q plot. A changing phase in time (or circle on an I-Q plot) shows that the detector is seeing a frequency not due to the drive, and the only other source is the plasma. If there is a combination of drive signal and plasma response seen by the detector the I-Q plot will be a circle about a point which respresents the magnitude and phase of the drive seen. If the I-Q plot is not an ideal circle, it means that the drive is not sweeping straight through the plasma response smoothly.

4.3.3 Hardware overview

The TAE antenna diagnostic consists of power supplies, matching circuits and coils. The power supplies are 500 Watts and capable of driving up to 1 MHz. There are 6 power supplies so a maximum of 6 coils (see Fig. 4.12 and Fig. 4.13) can be driven. The matching circuits transfer power from the power supplies to the coils. The ouput of the power supply is fed to the primary of a transformer, the secondary is connected to a coil with a capacitor to create a resonant circuit. The target frequency of the power supply is $\sim 80 - 120$ kHz and the resonance of the matching circuit is chosen optimally for this. Too high gain 'Q' (i.e. too narrow a bandwidth) of the resonant circuit cannot be chosen since it is desirable to sweep the frequency of coil through a relatively large frequency range.

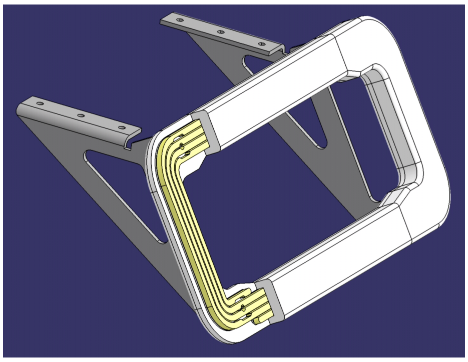

FIGURE 4.12: A TAE coil with a view through the protective cover.

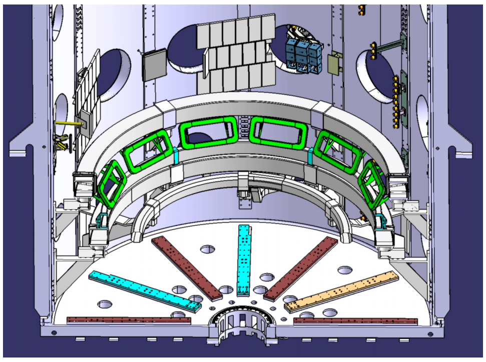

FIGURE 4.13: The 12 TAE coils in the lower half of the vessel. There are 6 in the upper half.

The power supplies take an input RF single up to 1MHz. This is provided by an FPGA system (see Fig. 4.14) consisting of a Nexys 2 FPGA with 8 DACs providing up to 4 arbitrary outputs and their inverse. The FPGA is controlled remotely via UART (RS232) over ethernet which configures the desired frequency sweep. The FPGA system was pre-existing (except the critical damping circuit). The contribution of the work of this thesis was to upgrade and program the FPGA system and use it to obtain new experimental results. In addition the FPGA can send a blanking signal which alternately switches the power supplies on and off at a high repitition rate. Due to the resonant nature of the coils, when the power supply is turned off it takes some time for the power to dissipate in the resonant coil (it naturally keeps it due to its resonance) so a critical damping circuit (see Fig. 4.15) was added which triggers a short circuit through a (non inductive) resistor on the coil side when the power supply is blanked (turned off). This blanking can occur at hundreds of hertz to kilohertz rates. The timing must be carefully orchestrated otherwise if the output of the power supply is still active, significant power will be reflected back potentially tripping or damaging the power supply.

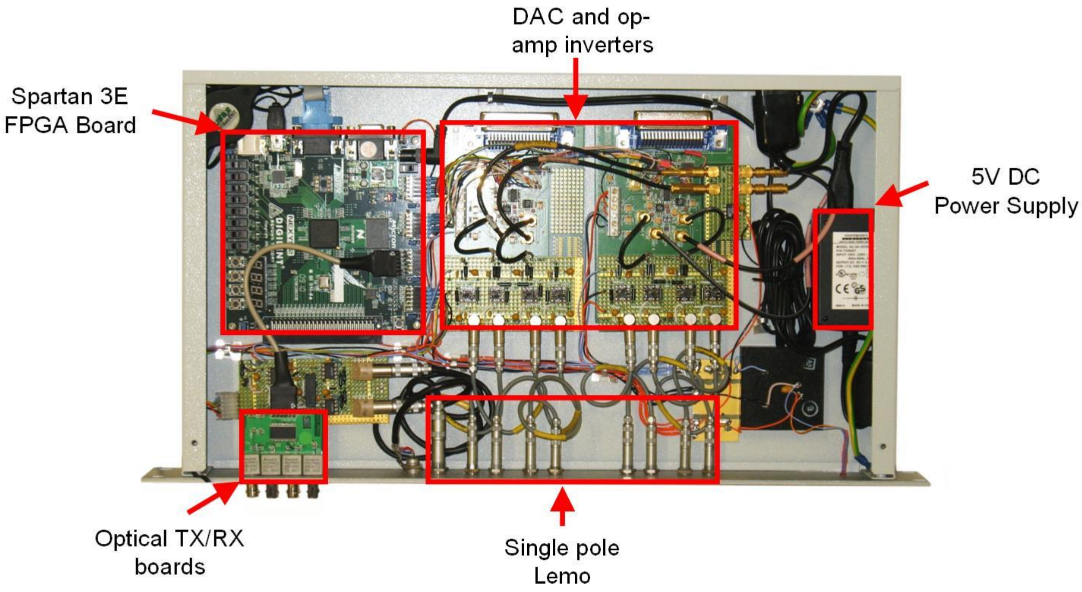

Figure 4.14: The TAE antenna are driven by an FPGA system which controls the frequency sweeping of the antenna.

4.3.4 Resonance Detection

4.3.4.1 Critical damping

Since we are concerned about the drive signal swamping the plasma signal a critical damping circuit (see Fig. 4.15) was added to the resonant coil circuit to allow the drive to be turned off quickly. The idea is that if the drive is suddenly critically damped, the signal due to the resonance of the plasma will damp at its natural damping rate and be larger than any remaining drive signal, thus enhancing the TAE resonance signal on the magnetic sensor compared to the direct signal from the drive coil. However this assumes that the Q of the TAE resonance is sufficiently high, otherwise the drive signal will always swamp the plasma signal. Using a critical damping circuit may be useful for detection of TAE modes however for the purpose of this thesis the experiments from the critical damping circuit are not explored in detail. The switching complicates the analysis and interpretation so instead shots without critical damping (high speed switching) of the drive are analysed.

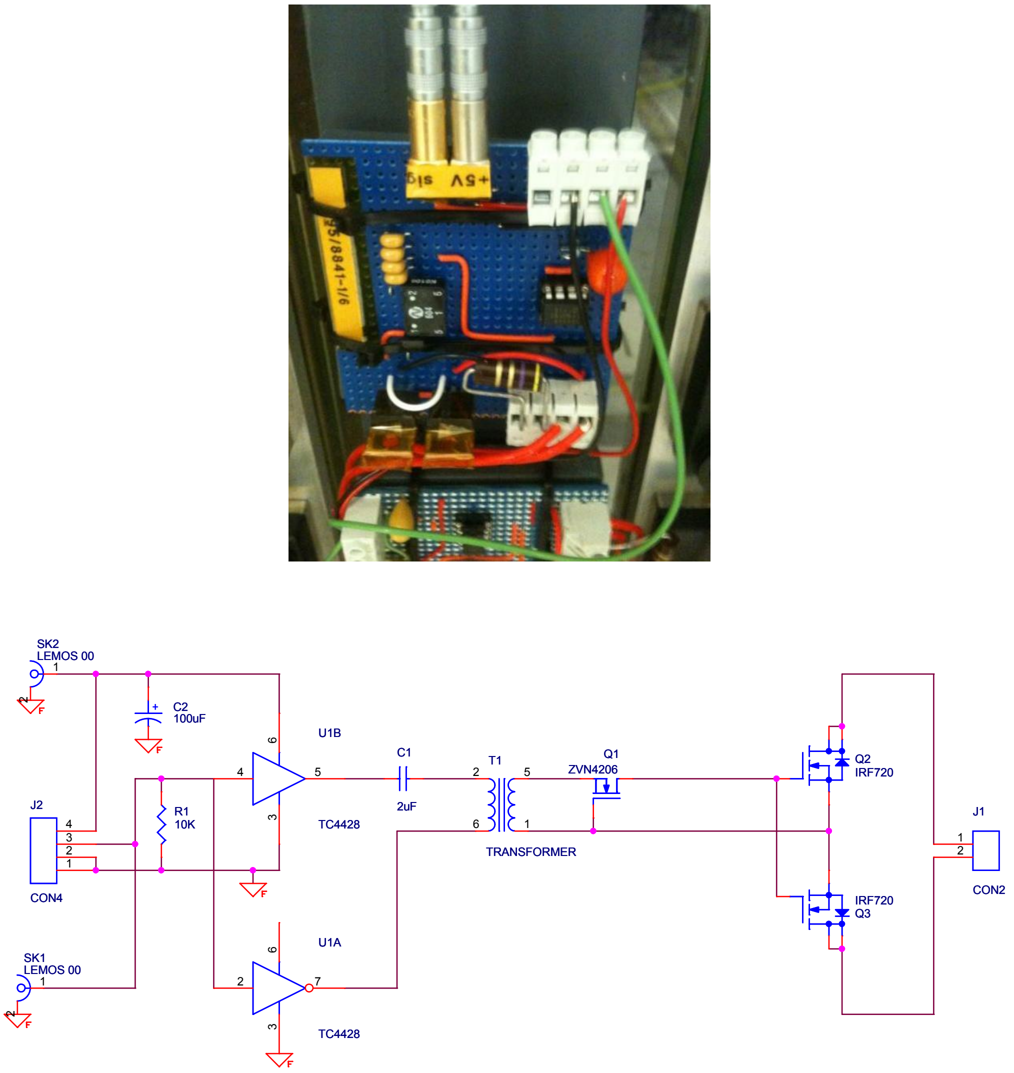

FIGURE 4.15: Critical damping circuit.

4.3.4.2 Impedance based detection

The primary advantage of the resonant circuit is that more power is driven to the coil. A side effect of using a resonant coil means that it is sensitive to impedance of the plasma, since a changing impedance can significantly change the gain of the circuit or current in the coil and hence excitation strength. It has been shown that the presence of an Alfvén resonance corresponds to a big impedance change (see Fig. 4.16). The effect of the impedance on the drive circuit can be interpreted as a resonant drive coil having a roughly constant power but as it crosses the TAE mode frequency the plasma will appear as a higher load (or impedance) and power will quickly transfer from the resonant drive coil into the TAE mode in the plasma. This can be seen by measuring a reduced voltage or current on the drive coil. Therefore it may be that a resonant drive circuit aids in TAE mode detection, with sensitivity increasing with increased Q.

This should be further explored. This comes at the cost of reduced frequency span one can drive through since for a resonant circuit as Q increases the bandwidth decreases. One way around this is a tunable resonant drive, in the same way a radio can tune its resonant frequency to scan across the frequency spectrum however this is difficult in power electronics.

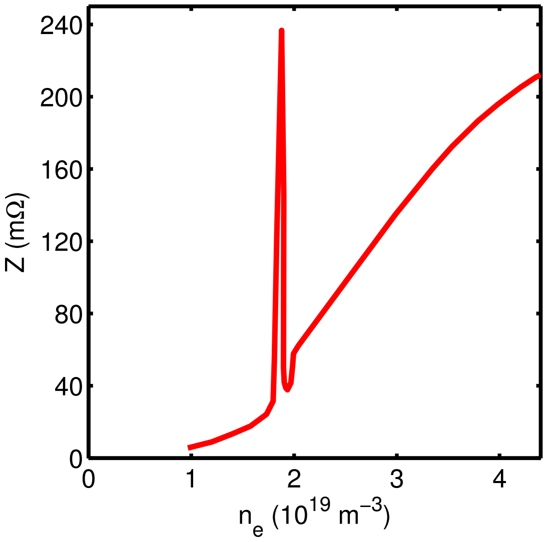

Figure 4.16: This figure is taken from Appert et al [41]. Antenna load versus line-averaged density. Refer to the Appert paper for full details. There is a very dramatic impedance change corresponding to the TAE mode.

4.4 Experimental data on MAST

The goal of the experiments is to identify for the first time on MAST if a TAE mode could be driven by the TAE antenna.

4.4.1 Shot 28345 vs. 28346

The characteristic TAE frequency f_A (derived from Eq. 4.31) has a dependency of $B/q\sqrt{n_i}$. We assume $n_i \sim n_e$ (quasi-neutrality).

$$f_A = \frac{\upsilon_A(r_0)}{4\pi R_0 q(r_0)} \sim \frac{B}{\sqrt{n_e}} \frac{1}{q(r_0)} \tag{4.31}$$

The υ_A is calculated using the toroidal field B at the magnetic axis. The density used is the line integral density (signal "ane_density" on MAST) divided by a constant factor (∼4) to bring the density to the range of the Thomson scattering core density (signal "ayc_ne_core" on MAST), and give mode agreement (as seen on the frequency spectrogram) with the characteristic TAE frequency. This factor of ~ 4 was calculated by dividing the line integral density by the core Thomson scattering density. The core density signal is not used since core density can fluctuate significantly and has a lower time resolution, limited by the Thomson scattering laser repetition giving a time resolution of ~ 4.3 ms. The q plotted (see Fig. 4.17 and Fig. 4.18) are two different q's, one which is the on-axis q provided by the MAST equilibrium reconstruction code (EFIT) [44], and another which is a fit to this, but with a lower start q. The reliability of the q provided by E-fit before 200 ms is debatable and although a lower q before 200 ms would certainly support the apparent mode frequency the key point is that q after 200 ms where the primary resonance is observed is essentially constant ($q \sim 1 - 1.2$). This means that the uncertainty in the accuracy of E-fit before the 200 ms does not impact the conclusion of the results.

To drive a TAE mode and confirm that it is a TAE resonance there are two primary ways: i) use a steady-state plasma with constant mode frequency and then sweep the coil frequency crossing the mode frequency [45], ii) use a changing plasma which sweeps the mode frequency and crosses a constant coil frequency . We have attempted both methods but the first option, of a steady state plasma is difficult on MAST due to the short pulse duration and a generally varying density. Thus the second option is preferred, where

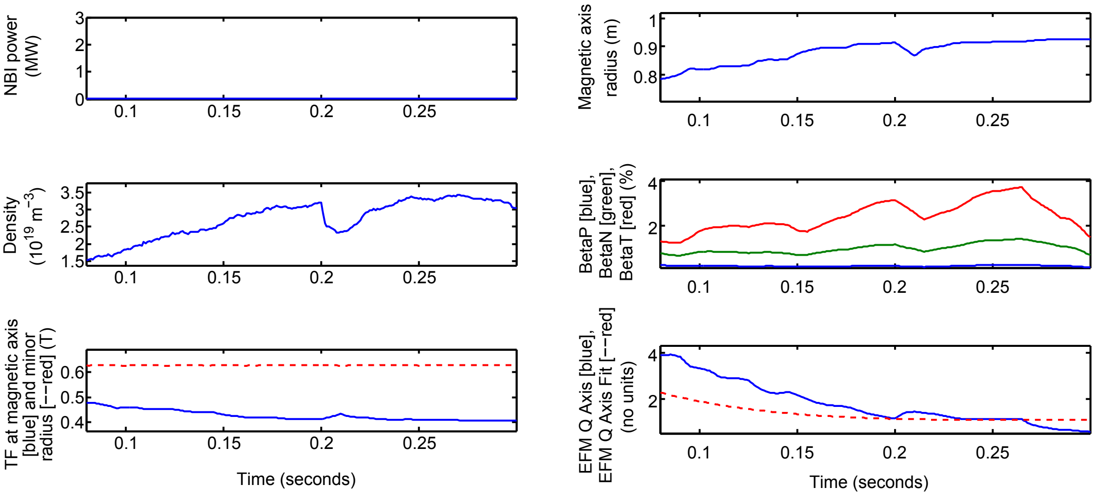

FIGURE 4.17: Shot 28345 plasma signals.

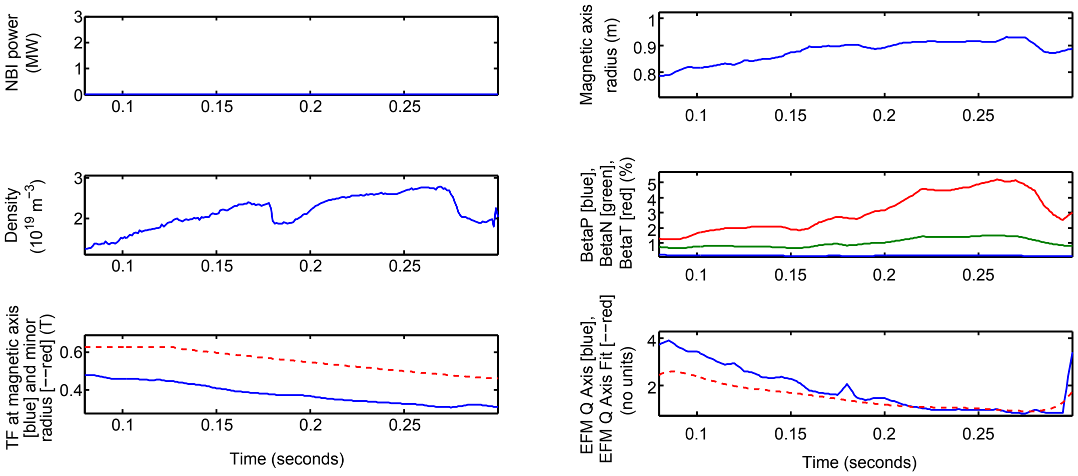

FIGURE 4.18: Shot 28346 plasma signals.

we have a fixed drive frequency while relying on the changing plasma parameters and attempting to control them. The plasma parameter which is easiest to change deterministically is the toroidal field. A big advantage of using a constant drive frequency is that the individual amplitude-frequency responses of the drive and detector are not included. This is particularly important in these experiments since the drive is a resonant circuit and sweeping in frequency, we might detect the resonance of the drive. Additionally magnetic detectors (particularly high bandwidth such as the OMAHA magnetic coils) will have their own frequency response. Using synchronous detection we can distinguish the drive from the plasma response by looking at the I-Q diagram (as explained in 4.3.2).

The Alfvén speed and therefore the characteristic TAE frequency can then be changed

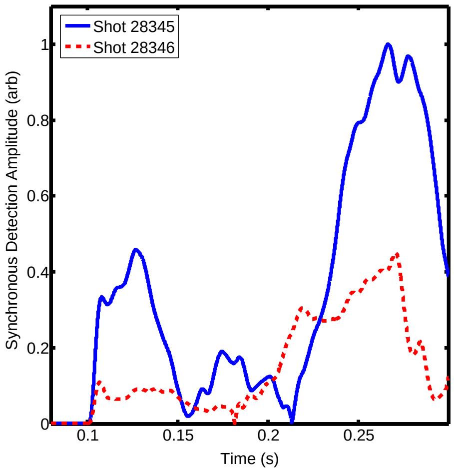

FIGURE 4.19: Comparison of the synchronous detection amplitude from shot 28345 and shot 28346.

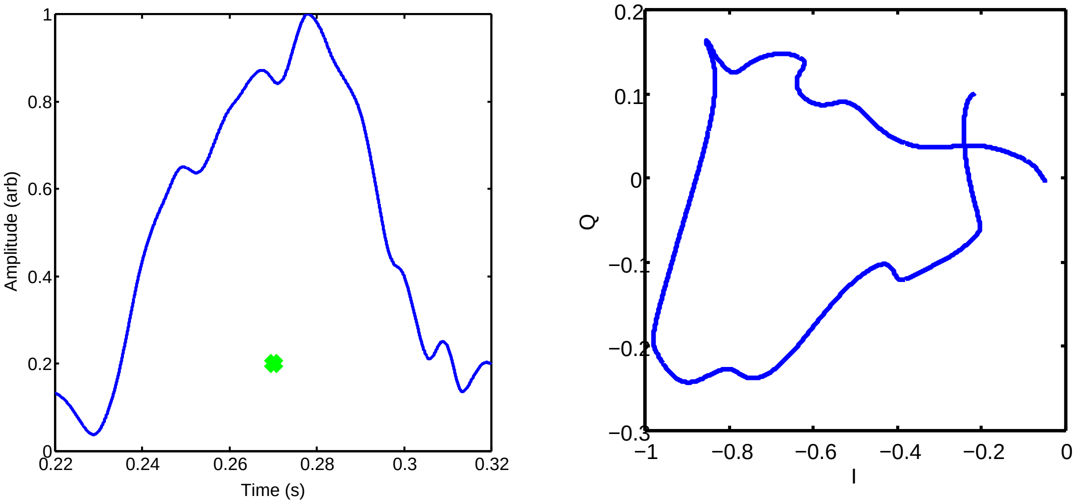

FIGURE 4.20: Left: Shot 28345 with resonance at 0.27 seconds (indicated by green star). Right: I-Q plot. A relatively good circle is seen. The centre of the circle is not $(0,0)$, which shows that there is a constant presence of the drive detected, but since the circle goes around the mean position this means the resonance is not at only the drive frequency, and so is a signal due to the plasma response as the drive frequency passes through the mode frequency.

from shot to shot. This analysis focuses on shot 28345 and shot 28346 which are the same except the latter has a reduced TF from 125 ms. This has the effect of moving the characteristic TAE frequency earlier in time from shot 28345 to 28346. What these data show is that two seperate shots have increased power (as viewed in the spectrogram as more red) at or near the characteristic TAE frequency.

The main resonance (largest signal amplitude) completes an approximate circle in the I-Q plot (Fig. 4.20 and Fig. 4.21). Since the characteristic TAE frequency does not

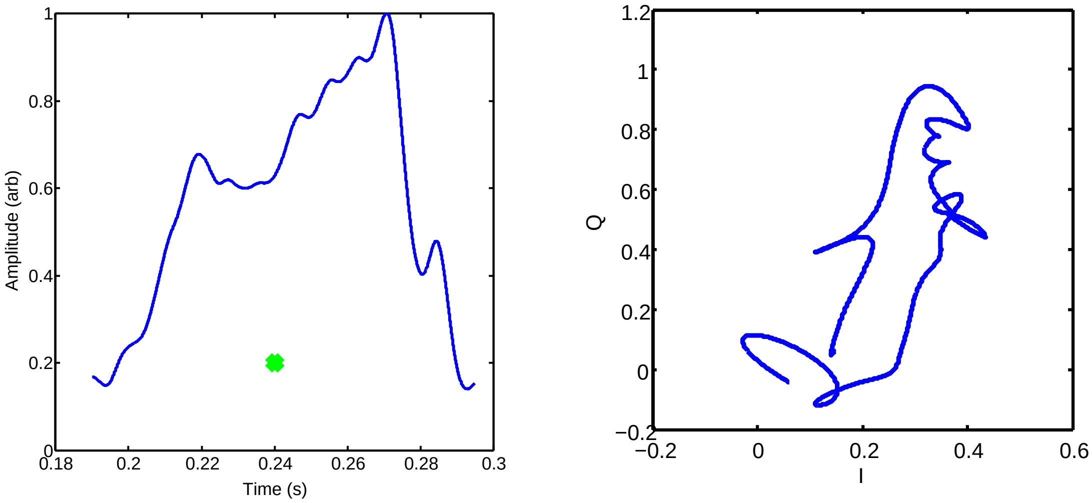

FIGURE 4.21: Left: Shot 28346 with resonance at 0.24 seconds (indicated by green star). Right: I-Q plot. This is not a particularly good circle, probably because the drive is not sweeping cleanly through the characteristic TAE frequency, but the drive and TAE frequency stay matched for much of the resonance and then move through. Despite this not being a clear circle, it is clearly going around in phase and thus like shot 28345 proves that we are not looking at just the drive frequency, but a signal due to the plasma response as the drive frequency passes through the mode frequency.

sweep quickly or linearly through the mode, the I-Q plots are not precise circles as can be seen in a more stable plasma (such as JET). The important requirement for resonance detection is the signal completes a loop, which is seen in the plots. The main resonance (see Fig. 4.19) moves earlier in time by ∼ 30 ms from shot 28346 to 28345, this corresponds to the characteristic TAE frequency which also moves by ∼ 30 ms (as indicated by the green stars, see Fig. 4.22 and Fig. 4.23).

The following is the summary of the evidence that a TAE mode has been driven and detected: i) the signal is only present at the drive frequency of the coil which proves the coil is driving the signal, ii) the signal of interest (using synchronous detection) completes a loop on the I-Q plot, which proves this signal is a resonance, iii) a fixed frequency drive is used eliminating any other system resonances which proves the plasma is the source of the resonance, iv) the centre of the signal (green stars) moves with the characteristic TAE frequency of the plasma which proves the resonance is a coil driven TAE resonance.

4.5 Summary

The TAE theory has been explained stating that TAE gaps are seen due to the curvature of a tokamak plasma, and it is easily seen that these gaps are larger due to increased

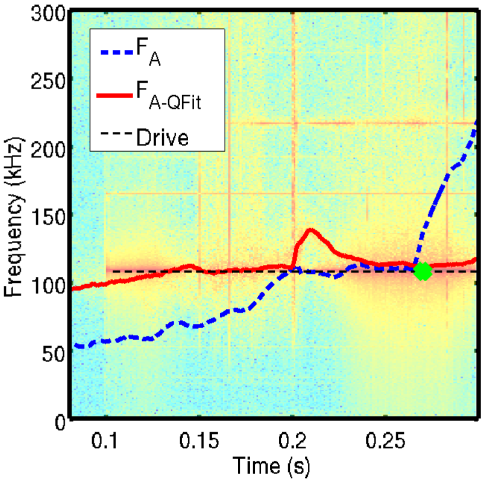

FIGURE 4.22: Shot 28345 with characteristic TAE frequency drive interaction at 0.27 seconds (indicated by green star). The background signal is the spectrogram of the OMAHA 5LZ coil.

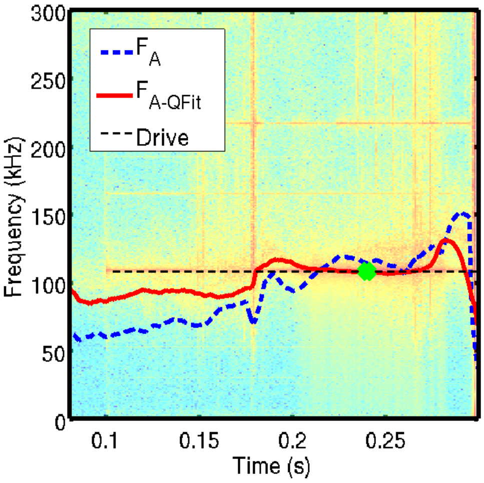

FIGURE 4.23: Shot 28346 with characteristic TAE frequency drive interaction at 0.24 seconds (indicated by green star). The background signal is the spectrogram of the OMAHA 5LZ coil.

curvature in spherical tokamaks, so TAEs on MAST should have a broader spectral width. The TAE antenna diagnostic has been described. An FPGA has been used to allow programmable drive frequencies and future capabilities for mode tracking. The resonant drive has increased power driven to the coil and potentially the sensitivity to the impedance of the plasma (and therefore the TAE mode as shown in Appert et al [41]). Experiments have been performed and analysis provided which gives very good evidence that for the first time on MAST TAEs have been driven by the TAE antenna. This is the first step towards using the antenna diagnostic to understand more about the plasma on MAST.

Chapter 5

Electron Bernstein Wave Microwave Imaging

5.1 Introduction

This chapter focuses on the EBW synthetic aperture microwave imaging (SAMI) system on MAST. First the motivation for studying EBW is given, followed by theory of EBW emission. Next a description of the SAMI system is given. The analogue components are described along with FPGA implementations of side band seperation (SBS) and single side band (SSB) up conversion. The digital electronics are described with a focus on the FPGA development and the challenges of developing an FPGA phased array system. Following that a description of synthetic aperture imaging with the overlap with astronomy is given, followed by a description of an alternative imaging method (intensity interferometry) and potential application of a similar (intensity based) method for pitch angle measurement.

5.2 Motivation for studying EBW

5.2.1 Heating and current drive

Heating and current drive are important for fusion. Before a fusion plasma generates its own internal heat from fusion born alphas, it must be heated up to the ignition temperature ($\sim$20keV). To maintain plasma confinement an axial current must flow in the plasma. Since the plasma is essentially a turn on a transformer, to produce a constant plasma current using purely inductive effects is not possible, since that relies on a constant changing current in another coil (solenoid) but one cannot change the current in one direction forever and so solenoid based current drive will always be pulsed based. Other methods are needed for steady state current drive. Steady state operation is ideal for a reactor which needs to provide a constant base load power supply.

Usually the electric field (E) in a plasma drives the current. Considering the electric field due to the solenoid, the electric field is proportional to the loop voltage (V) over the major radius (R).

$$V = L\frac{dI}{dt} \tag{5.1}$$

$$E = \frac{L}{2\pi R}\frac{dI}{dt} \tag{5.2}$$

Where L is the inductance and I is the current through the solenoid. For bigger devices such as ITER or DEMO inductance increases. As inductance increases it naturally reduces the maximum dI/dt, thus for larger devices the electric field is lower. On ITER it is only 0.35 V/m [46]. This makes plasma breakdown and current drive using solenoid difficult in larger devices, and another reason that alternative heating and current drive methods are useful.

In tokamaks over the decades many different techniques have been used. They each have their advantages and disadvantages and a detailed review of the different methods is needed to identify which is best. This chapter does not perform a detailed review but focuses on Electron Bernstein Waves (EBW) which have been used to good effect on MAST for both current drive and heating [47, 48]. Other different methods include neutral beam injection (NIB/NBI), lower hybrid current drive (LHCD) [49] and electron cyclotron resonance heating (ECCD/ECRH). What places one technique above another, especially when considering a future reactor is the efficiency of the heating and current drive methods.

5.2.2 Efficiency

5.2.2.1 Reactor efficiency

Reactor efficiency improves with higher beta β which is the ratio of plasma pressure to magnetic pressure. A device with higher beta means that plasma will be confined for a given lower field. A high beta reactor is more efficient because creating magnetic fields is expensive.

$$\beta = \frac{P_{plasma}}{P_{magnetic}} \tag{5.3}$$

In conventional tokamaks beta is on the order of a few percent (For JET 8% [50], $A = 3$). In low aspect ratio (spherical) ($A = 1.4$) tokamaks such as MAST the beta is higher. The record is the START tokamak with a peak central beta of 50% [51].

5.2.2.2 Absorption efficiency

Absorption efficiency is related to the optical thickness of the plasma and strongly related to heating a current drive efficiency. The following relations [52] show the optical thickness and a function of temperature. The hotter the plasma the more efficient the absorption.

$$\tau_{n,X} \sim \left(\frac{T_e}{m_e c^2}\right)^{n-1} \tag{5.4}$$

$$\tau_{n,O} \sim \left(\frac{T_e}{m_e c^2}\right)^{n} \tag{5.5}$$

$$\tau_{n,X} \sim \tau_{n-1,O} \tag{5.6}$$

Where n is the harmonic number and O and X are the ordinary and extraordinary mode. More detail will be given about these modes in the theory section, the important point to note is that with increasing harmonic number the efficiency of absorption decreases.

This limits practically in most (but not all cases) useful ECRH or ECCD up to the 3rd harmonic.

Starting with the definition for plasma beta

$$\beta = \frac{2\mu_0 \langle p \rangle}{B^2} = \frac{2\mu_0 \langle nT \rangle}{B^2} \tag{5.7}$$

The electron cyclotron frequency

$$\omega_{ce}^2 = \frac{e^2 B^2}{m_e^2} \tag{5.8}$$

The plasma frequency

$$\omega_{pe}^2 = \frac{ne^2}{m_e \epsilon_0} \tag{5.9}$$

Using the relation $c^2 = 1/\epsilon_0 \mu_0$

$$\frac{\omega_{pe}^2}{\omega_c^2} = \frac{m_e n}{B^2 \epsilon_0} \tag{5.10}$$

Substituting Eq. 5.10 into Eq. 5.7

$$\beta = 2\mu_0 T \frac{\epsilon_0}{m_e} \frac{\omega_{pe}^2}{\omega_{ce}^2} = 2 \frac{T}{m_e c^2} \frac{\omega_{pe}^2}{\omega_{ce}^2} \tag{5.11}$$

Gives the relation

$$\tau = \frac{\beta}{2} \left(\frac{\omega_{ce}}{\omega_{pe}} \right)^2 \tag{5.12}$$

This shows that for a given optical thickness which is a measure of absorption efficiency is only large if the cyclotron frequency is much larger than the plasma frequency, that is if the plasma is underdense. In spherical tokamaks such as MAST the plasma is well overdense (see Fig. 5.1 and Fig. 5.2) so EBW heating and current drive is a more efficient alternative [53] since EBW waves have no high density limit [54].

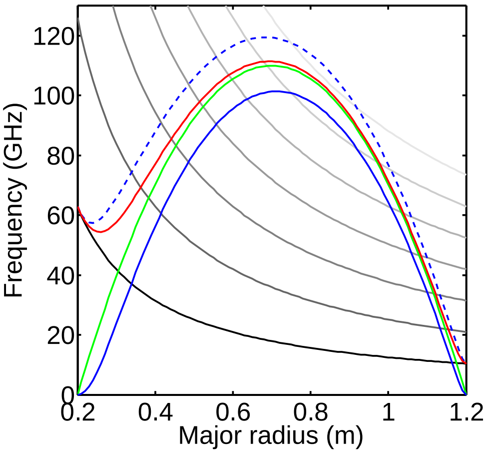

FIGURE 5.1: Perpendicular wave radial propagation. Black: Cyclotron frequency and harmonics. Parabolic from bottom to top: High density cut off (solid blue), plasma frequency (solid green), upper hybrid resonance (solid red), low density cut of (dashed blue). See [3] for more information.

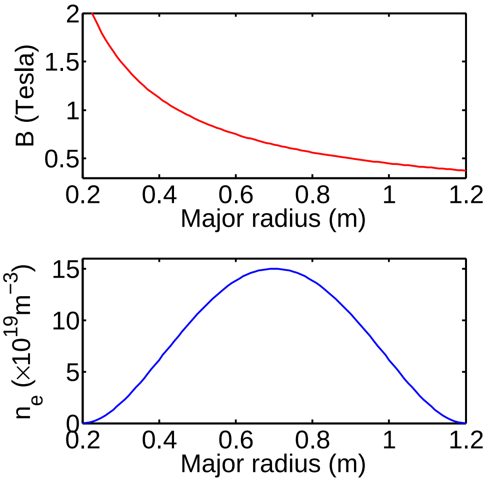

FIGURE 5.2: The toroidal field and density of an example MAST plasma.

5.3 Theory of EBW

5.3.1 Outline of EBW waves

On MAST a new synthetic aperture imaging of EBW emission has been developed with a high speed FPGA digitiser. EBW waves are electrostatic waves. They are formed as electrons gyrate around magnetic field lines, periodic charge accumulation occurs propagating an electrostatic wave [54]. Since the waves are electrostatic they cannot directly couple to the vacuum and be detected. In order to see EBW waves we rely on a process by which the waves are (mode) converted into electromagnetic waves which propogate out of the plasma and into the vacuum. In order to understand EBW waves it is necessary to understand first the propagation of electromagnetic waves in a magnetised plasma, then a description of mode conversion through emission windows is given.

5.3.2 Waves in a cold uniform plasma

5.3.2.1 Summary of theory

The theory aims to get across to the reader that the introduction of a magnetic field in a plasma allows multiple solutions to Maxwell's equations, resulting in waves with different dispersion relations. The propagation of these waves is dependant on their angle to the magnetic field lines and their polarisation. The wave travelling parallel to the magnetic field has three solutions, which are i) left hand circularly polarised wave (L mode), ii) right hand circularly polarised wave (R mode) and iii) the whistler wave (which is also right hand circularly polarised). Ordinary (O) mode is the wave which travels perpendicular to the magnetic field and has a linear polarization such that the electric field is parallel to the magnetic field lines. The electric field induces electron motion parallel to the field lines, so they don't feel the magnetic field so the Ordinary mode dispersion relation applies. eXtraordinary (X) mode is the wave which travels perpendicular to the magnetic field and has an elliptical polarization such that the electric field is perpendicular to the magnetic field lines. For oblique propagation, both O-mode and X-mode are elliptically polarised.

The X mode has two solutions, above and below the plasma frequency. The Fast X (fX) mode has a frequency higher than the plasma frequency, and the Slow X (sX) mode has a frequency lower than the plasma frequency.

5.3.2.2 Waves in a non-magnetised plasma

The electromagnetic wave equation for radiation in a vacuum can be derived from Maxwell equations:

$$\boldsymbol{\nabla} \times \mathbf{E} = -\frac{\partial \mathbf{B}}{\partial t} \tag{5.13}$$

$$\boldsymbol{\nabla} \times \mathbf{B} = \mu_0 \mathbf{J} + \mu_0 \varepsilon_0 \frac{\partial \mathbf{E}}{\partial t} \tag{5.14}$$

Combining the equations we can write:

$$\boldsymbol{\nabla} \times \boldsymbol{\nabla} \times \mathbf{E} = -\frac{\partial}{\partial t}\left(\mu_0 \mathbf{J} + \mu_0 \varepsilon_0 \frac{\partial \mathbf{E}}{\partial t}\right) \tag{5.15}$$

Using the vector identity $\boldsymbol{\nabla} \times \boldsymbol{\nabla} \times \mathbf{E} = \boldsymbol{\nabla}(\boldsymbol{\nabla} \cdot \mathbf{E}) - \boldsymbol{\nabla}^{\mathbf{2}}\mathbf{E}$ and simplifying by assuming $\boldsymbol{\nabla}(\boldsymbol{\nabla} \cdot \mathbf{E}) = \boldsymbol{\nabla}\rho/\varepsilon_0 \ll \boldsymbol{\nabla}^{\mathbf{2}}\mathbf{E}$, which is the same as assuming that the density gradient is much smaller than the electric field gradient, such as in a uniformly dense plasma. We can write the elecromagnetic wave equation

$$\boldsymbol{\nabla}^{\mathbf{2}}\mathbf{E} = \mu_0 \frac{\partial \mathbf{J}}{\partial t} + \mu_0 \varepsilon_0 \frac{\partial^2 \mathbf{E}}{\partial t^2} \tag{5.16}$$

This equation differs from free space by having a non-zero **J** term. Assume the electric field can be described as the real part of the complex equation. Consider a plane wave travelling in the x-direction:

$$\mathbf{E} = \mathbf{E_0} e^{i(kx - \omega t)} \tag{5.17}$$

Where k is the wave number and ω is the angular frequency. Substituting Eq. 5.17 into Eq. 5.16 gives:

$$k^2 = \varepsilon_0 \mu_0 \omega^2 \tag{5.18}$$

The phase term is $kx - \omega t$. Constant phase implies $kx - \omega t = \text{const.}$, so the phase velocity can be written:

$$v_p = \frac{dx}{dt} = \frac{w}{k} \tag{5.19}$$

In vacuum the speed of light is constant ($v_p = c$) so:

$$c^2 = \frac{1}{\varepsilon_0 \mu_0} \tag{5.20}$$

The divergence of the plane wave assuming charge neutrality gives:

$$\boldsymbol{\nabla} \cdot \mathbf{E} = ik\mathbf{E_x} = 0 \tag{5.21}$$

Electrons in a plasma will experience an electric field of an incoming wave producing a current. The force balance of the electron is:

$$m_e \frac{dv_e}{dt} = -e\mathbf{E} \tag{5.22}$$

We identify that velocity is proportional to the electric field:

$$v_y \propto \mathbf{E} \tag{5.23}$$

Substituting Eq. 5.23 into Eq. 5.22 gives:

$$-i\omega m_e v_y = -e\mathbf{E} \tag{5.24}$$

The plasma current **J** is directed in the y-direction:

$$\mathbf{J} = -n_e e v_y = i\frac{n_e e^2}{m_e \omega}\mathbf{E_y} \tag{5.25}$$

Substituting Eq. 5.25 into Eq. 5.16 gives:

$$\frac{\partial^2 \mathbf{E}}{\partial x^2} = i\mu_0 \frac{n_e e^2}{m_e \omega}\frac{\partial \mathbf{E_y}}{\partial t} + \frac{1}{c^2}\frac{\partial^2 \mathbf{E}}{\partial t^2} \tag{5.26}$$

When placing the plane wave equation into this equation we get what is known as the dispersion relation:

$$k^2 = \frac{\omega^2}{c^2} - \frac{n_e e^2}{\varepsilon_0 m_e c^2} = \frac{\omega^2 - \omega_{pe}^2}{c^2} \tag{5.27}$$

The dispersion relation is a useful tool for understanding the propagation of waves in plasmas. The refractive index of a medium is also a useful quantity and defined as the ratio of phase velocities in vacuo and in a medium.

$$N = \frac{kc}{\omega} \tag{5.28}$$

When we calculate the refractive index of the plane wave in a medium:

$$N = \left(1 - \left(\frac{\omega_{pe}}{\omega}\right)^2\right)^{\frac{1}{2}} \tag{5.29}$$

A refractive index of $N = 0$ when $\omega = \omega_p e$ means the wave is at the limit of propagation and is called a cutoff. When $\omega < \omega_{pe}$ the refractive index is imaginary and so the wave attenuated and cannot propagate.

5.3.2.3 Waves in a uniform magnetised plasma

Waves travelling in a uniform magnetised plasma will be affected differently depending on the direction of propagation of the wave with respect to the magnetic field line, since electron motion induced by the wave will see different amounts of the magnetic field. To simplify the mathematics the z-direction is taken for the direction of the magnetic field.

$$\begin{aligned} -m_e i\omega v_x &= -e\mathbf{E_x} - e\mathbf{B_0}v_y & (5.30)\\ -m_e i\omega v_y &= -e\mathbf{E_y} - e\mathbf{B_0}v_x & (5.31)\\ -m_e i\omega v_x z &= -e\mathbf{E_z} & (5.32) \end{aligned}$$

Solving in terms of **E**:

$$\begin{aligned} v_x &= -i\frac{e}{\omega m_e}\frac{1}{1-\omega_c^2/\omega^2}\left(\mathbf{E_x} - i\frac{\omega_c}{\omega}\mathbf{E_y}\right) & (5.33)\\ v_y &= -i\frac{e}{\omega m_e}\frac{1}{1-\omega_c^2/\omega^2}\left(i\frac{\omega_c}{\omega}\mathbf{E_x} + \mathbf{E_y}\right) & (5.34) \end{aligned}$$

Where $\omega_c = e\mathbf{B_0}/m_e$ is the electron cyclotron frequency. The current is given by:

$$\mathbf{J} = -en_e\mathbf{v} = \underline{\sigma} \cdot \mathbf{E} \tag{5.35}$$

The conductivity tensor $\underline{\sigma}$ is given by:

$$\underline{\sigma} = \frac{in_e e^2}{m_e \omega} \frac{1}{1 - \omega_c/\omega^2} \begin{bmatrix} 1 & -i\omega_c/\omega & 0 \\ i\omega_c/\omega & 1 & 0 \\ 0 & 1 & 1 - \omega_c^2/\omega^2 \end{bmatrix} \tag{5.36}$$

We assume as before (but with higher dimensionality) the plane wave form:

$$\mathbf{E} = \mathbf{E_0} e^{i(k.r - \omega t)} \tag{5.37}$$

We define the angle θ to the magnetic field line:

$$k = (0, ksin\theta, kcos\theta) \tag{5.38}$$

When solving the wave equation we can then write:

$$\begin{bmatrix} -N^2 + 1 - \frac{X}{1-Y^2} & \frac{iXY}{1-Y^2} & 0 \\ -\frac{iXY}{1-Y^2} & -N^2 cos^2\theta + 1 - \frac{X}{1-Y^2} & N^2 sin\theta cos\theta \\ 0 & N^2 sin\theta cos\theta & -N^2 sin^2\theta + 1 - X \end{bmatrix} \begin{bmatrix} \mathbf{E_x} \\ \mathbf{E_y} \\ \mathbf{E_z} \end{bmatrix} = \begin{bmatrix} 0 \\ 0 \\ 0 \end{bmatrix} \tag{5.39}$$

Where the following definitions have been made:

$$X = \omega_p^2/\omega^2 \tag{5.40}$$

$$Y = \omega_c/\omega \tag{5.41}$$

The determinant for this equation can be solved for the refractive index giving the Appleton-Hartree formula:

$$N^2 = 1 - \frac{X(1-X)}{1 - X - \frac{1}{2}Y^2 sin^2\theta \pm \left[\left(\frac{1}{2}Y^2 sin^2\theta \right)^2 + (1-X)^2 Y^2 cos^2\theta \right]} \tag{5.42}$$

This is a general formula from which we can understand how the waves travel when there is no magnetic field (see Fig. 5.3), propagate parallel to the magnetic field (see Fig. 5.4) and perpendicular to the magnetic field (see Fig. 5.5).

5.3.3 Applying the Appleton-Hartree formula

5.3.3.1 No magnetic field

No magnetic field implies $Y = 0$:

$$N^2 = 1 - X = 1 - \frac{\omega_p^2}{\omega^2} \tag{5.43}$$

It is trivial to see that the cutoff is at ω_p.

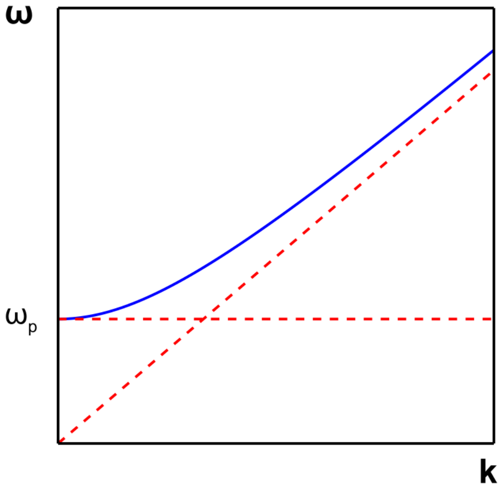

FIGURE 5.3: The dispersion relation for a wave in a uniform plasma without the presence of a magnetic field.

5.3.3.2 Parallel propagation

Parallel propagation implies $\theta = 0$:

$$N^2 = 1 - \frac{X}{1 \pm Y} \tag{5.44}$$

The polarisation for the two different wave solutions:

$$\frac{\mathbf{E_x}}{\mathbf{E_y}} = \pm i \tag{5.45}$$

Which corresponds to left and right handed circular polarisation. There are cutoffs (N=0) at frequencies:

$$\frac{\omega_p^2/\omega^2}{1 \pm \omega_c/\omega} = 1 \tag{5.46}$$

The solution ω_1 is also known as the R-wave since it is right hand circularly polarised:

$$\omega_1 = \frac{1}{2}\left[\left(\omega_c^2 + 4\omega_p^2\right)^{\frac{1}{2}} + \omega_c\right] \tag{5.47}$$

The solution ω_2 is also known as the L-wave since it is left hand circularly polarised:

$$\omega_2 = \frac{1}{2}\left[\left(\omega_c^2 + 4\omega_p^2\right)^{\frac{1}{2}} - \omega_c\right] \tag{5.48}$$

The other solution is the whistler wave which sees a resonance ($N \rightarrow \infty$) at $\omega = \omega_{ce}$. Such waves are able to travel along the earths magnetic field lines from one hemisphere to the other.

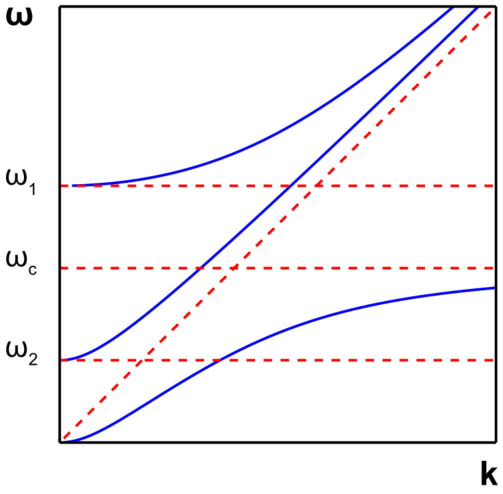

FIGURE 5.4: The dispersion relation for a wave in a uniform plasma parallel to the magnetic field.

5.3.3.3 Perpendicular propagation

Perpendicular propagation implies $\theta = \pi/2$. There are two physical solutions. The first solution is the same as if the magnetic field is not present and corresponds to the O (Ordinary) mode:

$$N^2 = 1 - X \tag{5.49}$$

With polarisation:

$$\mathbf{E_x} = \mathbf{E_y} = 0 \tag{5.50}$$

The second solution corresponds to the X (Extraordinary) mode:

$$N^2 = 1 - \frac{X(1-X)}{1-X-Y^2} \tag{5.51}$$

With polarisation:

$$\frac{\mathbf{E_x}}{\mathbf{E_y}} = -i\left(\frac{1-X-Y^2}{XY}\right) \tag{5.52}$$

$$\mathbf{E_z} = 0 \tag{5.53}$$

The cutoffs ($N = 0$) are at:

$$\frac{\omega_p^2/\omega^2}{1-\omega_c^2/(\omega^2-\omega_p^2)} = 1 \tag{5.54}$$

The Fast X-mode (fX) solution:

$$\omega_1 = \frac{1}{2}\left[\left(\omega_c^2 + 4\omega_p^2\right)^{\frac{1}{2}} + \omega_c\right] \tag{5.55}$$

The Slow X-mode (sX) solution

$$\omega_2 = \frac{1}{2}\left[\left(\omega_c^2 + 4\omega_p^2\right)^{\frac{1}{2}} - \omega_c\right] \tag{5.56}$$

$$\omega = \omega_p \tag{5.57}$$

The resonances ($N \to \infty$) also known as the upper hybrid resonance (UHR) is:

$$\omega^2 = \omega_p^2 + \omega_c^2 \tag{5.58}$$

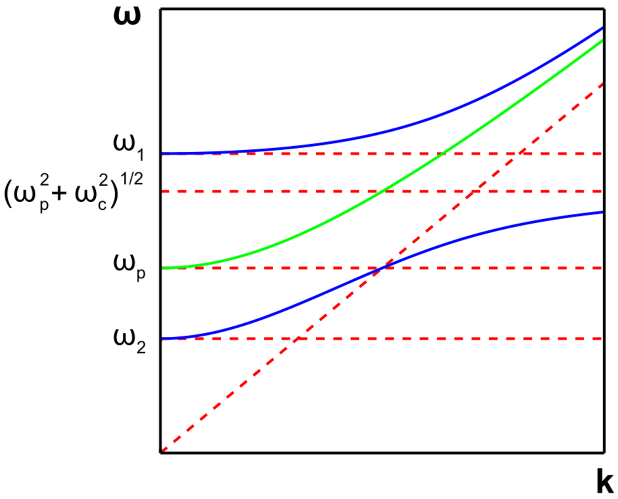

FIGURE 5.5: The dispersion relation for a wave in a uniform plasma perpendicular to the magnetic field.

5.3.4 Mode conversion

5.3.4.1 Bernstein mode

Different modes have been introduced and the focus has been on the O and X mode. Figure 5.1 shows that in an overdense ($\omega_{pe} > \omega_{ce}$) plasma that the cutoffs are near the edge of the plasma. This means that the O or X mode cannot directly couple to the vacuum. As mentioned in Section 5.2.2.2 Electron Bernstein Waves (or the Bernstein mode) have no high density limit and when they propagate to the upper hybrid resonance (UHR) they are absorbed and so can be used for heating and current drive. The Bernstein mode is a result of electron thermal motion and subject to warm dispersion theory which is complex and is not covered in this thesis. Warm dispersion theory [55, 56] shows the Bernstein mode couples to the slow X (sX) mode and so can indirectly couple to the vacuum via mode conversion.

5.3.4.2 Description of O-sX-B mode conversion

There are different types of mode conversion, direction conversion from X mode to Berstein mode (direct X-B tunneling/conversion), O-sX-B conversion and others. This section will focus on O-sX-B mode conversion which is the primary process by which the Bernstein mode can couple to the vacuum for typical overdense MAST plasmas. The mode conversion occurs via the following process: An O mode beam is launched at an angle towards a field line, if the angle is such that it is not so shallow the beam will refract away and out of the plasma, and not so large that is will hit the O mode cut off and be reflected, but if it is at just the right angle it will refract and become directly parallel to the magnetic field line at the O mode cutoff. At this point the frequency is below the UHR frequency, and above the sX cutoff but below the fX cutoff; the wave is now an sX mode, which is still undergoing refraction to a low density region of plasma, but since it is an sX mode it will hit the UHR resonance and be converted to the Bernstein electrostatic mode which can then propagate through the plasma.

5.3.4.3 Optimum mode conversion angle

The requirement that the mode conversion can only happen at an optimum angle has been solved analytically [57, 58]. The model under consideration is a cold plasma in which there is a uniform magnetic field, and a linear density gradient which is at an angle to the magnetic field. The uniform magnetic field assumption is valid generally in a tokamak plasma where the density changes are much larger than the changes in magnetic field. This problem is greatly simplified by considering the refractive index parallel ($N_{\|}$) and perpendicular ($N_{\perp}$) to the increasing density gradient. $N_{\|}$ depends only on B which is constant, therefore only $N_{\perp}$ which is changing perpendicularly to the magnetic field needs to be calculated.

Mjølhus makes the assumption that mode conversion occurs when the refractive index of two different modes is equal at the same place in the plasma (i.e. the same X which is proportional to density). This can be identified when plotting the Appleton-Hartree formula against X. At $\theta = 0$ and $X = 1$ (see Fig. 5.6) which means this mode conversion occurs only when the wave is travelling purely parallel to the field line at the O-mode cutoff layer. The wave can meet this condition if injected obliquely (see Fig. 5.7) at the correct angle such that it will refract being precisely parallel at the O-mode cutoff.

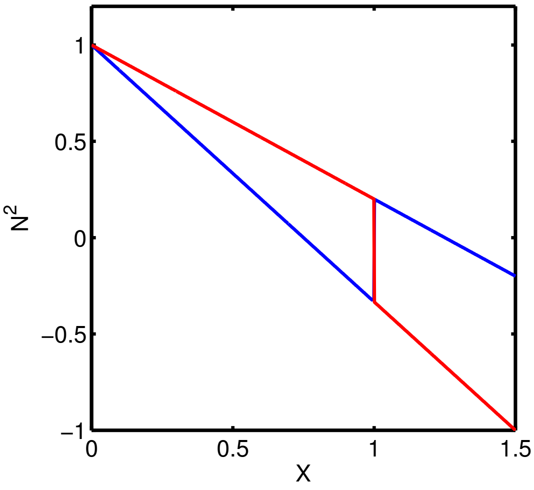

FIGURE 5.6: $\theta = 0, X = 1$.

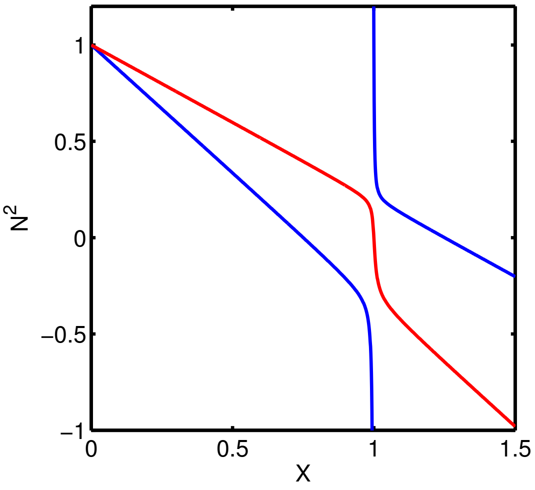

FIGURE 5.7: $\theta \ll 0, X = 1$.

These images only demonstrate the mode conversion condition ($\theta = 0$ and $X = 1$) where mode conversion occur, but not that the refractive index follows this equation in general, since the wave is generally not propagating only parallel to the field lines. The refractive index through the slab is a function of both a constant $N_{\|}$ and the changing (due to changing density) $N_{\perp}$. Since the propagation parallel to the magnetic field is constant, any propagation formula which satisfies the mode conversion condition satisfies the constant parallel refractive index denoted by $N_{\|,MC}$. Thus evaluating the equation of the refractive index $N_{\|}^2 = 1 - \frac{X}{1 \pm Y}$ at $X = 1$ allows us to identify:

$$N_{\|,MC}^2 = \frac{Y}{1+Y} = \text{const} = cos(\theta) \tag{5.59}$$

5.3.5 Optimal mode conversion windows on a MAST plasma

The SAMI system views in 2D, and so a MAST plasma will have two mode conversions windows (see Fig. 5.8 and Fig. 5.9), where the line between the two windows is along the magnetic field line at the O-mode cutoff. **By imaging these conversion windows it is possible to obtain a measurement for the pitch angle** at the cutoff. The cutoff is radially localised according to the frequency of emission.

As shown in Eq. 5.59 and Mjølhus [58] the optimal O-sX mode conversion angle, where we have made the assumption that the increasing density gradient is perpendicular to the magnetic field:

$$cos\,\theta_{MC} = \sqrt{\frac{Y}{Y+1}} \tag{5.60}$$

Where $Y = \omega_c/\omega$ and θ_{MC} is the angle of the incoming ray to the magnetic field. Considering that EBW emission only occurs when $\omega > \omega_c$ this means that $Y > 1$, meaning that $0 < cos\,\theta_{MC} < 1/\sqrt{2}$ or $90^o < \theta_{MC} < 45^o$. Therefore the optimum MC angle will always range from being perpendicular to the plasma surface to 45 degrees. Hansen [59] gives us the equation for the transmissivity as:

$$T = exp\left(-\pi k_0 L \left(\frac{Y}{2}\right)^{\frac{1}{2}} \left[(N_z - N_{\parallel,MC})^2\; 2(1+Y) + N_y^2\right]\right) \tag{5.61}$$

Where N_z and N_y are projections of the incoming/outgoing ray which are well described by Igami [4]. k_0 is the vacuum wavenumber and L is the density scale length. The density scale length changes the apparent size of the window, but not its position. A larger density scale length corresponds to a smaller evanescent layer, which means the window will appear larger.

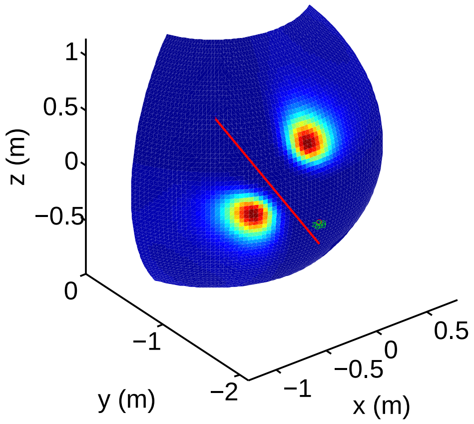

FIGURE 5.8: A spherical plasma with 1.4m radius and a $1/R$ toroidal field defined as 0.6T at 1m. The antenna array is the standard SAMI (see Section 5.4) antenna configuration. Frequency 20GHz. Density scale length is chosen such that $L/\lambda = 0.7$. Other parameters are chosen such that $1/Y = \omega/\omega_c = 1.67$. These values are comparable with Igami's MC survey (Fig. 2.12 of [4]). The transmissivity is shown for a 45^o pitch angle calculated by evaluating the N_z and N_y from the antenna to every point on the surface.

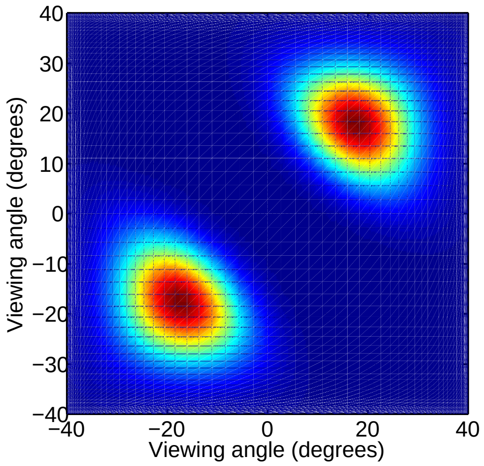

FIGURE 5.9: The transmissivity as would be viewed by the antenna array.

5.4 Synthetic aperture microwave imaging hardware

5.4.1 Analogue hardware

5.4.1.1 Overview

The Synthetic Aperture Microwave Imaging (SAMI) system has 8 receiving antennas, with a frequency switchable local oscillator (LO) used for superheterodyne down-conversion. The different frequencies probe different radial positions of the plasma. Generally frequency of emission corresponds to radiation in the pedestal of the plasma. Due to the high density gradient of the plasma it is possible to get high radial resolution of plasma emission giving more information about what is happening in the edge of the plasma and potentially pitch angle and 2D current density measurements. One of the most technically challenging parts of this system is the large bandwidth of the system $\sim 6 - 40$GHz.

5.4.1.2 Antipodal Vivaldi antenna

The SAMI system uses antipodal Vivaldi antennas where the electric field (polarisation) lies in the plane of the antenna (see Fig. 5.10). A good antenna will match the impedance of free space ($\sqrt{\mu_0/\varepsilon_0} \approx 377$ Ohms) to the transmission line (50 Ohms). By changing the alignment of the antenna to the magnetic field lines of the plasma different modes (O and X) can be selected. We are assuming the antenna is directed at the plasma and so perpendicular from that sense, but the mode selection relates to the polarisation (perpendicular or parallel) with respect to the field lines. If a pure polarisation is not selected (pure perpendicular or parallel) then the incident ray will split into O and X mode which will propagate independently [57]. If the electric field is aligned perpendicular to the magnetic field lines then X mode is selected, if the plane of the antenna is aligned parallel to the field lines then O mode is selected. The antenna is broadband and therefore low gain and so sees emission from the plasma in every direction. Therefore the signal received by the antenna array is a mixture of O and X mode. In high density (H-mode) plasmas the O and X cutoff are close to each other which may mean the O and X mode signal will beat together. It has been shown that by having a duplicate antenna array with orthognal polarisations it would be possible to select the polarisation of emission viewed by the antenna [60], however with the current antenna array configuration this is not possible.

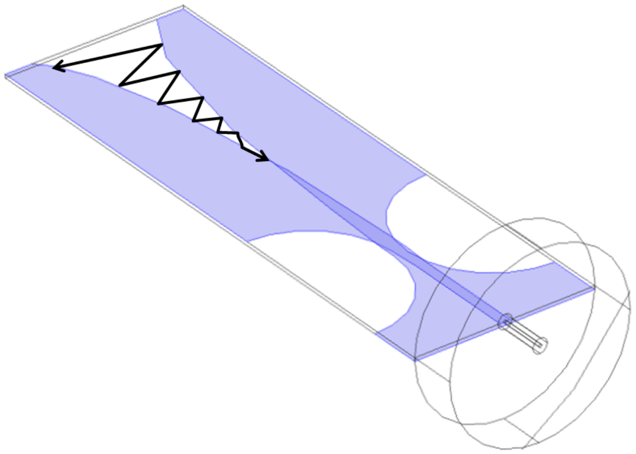

FIGURE 5.10: The electric field in the plane of the antipodal Vivaldi antenna. Credit: Vladimir Shevchenko.

5.4.1.3 Frequency switched LO

There are 16 available LO frequencies. A fast switching device with 200ns settling time is used. Generally each frequency is acquired for 10us. A sweeping LO cannot be used since it is desirable to measure at a fixed radial location and have a phase stable oscillator for doing cross correlations used in synthetic aperture imaging. The LOs are chosen such that they have very low phase noise, since it is necessary to have a good I/Q downconversion where we care about the phase.

5.4.1.4 Quadrature downconversion

For phased array imaging it is necessary to have the phase information from the RF down to the IF stage. This is achieved by doing quadrature downconversion (See Fig 5.11) using a 90^o hybrid coupler. One consequence of using a broadband component is the I and Q may not be equally balanced in power, which is crucial for side band separation (SBS). This power rebalancing can be performed in software on the separate digitised I and Q channels resulting in good sideband separation.

$$cos\,\theta\ cos\,\phi \sim cos(\theta-\phi)+cos(\theta+\phi)=[\text{lowpass}]=cos(\theta-\phi) \tag{5.62}$$

$$cos\,\theta\ sin\,\phi \sim sin(\theta-\phi)-sin(\theta+\phi)=[\text{lowpass}]=sin(\theta-\phi) \tag{5.63}$$

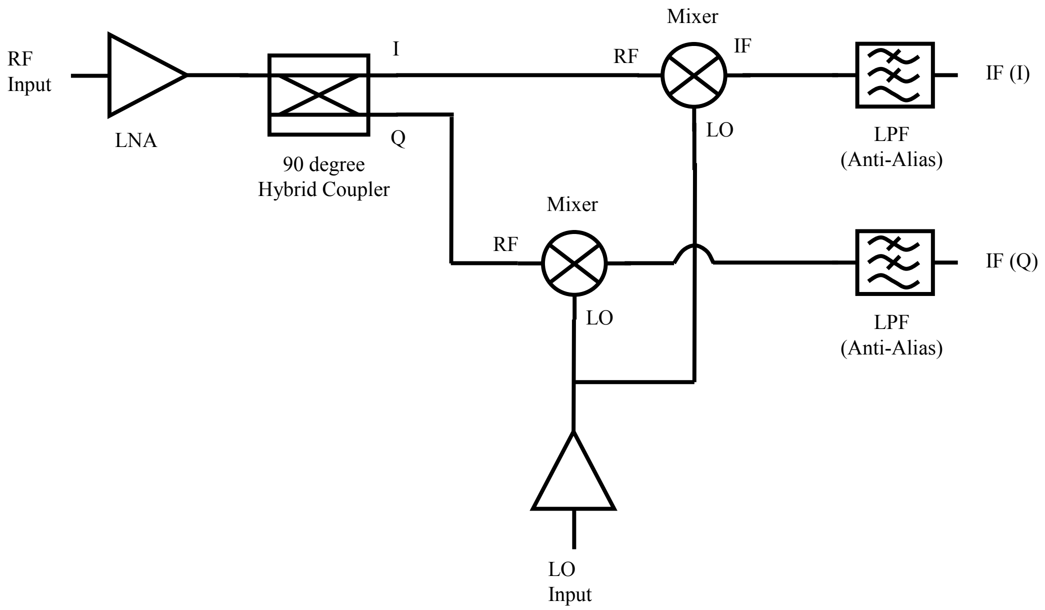

FIGURE 5.11: A schematic of the microwave components for analogue downconversion.

5.4.1.5 Side band separation (SBS)

Side band seperation is needed for the following reason: when we mix the signal received by the antenna with the LO, for example 20GHz, and digitise, we are in fact digitising 20GHz±125MHz. When we do this the signal below the LO (negative frequencies or lower sideband) and above the LO (positive frequencies or upper sideband) are folded onto each other. We need the I and Q in order to seperate out the upper and lower sideband otherwise we cannot do anything useful with the signal. The exception to this is intensity interferometry (see Section 5.5). When using a hybrid coupler to create a 90^o shifted signal one issue is that it is difficult to get a component which works accurately over a large bandwidth. As such it would be nice if the perfect quadrature signal can be reconstructed even without a perfect phase shifter. In fact there is such a method, which is proved in Equation 5.74. It works well down to a phase shifter that does a 10^o shift instead of 90^o. Additionally the algorithm could be easily implemented in an FPGA but this is not currently done for the SAMI system. The correction below to recover a perfectly shifted quadrature signal should always be applied after power rebalancing of the I and Q channels.

Our local oscillator (LO) signal, is a single frequency source such as a single mode laser or signal generator (represented by $\cos(\theta)$). Our (RF) signal can contain multiple frequencies, such as a light source or plasma (represented by $\cos(\phi)$).

The inphase downconverted component is obtained by mixing the LO with the RF signal:

$$\cos(\theta)\cos(\phi) = \cos(\theta - \phi) + \cos(\theta + \phi) \tag{5.64}$$

The signal is low pass filtered. This lowpass filter can act as an anti-alias filter on the digitiser. This signal is also known as the “in-phase” or I component. The substitution $\alpha = \theta - \phi$ is used.

$$I = \cos(\theta)\cos(\phi) = [\text{Lowpass}] = \cos(\alpha) \tag{5.65}$$

The “quadrature” or Q component may also be obtained by phase-shifting the RF signal by 90 degrees.

$$Q = \cos(\theta)\sin(\phi) = [\text{Lowpass}] = \sin(\alpha) \tag{5.66}$$

However what if we phase-shift the signal by an unknown amount normally our SBS would be compromised. This is particularly a problem at high frequencies where precise phase shifting such as at optical frequencies requires nanometer precision for sub 10 degree accuracy. The “unknown-phase” or U component is defined as:

$$U = \cos(\theta)\cos(\phi + \delta) = [\text{Lowpass}] = \cos(\alpha - \delta) \tag{5.67}$$

So we assume that we now have two components digitised, the I and U component. First we calculate the phase difference (δ) between them. In standard interferometry it is well known that the average mutual intensity between two waves is related to its phase difference [61]:

$$\frac{\langle E_1 \cdot E_2 \rangle}{\sqrt{I_1 I_2}} = \cos(\delta) \tag{5.68}$$

Another way of writing this, where the I and U signals are real signals which have been normalised by the square root of their average power:

$$\langle \cos(\alpha)\cos(\alpha + \delta) \rangle = \langle \cos(\delta) + \cos(2\alpha + \delta) \rangle = \cos(\delta) \tag{5.69}$$

Thus the phase difference δ between I and U is known. Next comes the correction, we wish to obtain $\sin(\alpha)$.

$$\cos(\alpha + \delta) = \cos(\alpha)\cos(\delta) - \sin(\alpha)\sin(\delta) \tag{5.70}$$

$$\frac{\cos(\alpha + \delta)}{\cos(\delta)} = \cos(\alpha) - \sin(\alpha)\tan(\delta) \tag{5.71}$$

$$\sin(\alpha)\tan(\delta) = \cos(\alpha) - \frac{\cos(\alpha+\delta)}{\cos(\delta)} \tag{5.72}$$

$$\sin(\alpha) = \frac{1}{\tan(\delta)}\left(\cos(\alpha) - \frac{\cos(\alpha+\delta)}{\cos(\delta)}\right) \tag{5.73}$$

$$Q = \frac{1}{\tan(\delta)}\left(I - \frac{U}{\cos(\delta)}\right) \tag{5.74}$$

Where $\delta = \cos^{-1}(\langle I\ U\rangle)$.

5.4.1.6 Single side band (SSB) upconversion for active probing

Active probing involves injecting a signal onto the plasma which is then received by the phased array. The active probing is generated at the IF and then “upconverted” to the RF using upconversion electronics (see Fig. 5.12). Possible measurements include reflectometry, scattering and doppler shifted signal. An additional use is that if the active probing signal is only present in one sideband (one side of the LO or single sideband) then the quality of the side band separation used can be tested.

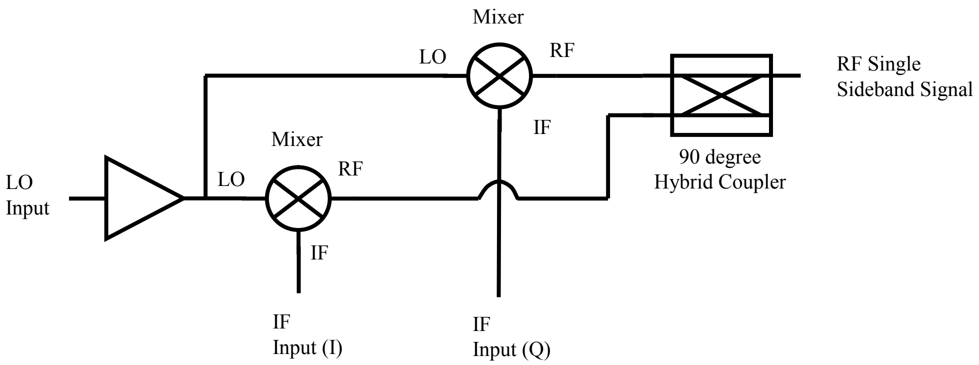

FIGURE 5.12: A schematic of the microwave components for analogue upconversion.

The mathematics to achieve upconversion is shown below. After the mixer stage we have:

$$cos\,\theta\ cos\,\phi \sim cos(\theta-\phi) + cos(\theta+\phi) \tag{5.75}$$

$$cos\,\theta\ sin\,\phi \sim sin(\theta-\phi) - sin(\theta+\phi) \tag{5.76}$$

Then the 90^o hybrid will do a Hilbert transform one of the signals, and add them together:

$$cos(\theta - \phi) + cos(\theta + \phi) \tag{5.77}$$

$$cos(\theta - \phi) - cos(\theta + \phi) \tag{5.78}$$

Clearly when added only the $cos(\theta - \phi)$ or $sin(\theta + \phi)$ signal will remain, i.e. our input signal $cos(\phi)$ is only present in one sideband.

This can be simulated in MATLAB where $s1$ and $s2$ are complex signals. The Hilbert transform below is showing the phase shifting property of the hybrid. A the addition/-subtraction demonstrates the coupling (summation) property of the hybrid.

SSB MATLAB Code

```
upper = real(s1).*real(s2) - imag(hilbert(real(s1).*imag(s2)))
lower = real(s1).*real(s2) + imag(hilbert(real(s1).*imag(s2)))
```

5.4.2 FPGA I/Q generator for a bandwidth limited single side band (SBS) microwave source

5.4.2.1 FPGA based filtering using the convolution theorem

An FPGA can be used to perform filtering or provide a Hilbert transform. These are implemented using convolutions of an input signal with a set of coefficients. This is best understand by the convolution theorem.

The convolution theorem states:

$$F(f * g) = F(f) \cdot F(g) \tag{5.79}$$

Where $F(f)$ is the filter in Fourier space and g is the signal. The coefficients then used for the convolution (f) can be found by doing an inverse transform of the filter. The convolution theorem allows multiple filters to be combined by convolving filters with each other resulting in a single set of coefficients. The set of coefficients is also referred to as a Finite Impulse Response (FIR) filter. It should be noted that if a filter is required by one channel, such as a Hilbert transform, but then not by another channel, a delta function introducing group delay should be used to ensure that the phase of the signals is aligned as required. Additionally the filter applied by convolution operates entirely in the real and imaginary domain.

The convolution theorem is used to generate the I and Q channels for bandwidth limited white noise or single frequency source which is used to create a single side band source. Injecting noise (active probing) is useful since the signal reflected and scattered by the plasma is of higher power than the signal generated solely by the plasma, increasing the effective signal to noise of the signal received from the plasma. Using noise means the coherence length will be shorter so interference effects which distort the reconstructed image using the phased array should be reduced.

5.4.2.2 FPGA I/Q system

A high speed FPGA I/Q generator (up to 500MSps) has been built (see Fig 5.17) which has advantages over an analogue system, such as excellent I/Q power balance and constant 90^o phase shift over a large bandwidth. The FPGA based system is shown (see Fig. 5.13 and Fig. 5.14) to provide a peak side band separation of 25dB which is a 10dB

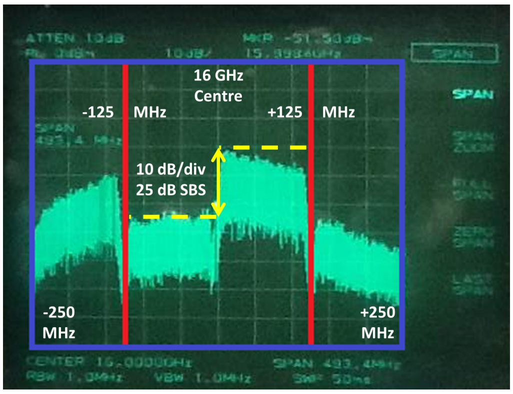

FIGURE 5.13: Data from a spectrum analyser with centre frequency at 16 GHz. The signal generated by the FPGA box at 250 Msps has a total bandwidth (when summing the bandwidth of the I and Q channels) of 250 MHz. This is indicated by the red lines at ±125 MHz which also corresponds to the maximum intermediate frequency (IF) bandwidth of the SAMI system.

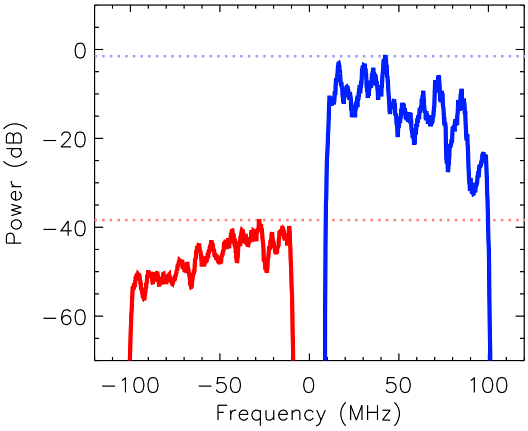

FIGURE 5.14: Data from the noise signal with the same centre frequency of 16 GHz injected into (sector 11 of) the MAST tokamak and received by the SAMI system. The data are bandpass filtered from 10 to 100 MHz. Side band seperation of at least 25 dB is seen, confirming the spectrum analyser results.

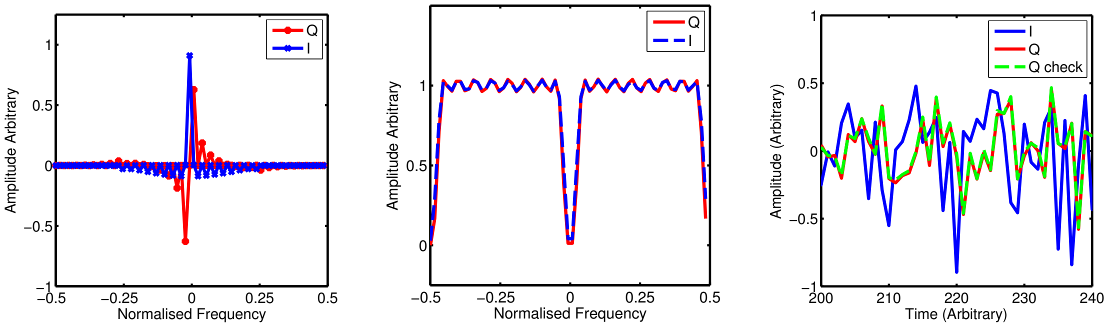

FIGURE 5.15: Left to right: i) The I and Q coefficients, ii) The absolute Fourier magnitude (frequency response) of the coefficients, iii) Simulated time data from the noise generator with a comparison Q from an FFT Hilbert transform and the Q (check) from an FIR (coefficient based) Hilbert transform. .

improvement over an entirely analogue implementation. A dual channel 12-bit DAC3162 EVM board is used, with an FMC adapter card. Two different baseboards are used, a Zedboard (Avnet) with ZYNQ FPGA and an SP601 board (Xilinx) with Spartan 6 FPGA. Using the Vita 57.1 FMC standard allowed easy porting of the DAC to different FPGA baseboards. The high speed of the DAC is made even more demanding due to the DDR (1Gsps) used to drive the DAC. The I channel is on one edge of the clock and the Q channel is on the other edge. In order to meet the timing constraints of such a high speed system and achieve the maximum frequency a special code was developed (PUCF). See Fig. 5.19 and Fig. 5.20 for the improvements to the FPGA routing using the PUCF code.

Simulink in conjunction with System Generator (see Fig 5.16) has been used to implement a Linear Feedback Shift Register (LFSR) based noise source (see Fig 5.18) and FIR filters for both the I and Q channels (see Fig. 5.15). In fact two LFSRs were combined to create a flat frequency response. Any given upconverter must result in equal power for the I and Q channel. The Q channel therefore was simulated and an amplitude correction was performed by a multiplication in the FPGA to ensure power balance. In testing the I and Q channels inputs were swapped with a single frequency generator (instead of the LFSR noise generator) with a cosine signal on the I channel and a sine signal on the Q channel. The sine signal is Hilbert transformed back to a cosine which should be 0^o apart across the bandwidth and useful for checking group delays. A delay of one or more clock cycles can be corrected for by shifting the index of the coefficients in the I channel.

The FPGA system although tested and proved capable of running with a 500 MHz clock was reduced to 250 MHz since the SAMI acquisition system (Section 5.4.3) is limited by this rate. The FIR filter has a bandpass of 10 MHz to 115 MHz. Any required bandwidth can be selected by choosing the appropriate coefficients, however the more complex the filter and the greater the roll off and/or smaller the ripple, the larger the number of coefficients needed, potentially requiring a larger FPGA device.

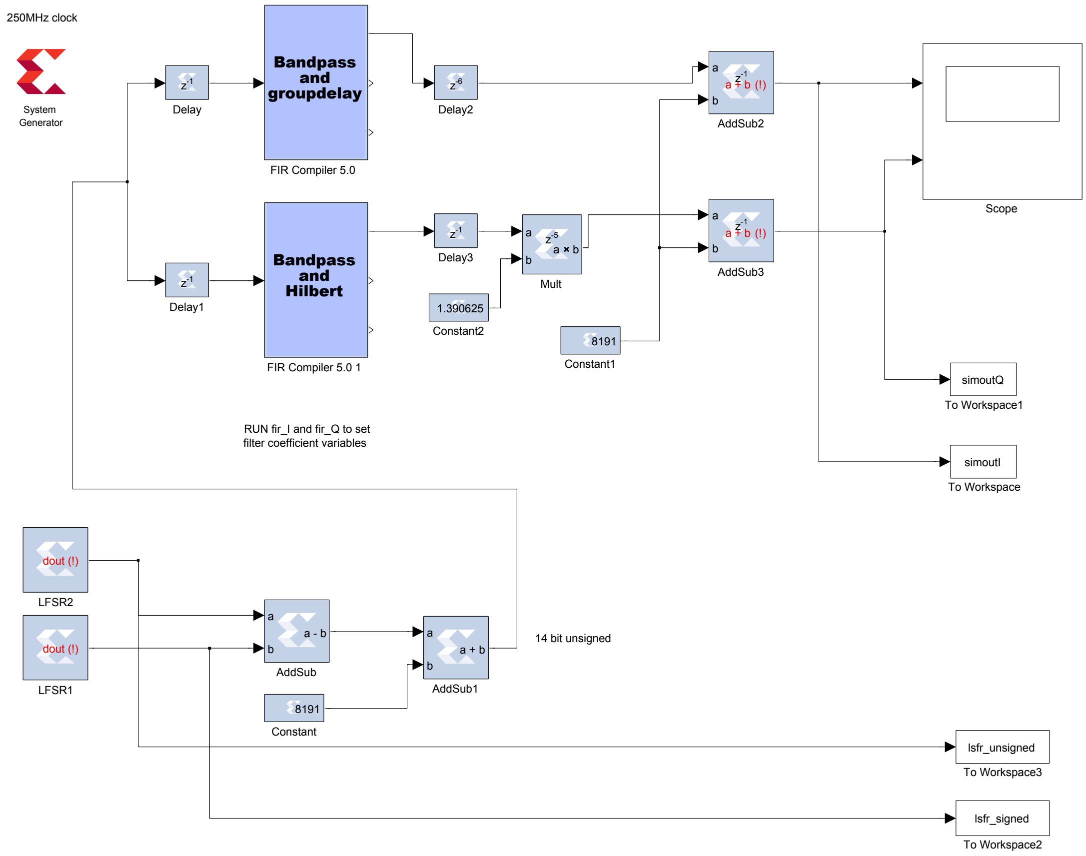

FIGURE 5.16: The Simulink model which combines the LFSR noise generator with a band-pass filter and Hilbert transform to create the I and Q components for upconversion to microwave frequencies.

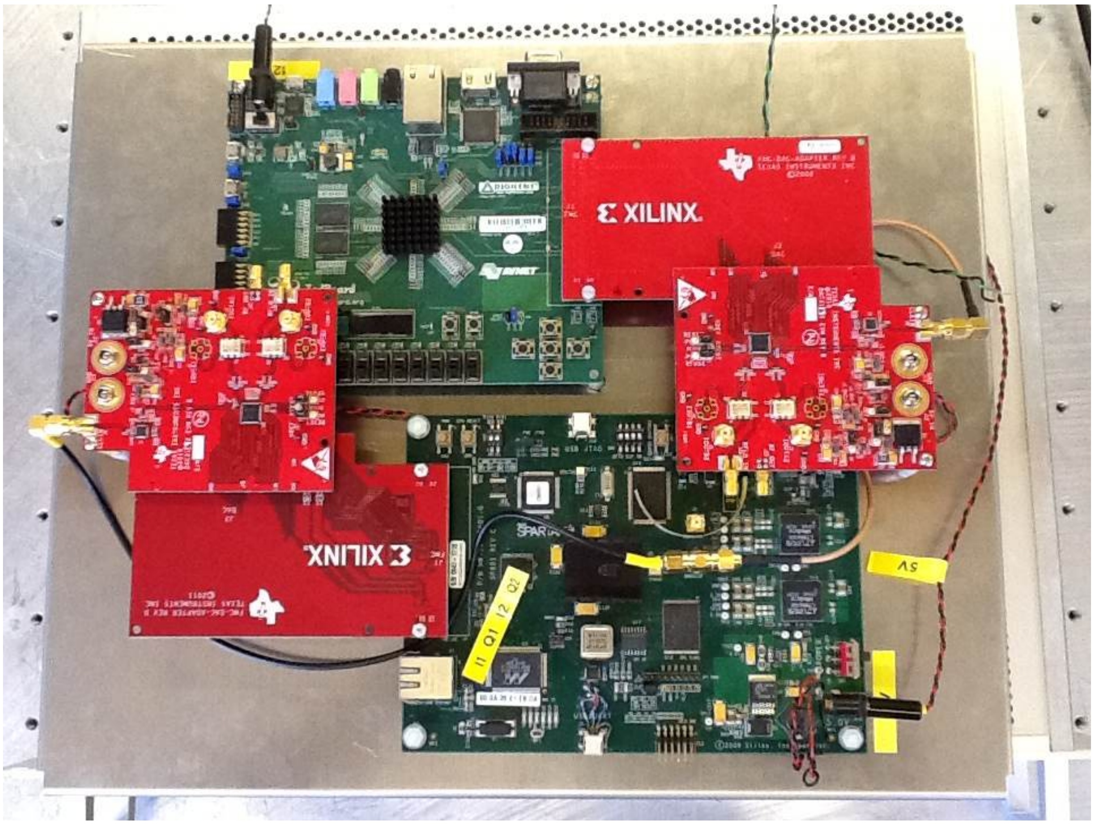

FIGURE 5.17: FPGA based I/Q generator using DAC3162 500MSps 12-bit on the Zedboard and SP601 baseboards. The boards have a synchronised clock which is either sourced externally, or internally from the SP601.

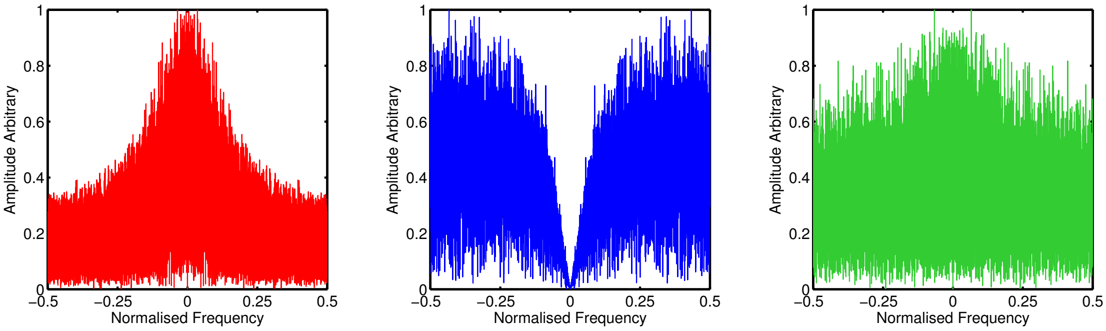

FIGURE 5.18: Left to right is the Fourier spectrum of the noise generated by a Linear Feedback Shift Register: i) LFSR (unsigned), ii) LFSR (signed), iii) LFSR (unsigned - signed).

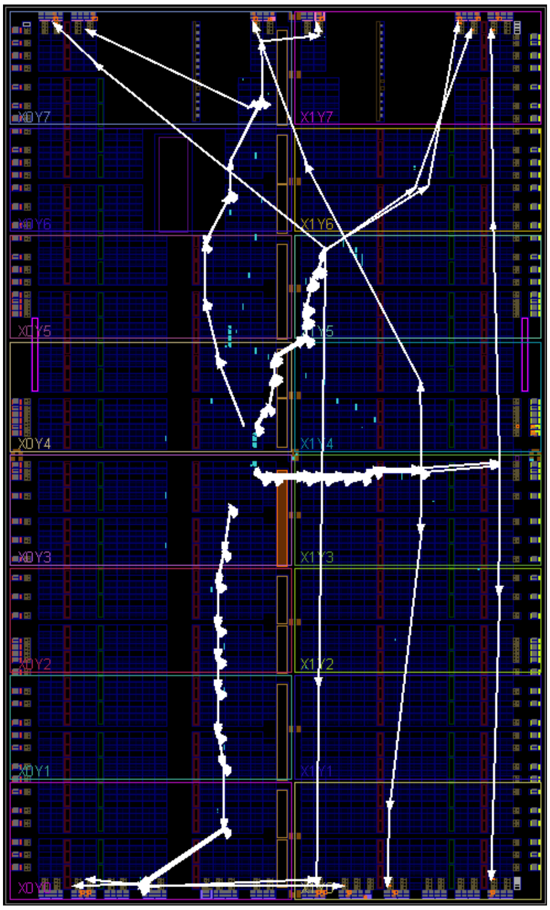

Figure 5.19: The standard routing of buffer flip-flops by the Xilinx tools to take data from the centre of the FPGA device to the data pins at the top and bottom edges of the FPGA die. The routing is sub-optimal since there are some very long data path delays due to flip flops not beeing placed equally apart.

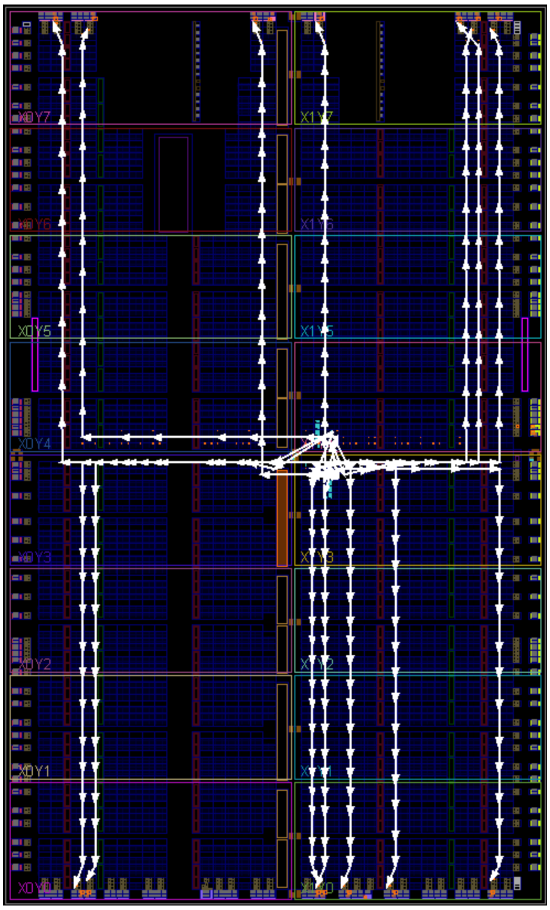

Figure 5.20: A specialised enhanced placement tool (PUCF) which generates predefined location constraints for flip-flops to transfer data from the middle of the FPGA to the device. With the addition of this enhanced placement the design can be driven at 500MHz DDR, pushing the FPGA to it's limits. Without this optimisation the design would not meet timing requirements at this high frequency. PUCF allows the high speed design to be transferred from one FPGA to another, the design shown here runs on the SP605, SP601 and Zedboard.

5.4.3 FPGA based data acquisition system

5.4.3.1 Overview of the data acquisition system

A high speed data acquisition system (see Fig. 5.21) has been developed using FPGAs [62]. It has 16 ADC channels operating at 250 MSPS, at 14-bit resolution acquiring continuously at 8GB/s for 0.5 seconds. The system uses the Virtex 6 FPGA running embedded Linux (TokaLin specifically designed for Fusion) on the MicroBlaze$^{\mathrm{TM}}$ soft processor. The development of a standard FPGA architecture has enabled us to develop this system using Commercial-Off-The-Shelf (COTS) components. This architecture can easily be modified for a variety of applications, both high and low performance at a competitive cost in terms of hardware, engineering and development.

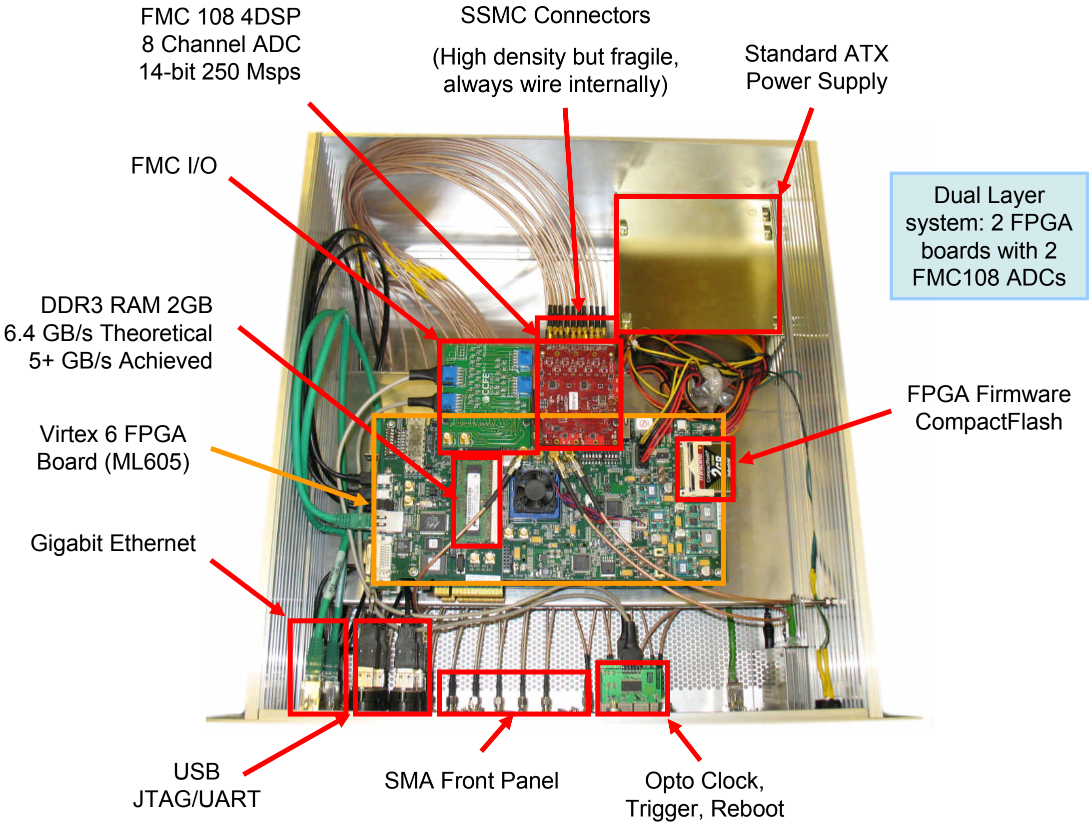

Figure 5.21: The MAST EBW digitiser with two Xilinx ML605 boards with the Virtex 6 FPGA and two 4DSP FMC108 ADC boards. Totalling 16 ADC channels of 250 MSPS at 14-bit resolution acquiring at 8GB/s for 0.5 seconds.

5.4.3.2 Developing a phased array acquisition system

In a phased array system the first criterion to define is the desired phase accuracy at the RF frequency. So for example if we are at 20GHz, and we desire a phase accuracy of 1 degree, we should note that ideally we would know the path lengths through the system (including cables, components, waveguides etc) to an accuracy of the time period $(1/f)/360$ which is 50ps/360 = 140fs for the RF paths. For IF paths the phase is related to the IF digitisation frequency and generally is a much less demanding requirement. At high frequencies it is not reasonable to assume that matched length cables and electrical signal paths are sufficient to ensure the required phase accuracy. We have also neglected the complication of different frequency responses (dispersion) in transmission lines. Instead we must assume that an arbitrary time lag is present between channels. The way to measure this lag is to have a frequency sweep in the RF. The gradient of the phase between antennas as a function of frequency is proportional to the time lag $(\Delta t = \partial\phi/\partial\omega)$. The time lag can then be corrected for between antennas in software by applying the $\partial\phi/\partial\omega$ correction in the Fourier transform. It should be noted that arbitrary time lag correction is only a good approximation up to half of the Nyquist (a quarter of the sampling frequency) otherwise modulation in the signal will result.

For calibration it is important to determine a known phase (δ) relationship between antennas. This can be done by introducing a noise source into the vacuum vessel, and then looking at $cos\ \delta = \langle S_1 S_2 \rangle$ [61] where S_n is the antenna signal after side band seperation and time lag correction.

5.4.4 Performance

The total acquired data per acquisition (0.5 seconds) is just under the 4 GB of the 2×SODIMM RAM boards. It is actually 3840 MB since each board reserves 128 MB for the embedded Linux. The system is actually capable of acquiring at 10 GB/s. Theoretically it is capable of 12.8 GB/s since the memory is 400 MHz DDR (800 MT/s) at 64-bits equating to 6.4 GB/s for each of the two FPGA board. Thus the actual performance efficiency is 80% compared to the theoretical which is a good result. The full performance is never achieved due to the need for dynamic memory refresh etc.

5.4.5 Components

The high required bandwidth of 8GB/s was too challenging for a single board so to halve the requirement two identical FPGA boards (ML605s) were used each with an FMC108 4DSP ADC. The FMC standard was utilised to enable the FMC108 reference design to be ported to any FPGA board which supports the FMC standard. This means that the system can be ported to other FPGA baseboards in future, such as those taking advantage of the Zynq FPGA with embedded dual core ARM processor.

The onboard embedded linux is crucial for enabling access to a multitude of linux drivers such as those which communicate over the SPI interface to the ADCs, or which enable access via an embedded web server for configuration and access to a custom ethernet driver for fast data transfer using the StarkStream protocol (See Section 2.5.2).

A standard ATX power supply is used to provide a number of different standard voltages, allows remote hard optical reboot and a watchdog based reboot in case of an operating system failure or other hang-up of FPGA functions.

5.4.6 FPGA programming

Whenever an FPGA model is resynthesized, one issue is that the logic will generally have a completely different routing even for small changes. Given the high frequency of the DAC and high speed of the FPGA logic and the desire to have good phase accuracy one challenge to deal with is the different signal propagation times within the FPGA which can completely change the timing of the FPGA logic. This means that resynthesis can break the behaviour of the system resulting in misalinged triggers and glitches on ADC or DAC data. This can be avoided by specifically locking down parts of the FPGA code, but this was not done for this system, instead variable delays on the Virtex 6 on the input/output pins allows us to compensate changes due to routing. One issue however is that the trigger and clock is sent to both boards, and if the trigger and clock edge happen to be close to each other on either board then this can result in a trigger on a different clock edge from one board to the next which results in a 4ns time lag between channels. This can only be compensated for if a $\partial\phi/\partial\omega$ plot from a frequency sweeping source (or similar) shows a 4ns gradient. Without any possibility to compensate for time lags in software then this must be compensated for in hardware. The software compensation is desirable since temperature can change. Hardware compensation will not necessarily account for temperature changes.

5.5 Intensity Interferometery

The EBW mode conversion emission windows from an overdense plasma is analogous to imaging binary stars in astronomy. Image reconstruction techniques used in astronomy can be applied to the reconstruction of EBW emission window images. There are different techniques and each have their different advantages and disadvantages. They have different attributes of complexity of implementation, sensitivity and robustness. Intensity interferometry is one such technique and uses intensity fluctuations, which has the benefits of easier implementation and robustness at the cost of reduced sensitivity. This section explains and explores the possibility of using this technique for image reconstruction on the SAMI system (and shows that the current 8 antenna system is not sufficient), compares the technique to the standard synthetic aperture (and other techniques) and shows the requirements for using this technique for pitch angle measurement on a future system.

5.5.1 Overview

Intensity interferometry is the science of obtaining an image from a phased array using intensity information alone. This idea dates back to Hanbury Brown and Twiss experiments [63, 64]. Standard interferometry or synthetic aperture (phased array) imaging is based on measuring the Fourier transform of the image whereby antenna voltage signal pairs give complex Fourier coefficients in Fourier space allowing a Fourier inversion to retrieve the image seen by the antenna. Intensity interferometry instead relies on the intensity of antenna pairs which gives the magnitude of the Fourier coefficient which cannot be used alone in a Fourier inversion (see the Van Cittert Zernike Equation 5.81) to retrieve the original image. A phase component must be multiplied into the magnitude in order to give a complex Fourier coefficient which can then be used for a Fourier inversion.

It has been shown that Fourier phase information can be retrieved from the Fourier magnitude allowing a image reconstruction. Over the decades different phase retrieval methods have been used and is a field of scientific research in it's own right. There is much literature for intensity interferometry and phase retrieval which can be confusing, but I will endeavour to provide a better understanding by describing intensity interferometry from the ground up. It is expected that the reader would be familiar with standard phased array interferometry and the Van Cittert Zernike theorem [61], which essentially says that the average complex point wise multiplication between one antennas and the conjugate of another antenna measures the complex Fourier transform of the brightness (intensity) distribution of an extended spatially incoherent source (see Eq. 5.81).

5.5.2 Measuring intensity

5.5.2.1 Young's double slit experiment

To understand intensity interferometry it helps to understand Young's double slit experiment and from this a full understanding of the nature of coherence and intensity can emerge. In Young's double slit experiment an incoherent source is split between two small apertures creating two coherent sources and are projected onto an imaging plane. The intensity measured on the imaging plane in the far field (say on a piece of paper or detector) is the Fraunhofer diffraction pattern which is equal to the square of the Fourier magnitude of the image.

Two slits seperated by 0.5mm which are illuminated by 0.6 μm radiation will create an interference pattern of fringes seperated by 1.2mm on a screen 1m from the slits (see Fig. 5.22). As is well known, the intensity is the average of the square of the electric field. In synthetic aperture (phased array) imaging using Van Cittert Zernike we consider complex disturbances, however when using only intensity (such as for intensity interferometry) we need only the real or imaginary signal squared. It is important to note that intensity is phase insensitive in that we have the same intensity from the real and the imaginary (from the hilbert transform) component of the detector signal.

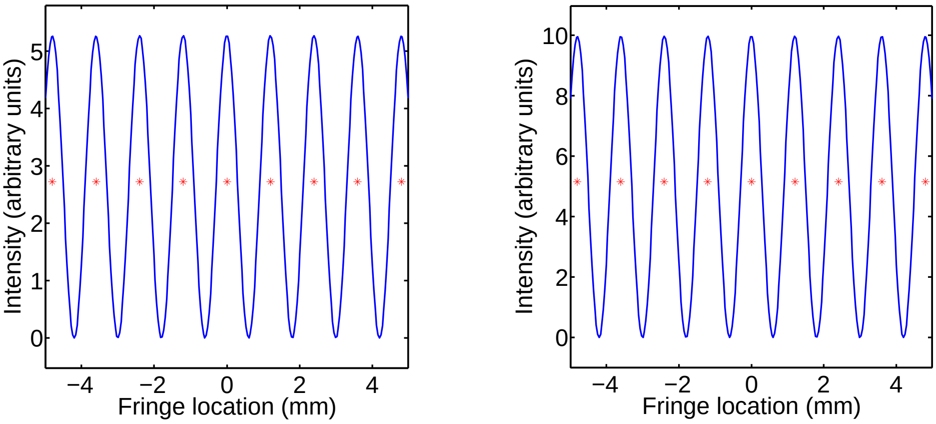

FIGURE 5.22: Left to right: i) real signal squared, ii) imaginary signal squared. The simulated emmision source is 0.6μm with a slit seperation of 0.5mm. The fringes are viewed at a distance of 1m giving a fringe seperation of 1.2mm (indicated by red stars).

The intensity measured at each point on the detector is [61]:

$$I = \langle (E_1 + E_2) \cdot (E_1 + E_2) \rangle = \langle E_1^2 \rangle + \langle E_2^2 \rangle + J_{12} \tag{5.80}$$

Where J_{12} is the mutual intensity or inteference term and defined by $J_{12} = 2\langle E_1 \cdot E_2 \rangle$. The diffraction pattern sinusoidally modulates due to the phase difference $cos\ \delta = \langle E_1 \cdot E_2 / |E_1||E_2| \rangle$. Two incoherent sources would not interfere and no diffraction pattern would be imaged which is the reason Young used a single slit before the double slit to create the two coherent sources.

5.5.2.2 Square law detectors

To measure intensity we need to measure the power of the incoming signal. This means we are measuring a signal which is proportional to the square of the electric field of the incoming radiation. To do this a square law detector is used. When the electric field is incident on a conductor (antenna) a voltage is produced which is proportional to the amplitude of the electric field. This voltage can then be directly digitised (amplitude/-voltage detector) or passed onto a diode. A diode can operate where the output voltage is proportional to the square of the incoming voltage, thus measuring the intensity of the incoming signal. Diodes are commonly used to measure intensity from RF to optical frequencies. It is important to take care that the input voltage is in the range of the square law operation of the diode. Another way of saying square law detector is non-linear detector. The exception to this is when a diode is used as a mixer where the output of the diode can be made to be proportional to the amplitude of an input signal.

5.5.2.3 Mixers

A mixer is essentially a diode (square law detector) rectifier with an isolating transformer that squares the sum of a high power LO and input signal. The squared signal will give a signal at twice the LO frequency and around DC. When mixing down the higher frequency is filtered out, and the offset voltage (absolute DC) signal blocked by the transformer. The bandwidth above DC is allowed through and is now our mixed down (baseband) signal. The output of the mixer is proportional to the amplitude of the input signal because squaring a sine wave (LO) summed with a lower amplitude signal results in this mathematically. If we wish to measure intensity the signal from the mixer has to be squared to be proportional to intensity.

5.5.3 Simulating intensity

5.5.3.1 Staying within the data bandwidth

To simulate a signal representative of reality the following must hold true: Any operation that we perform on a signal (or array of data representing a real signal) must after the operation be within the bandwidth (or Nyquist frequency) of the data. This is an easy mistake to make, for example when squaring a voltage signal it will be proportional to power, but it's not a signal representative of reality. If squaring the signal the maximum frequency components must be half the Nyquist (or one quarter of the sample frequency) so that when the signal is squared the frequency components will be up to the Nyquist frequency and thus within the data bandwidth. Such a signal is suitable for doing intensity interferometry simulations.

5.5.3.2 The Hanbury Brown Twiss experiment

The Hanbury Brown Twiss (HBT) experiment [64] showed that light incident on two spatially seperate photodetectors is partially correlated. This was a surprising result because correlation (or coherence) between light beams was traditionally measured using interferometry, where the coherence would be measured after interfering light beams.

How is it that light which has very high frequency fluctuations can have correlated fluctuations at the much lower detection frequency? One explanation is that the light incident on a diode such as that used for imaging stars demodulates or beats with itself on a diode resulting in low frequency fluctuations. Such beat signals are also seen on a photo diode when looking at a multi-mode laser where the modes are separated by some MHz or GHz resulting in a signal at 0 Hz plus the mode seperation frequency. This can be clearly explained and simulated by the square law nature of the diode detector. Consider incident broadband radiation on the diode, which is first narrow band filtered (such as via an optical filter), the squaring will result in signal at DC and twice the light frequency which will be outside the bandwidth of the diode and naturally filtered out leaving a signal around DC which is related to the light fluctuations incident on the diode. In simulations the filter is chosen such that the remaining signal is below one quarter of the sampling frequency, thus staying within the data bandwidth (see Section 5.5.3.1) when squaring. The steps are shown in Fig. 5.23. The resulting simulated signal is equivalent to one which would be viewed on a diode (intensity/square law) detector and can be used for doing intensity correlations to obtain the Fourier magnitude of an image (see Section 5.5.5).

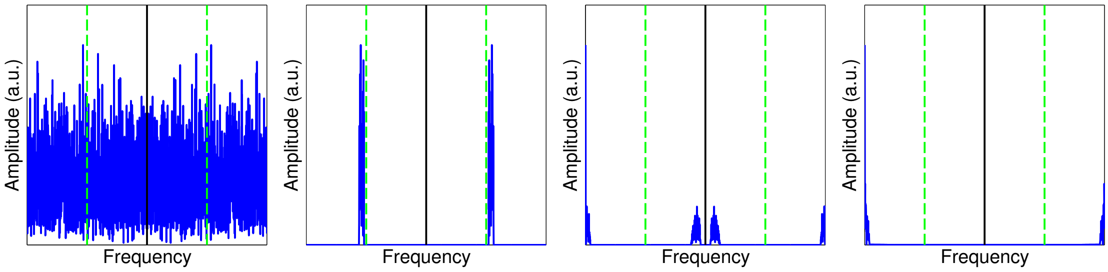

FIGURE 5.23: Left to right the Fourier transform of: i) raw broadband voltage signal, ii) narrow band filtered, iii) squared, iv) low pass filtered. The solid black line is half of the sample frequency and the dashed green line is quarter of the sample frequency.

5.5.4 Optical Downconversion

Optical downconversion is mentioned here since details of the HBT experiment and obtaining the Fourier magnitude have been discussed. Optical intensity interferometry assumes the light from a star is passed through a narrow band filter and then incident on a bandpass filter. The phase information is lost on the square law detection of the diode since the power of the spectrum is approximately constant. **A very important observation** is the possibility to preserve the phase information and perform optical downconversion and obtain I and Q information which allows in theory the construction of a different type of optical interferometer. This is achieved by doing the following: i) Light from a star at each antenna is narrow band filtered and split via two paths onto two different (I and Q) photo diodes. A narrow line width (~kHz or smaller bandwidth) single mode laser signal is distributed to each antenna and shone into the detector (acting as an LO). The power of the laser should be higher (~100 times) than the signal background. The signal from the diode should be DC-blocked and low-noise amplified and digitised. A low pass anti-alias digitiser filter is assumed. The diode essentially acts as a mixer downconverting the signal. Since the light is split via two different (approximately equal) paths there should be a different phase delay between the I and Q signal. Equation 5.74 allows a good quadrature signal to be obtained even if the path delay does not introduce a perfect 90 degree shift, but as long as it is greater than 10 degrees. Now side band separation can be performed to obtain the true signal and standard Van Cittert Zernike based synthetic aperture interferometry can be used. Of course a calibration is needed with a calibration star to define a phase relationship between each antenna. A full comparison of this method is compared with Van Cittert Zernike synthetic aperture inversion and intensity interferometry method is provided later (See Fig. 5.33).

5.5.5 Fourier magnitude from intensity

From the Van Cittert Zernike theorem [61, 65, 66] we know the complex Fourier coefficient (or complex degree of coherence):

$$\Gamma_{12} = \frac{\langle V_1 \cdot V_2^* \rangle}{\sqrt{I_1 \, I_2}} \tag{5.81}$$

Image reconstruction using Eq. 5.81 is referred to as synthetic aperture imaging, which is a method of phased array imaging. It can be shown that the Fourier magnitude $|\Gamma_{12}|$ can be given by intensity fluctuation correlations [67, 68]:

$$|\Gamma_{12}|^2 = \frac{\langle \Delta I_1 \cdot \Delta I_2 \rangle}{\langle I_1 \rangle \langle I_2 \rangle} \tag{5.82}$$

5.5.6 Fourier phase retrieval from the Fourier magnitude

Intensity interferometry has been shown to measure the Fourier magnitude of the source, but this is not enough information to reconstruct our original image. We need phase information which essentially allows us to obtain the complex Fourier coefficients of the source allowing a Fourier inversion to recover the image.

It is challenging to retrieve phase information from intensity measurements and there have been many different methods [69]. Recovery using triple correlations has been described by Gamo [70] and put into practice by [71, 72]. Methods have also worked using bispectra [73]. Each of these cases has their advantages and disadvantages. This chapter will focus on the Holmes-Cauchy-Riemann (HCR) method which is an analytical solution to the problem of phase retrieval.

5.5.7 Holmes-Cauchy-Riemann phase recovery

5.5.7.1 Theory

The thesis by Nuñez [74] and Holmes' papers [75, 76] are an excellent reference on the HCR theory which is shown here for completeness. Let us assume that the Fourier magnitude (R) can be represented by a complex number which is dependant upon another complex number (z). $I(z) = R(z)e^{i\Phi(z)}$ where $z = \xi + i\psi$. Here we are assuming that the Fourier magnitude (R) can be by a complex number. Here $I(z)$ is not intensity. ξ and ψ can be considered equivalent to variables in the image plane x and y. These are used interchangably where ξ and ψ are commonly used in astronomy.

The Cauchy-Riemann (CR) equations are can be written:

$$\frac{\partial \Phi}{\partial \psi} = \frac{\partial \ln R}{\partial \xi} = \frac{\partial s}{\partial \xi} \tag{5.83}$$

$$\frac{\partial \Phi}{\partial \xi} = -\frac{\partial \ln R}{\partial \psi} = -\frac{\partial s}{\partial \psi} \tag{5.84}$$

s is defined as the log magnitude. The CR equations show that if the phase is modelled as a complex variable, which changes spatially over the image with ξ and ψ (or x and y) then the derivitave of the log-magnitude is related to the derivitave of the phase. We can rewrite the derivatives along each axis:

$$\Delta s_{\xi} = \frac{\partial s}{\partial \xi}\Delta\xi = \frac{\partial \Phi}{\partial \psi}\Delta\xi \tag{5.85}$$

$$\Delta s_{\psi} = \frac{\partial s}{\partial \psi}\Delta\psi = -\frac{\partial \Phi}{\partial \xi}\Delta\psi \tag{5.86}$$

Since $|z| = 1$ we measure the log magnitude on the unit circle in complex space (ξ, ψ). In reality when we take the spatial derivative of the log magnitude of a real image, we measure the differences parallel to the unit circle $\Delta s_{||} = \Delta s_{\xi} + \Delta s_{\psi}$:

$$\Delta s_{||} = \frac{\partial s}{\partial \xi}\Delta\xi + \frac{\partial s}{\partial \psi}\Delta\psi \tag{5.87}$$

$$= \frac{\partial \Phi}{\partial \psi}\Delta\xi - \frac{\partial \Phi}{\partial \xi}\Delta\psi \tag{5.88}$$

$$= \Delta\Phi_{\perp} \tag{5.89}$$

This proves that the log magnitude differences are equal to the phase differences perpendicular to the unit circle. However, we need the phase differences parallel to the unit circle $\Delta\Phi_{||}$. The integral of the phase differences gives Φ (Fourier phase) which combined with R (Fourier magnitude) is the complex Fourier coefficent of the image. In order to obtain $\Delta\Phi_{||}$ what the HCR theory shows is that it is possible to show that the general solution of the phase can be shown to reduce to an equation of $\Delta\Phi_{\perp}$ whose orthogonal coefficients can be substituted back into the general solution to obtain the phase Φ. Since $\Delta s_{\|} = \Delta\Phi_{\perp}$ we are saying that the derivitive of the log Fourier magnitude contains the coefficients of the general solution to the phase.

The proof that the general solution of phase can be written in terms of $\Delta\Phi_{\perp}$ follows. Taking the second derivative of the CR equations (Eqs. 5.83) we see that Φ is a solution of the Laplace equation:

$$\frac{\partial^2\Phi}{\partial\xi^2} + \frac{\partial^2\Phi}{\partial\psi^2} = 0 \tag{5.90}$$

The general solution of Φ in polar coordinates (ρ, ϕ):

$$\Phi(\rho, \phi) = a_0 + b_0\phi + \sum_j \rho^j (a_j \cos j\phi + b_j \sin j\phi) \tag{5.91}$$

Where terms $(j < 0)$ have been ignored.

$$\Delta\Phi_{\perp}(\rho, \phi) = \sum_j \rho^j ((1 + \frac{\Delta\rho}{\rho})^j - 1)(a_j \cos j\phi + b_j \sin j\phi) \tag{5.92}$$

$\Delta_\phi = |\delta\xi + i\delta\psi|$ and $\Delta_\rho = |\delta\xi + i\delta\psi|$ implying $\Delta_\phi = \Delta_\rho$. A unit circle implies $\rho = 1$ which reduces to:

$$\Delta\Phi_{\perp}(\phi) = \sum_j j\Delta\phi(a_j \cos j\phi + b_j \sin j\phi) \tag{5.93}$$

The coefficients a_j and b_j can be found since the equation is an orthogonal basis therefore Fourier integration can be used to obtain the coefficients.

$$a_j = \frac{1}{2\pi j}\int_0^{2\pi} \frac{d\Phi_{\perp}}{d\phi} \cos j\phi d\phi \tag{5.94}$$

$$b_j = \frac{1}{2\pi j}\int_0^{2\pi} \frac{d\Phi_{\perp}}{d\phi} \sin j\phi d\phi \tag{5.95}$$

In summary HCR theory has shown that antenna pair intensity fluctuation correlations give the Fourier magnitude $R = |\Gamma_{12}|$. Where the log magnitude is denoted by $ln\ R = s_{\|}$. The differential of $s_{\|}$ (along a strip) gives the perpendicular phase differences $\Delta\Phi_{\perp}$.

These can be Fourier integrated to give a set of coefficients for the general solution of the phase Φ, thus retrieving the phase from intensity information.

5.5.7.2 Reconstruction 1-D

A 1-D reconstruction (see Fig. 5.24) is performed to demonstrate the possibility of doing an image reconstruction solely from Fourier magnitude information. This reconstruction has been performed using a fully sampled Fourier space. Fully sampled means the phase reconstruction is performed on the magnitude of the Fourier transform of the image and gives a best case reconstruction. The Fourier space of 1024 samples produces an image which is reasonably defined over 60 points. This highlights a fundamental limitation of HCR reconstruction: a much larger number (compared to synthetic aperture reconstruction) of baselines (and therefore antennas) are needed for a good reconstruction. The image reconstruction is very good despite the reconstructed phase not matching the original phase perfectly. In other reconstructions the phase can match perfectly, particularly when the phase changes more slowly.

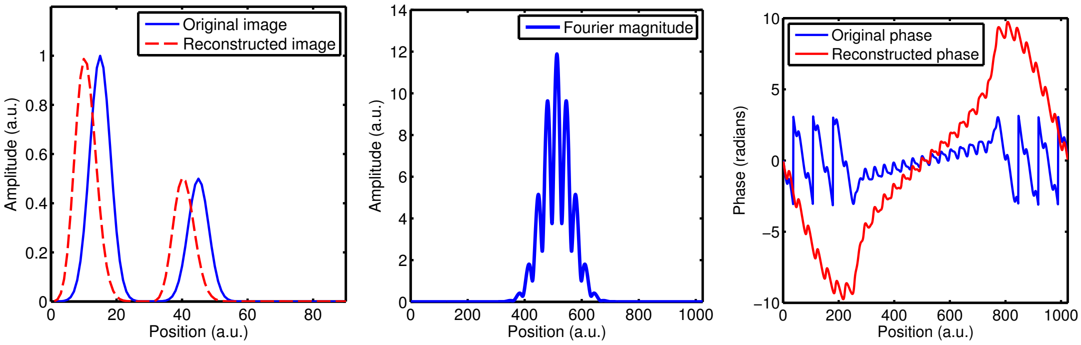

FIGURE 5.24: Left to right: i) Pristine image (blue) with reconstructed image (red), ii) Fourier magnitude, iii) Pristine phase (blue) with reconstructed phase (red).

5.5.7.3 Reconstruction 2-D

The HCR theory fully described obtaining the phase using the log of the Fourier magnitude. To extend the method to 2-D we do a 1-D reconstruction along slice of the Fourier magnitude, and then take an orthogonal slice and set the relative phases between slices using this orthogonal slice. This creates the 2-D phase which can be used to reconstruct the image. A 2-D reconstruction is performed on a fully sampled Fourier space for a double source (see Fig. 5.25) and triple source (see Fig. 5.26). These images show the best case reconstruction for two different images.

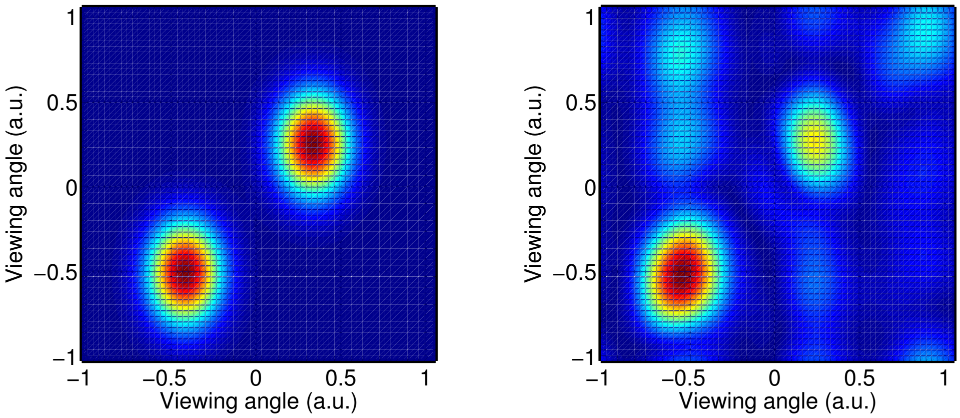

FIGURE 5.25: A two source pristine (left) with a (best case) HCR reconstruction (right). The reconstruction is artifical assuming a fully sampled Fourier magnitude of the image. It represents a best case reconstruction and not necessarily representative of what can be achieved with an antenna array. These results are shown later in this thesis.

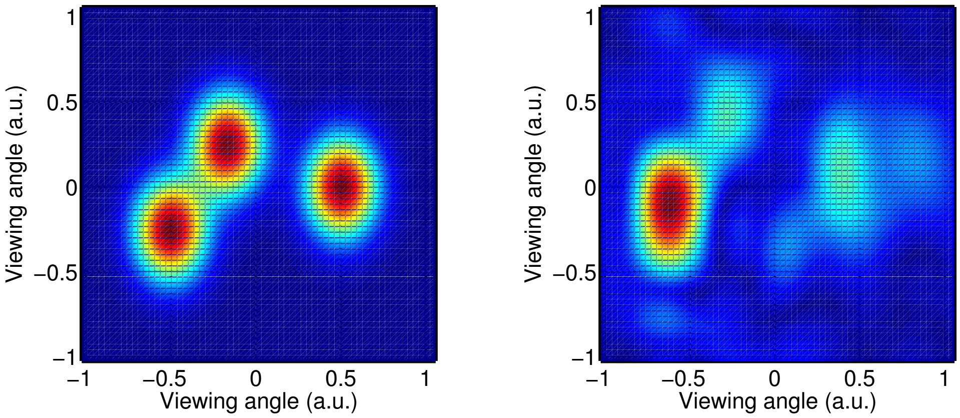

FIGURE 5.26: A three source pristine (left) with a (best case) HCR reconstruction (right). The reconstruction is artifical assuming a fully sampled Fourier magnitude of the image as in the two source image shown above. Clearly only one source is reconstructed well and the two other sources only faintly. A full investigation into which different images the HCR method is good at reconstructing is not given. However it is noted that two bright source images are well reconstructed, but three bright source images are only marginally reconstructed.

However for a real system implementing intensity interferometry the Fourier magnitude will be undersampled due to the limited number of antennas. A more realistic simulation of an 64 antenna array (see Fig. 5.27) imaging a binary star (0.6μm visible light) is shown (see Fig. 5.28) with the expected HCR reconstruction (see Fig. 5.29). The signal received by each antenna is time lagged (by performing a $\partial\phi/\partial\omega$ shift in Fourier space) according to its physical position from the source. Increased Fourier coverage due to earths rotation is not included which may significantly improve the reconstruction. Similar results are achieved by Jensen [77], Daniel [67] and Nunez [74]. The key result is that it demonstrates that HCR reconstruction can occur at the same baselines as would be used for the synthetic aperture imaging. This result, along with the phase insensitivity of the measurement (see Section 5.5.2) means that in astronomy intensity interferometry can utilise baselines up to the diameter of the earth hugely increasing angular resolution over standard phase array interferometers where this is not possible. These are not new results but are shown primarily to demonstrate the developed tools for these reconstructions that are then used to compare different methods and simulate applicability for the SAMI EBW system.

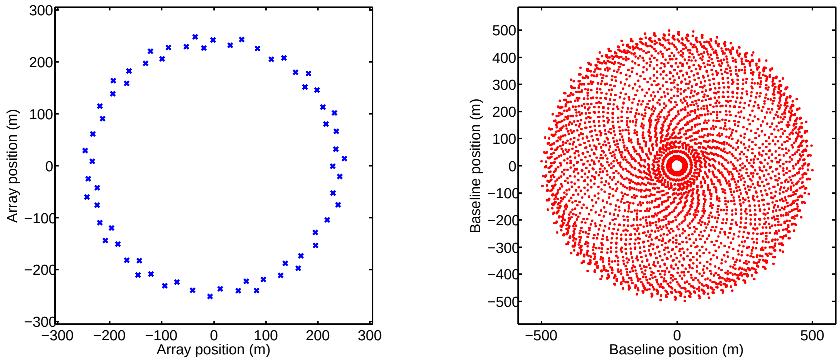

Figure 5.27: Left to right: i) Antenna array, ii) Antenna baselines. The antenna array is chosen to give as uniform as possible Fourier space coverage as can be seen in the baselines. A uniform Fourier space coverage is useful for phase retrieval since the Fourier magnitude can easily be interpolated onto a grid (see 5.29).

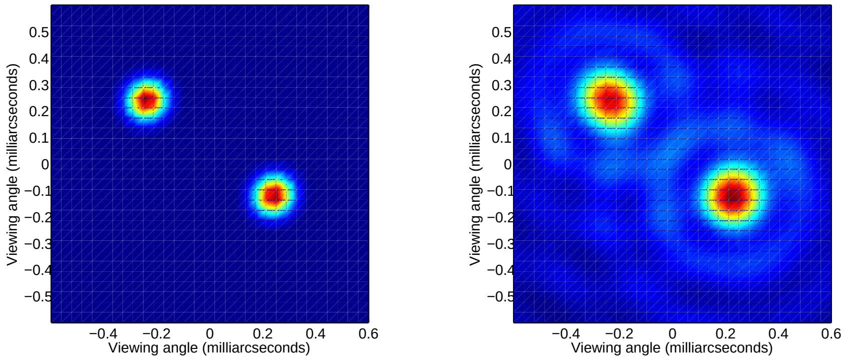

Figure 5.28: Left to right: i) The pristine image, ii) The synthetic aperture (using VCZ theorem) reconstructed image. The slight fringing seen in the reconstructed image is due to the large number (for synthetic aperture imaging) of antennas used.

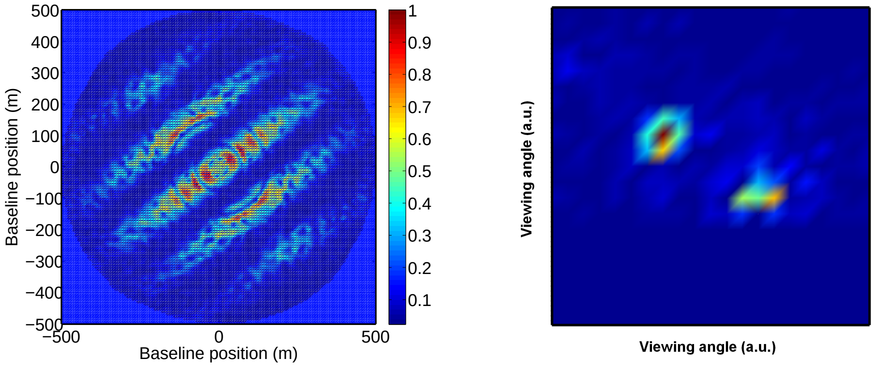

Figure 5.29: Left to right: i) The sampled Fourier magnitude received at the baselines. The apparent rings are a function of the circular nature of the selected antenna array, ii) The CR reconstruction of the two source image. The axes are viewing angle in arbitrary units. The reconstruction is poor due to the undersampled Fourier magnitude caused by the small number (64) of antennas.

5.5.8 Reconstruction method comparison

It is useful to do an image reconstruction (see Fig. 5.30) comparison between different methods: synthetic aperture imaging (see Fig. 5.31), synthetic aperture imaging using intensity information (phase retrieval is not used in the reconstruction, see Fig. 5.32), and optical downconversion (see Fig. 5.33) and Section 5.5.4). The image seen using intensity information clearly does not result in a good reconstruction and phase retrieval should be used to attempt a better image reconstruction. However a good image is unlikely since there Fourier space is severly undersampled to attempt phase retrieval. The optical downconversion method preserves the phase despite the signal being squared. This is because before squaring a higher amplitude LO signal is added at the detector, essentially forcing the detector to act as a mixer.

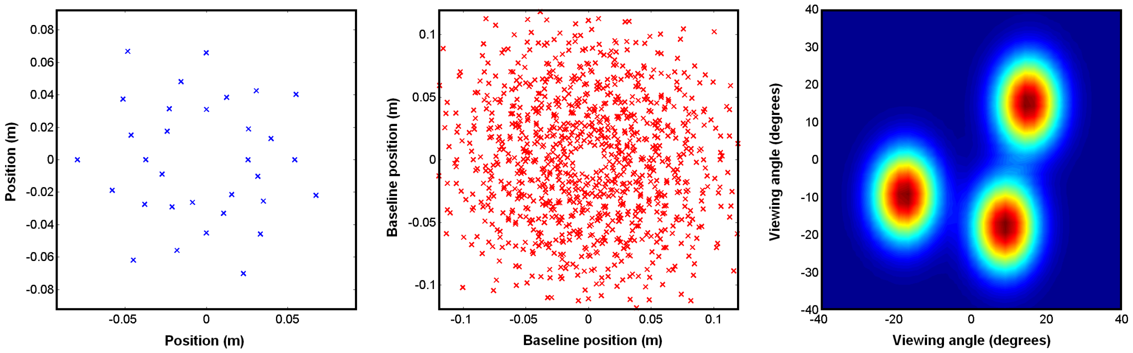

FIGURE 5.30: Left to right: i) Array, ii) Baselines, iii) Pristine image.

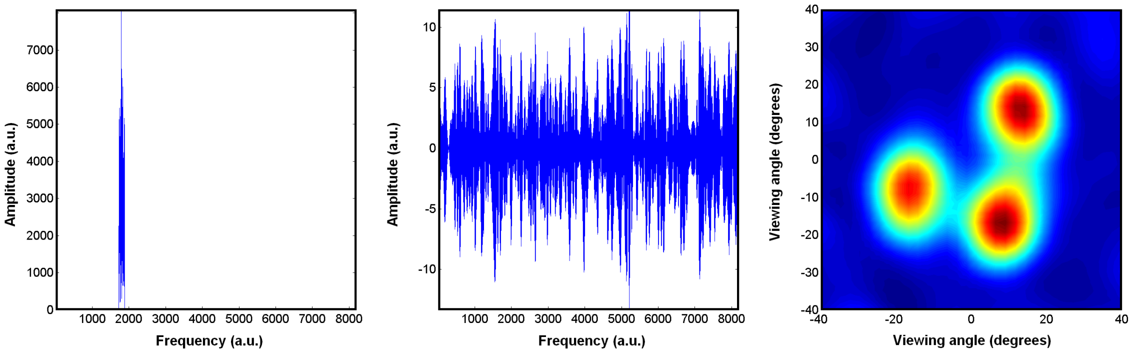

FIGURE 5.31: Left to right: i) FFT of an antenna signal which is narrow band filtered, ii) Real antenna signal, iii) Reconstructed image using the Van Cittert Zernike (synthetic aperture) reconstruction.

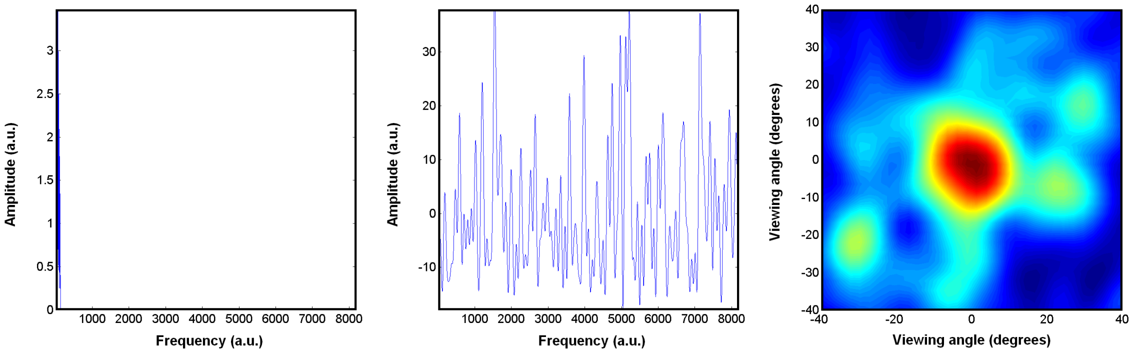

FIGURE 5.32: Left to right: i) FFT of an antenna signal which was narrow band filtered and then squared, ii) Real antenna signal, iii) A view of the attempted reconstructed image using VCZ. There is no phase information since the signal did not have a dominant pure sine wave before squaring to preserve phase information. This image represents the Fourier magnitude.

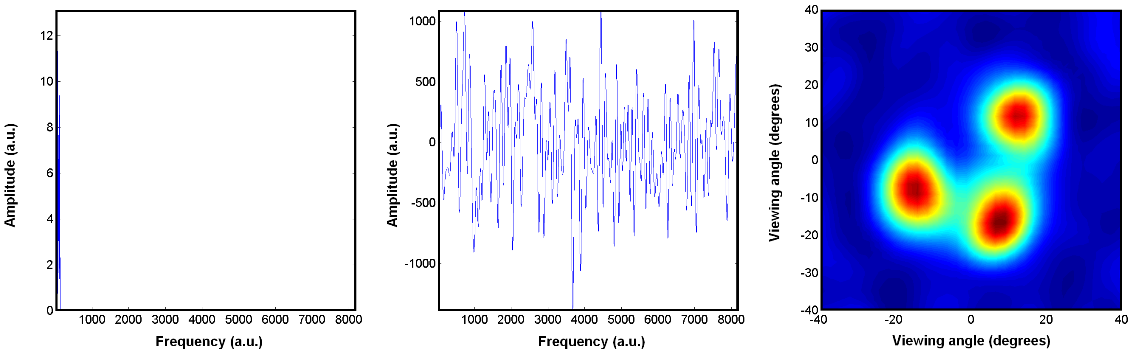

FIGURE 5.33: Left to right: i) FFT of an antenna signal which viewed the incoherent source but in addition a pure sine wave (of higher power than the background signal) which was placed at one side of the narrow band filter to prevent the need for side band separation. The signal was then squared and DC removed/blocked, ii) Real antenna signal, iii) Reconstructed image which shows the phase preserved. This method can be used for optical downconversion on the photo diode (see Section 5.5.4).

5.5.9 Intensity interferometry on SAMI

5.5.9.1 Summary of current findings

It has been shown that for phase retrieval a large number of antennas is needed. The simulation in Figure 5.29 resulted in a poor reconstruction using 64 antennas and so could be considered a lower limit. The HCR method cannot be applied on the current SAMI system with 8 antennas. However the next section shows that since we know something about the emission, we can avoid phase retrieval altogether and still make a useful measurement of the pitch angle using intensity information alone with a small number of antennas.

5.5.9.2 An alternative method for measuring pitch angle with the EBW SAMI system

The primary goal of the EBW SAMI systems is to measure pitch angle. Since the EBW emission is from two sources (mode conversion windows) this will create a diffraction pattern (Fourier magnitude) where the angle of the fringes are equal to the pitch angle (if x-baseline is swapped). The diffraction pattern is imaged by the intensity correlations between antennas as described by intensity interferometry theory. We do not need to do phase reconstruction since we are assuming the image is two sources and thus creates a well known diffraction pattern.

On the EBW system we have 16 channels. If we just digitise the real signal we can have 16 real antenna signals, giving $\sim 4\times$ Fourier coverage. The signal IF signal from the mixer needs to be passed to a diode and then DC blocked. This signal will represent the narrow band voltage signal squared and suitable for doing the intensity correlations. It is shown that 8 antennas is not enough (see Fig. 5.34 and Fig. 5.35) but that 16 antennas can be used (see Fig. 5.36, Fig. 5.37 and Fig. 5.38) to get the pitch angle. The optimum frequency appears to be around 10 GHz however the pitch angle should be obtainable at 20 GHz. Other frequencies are not simulated. A comparison with the expected synthetic aperture reconstruction is provided however the digitisation channels for synthetic aperture is doubled due to requirement of having an additional quadrature signal for every antenna.

In a harsh reactor environment it is reasonable to expect that achieving phase sensitivity will be more difficult. Using intensity information means a more phase insensitive detection is used and so is potentially a more reliable way to measure the pitch angle than using standard synthetic aperture imaging.

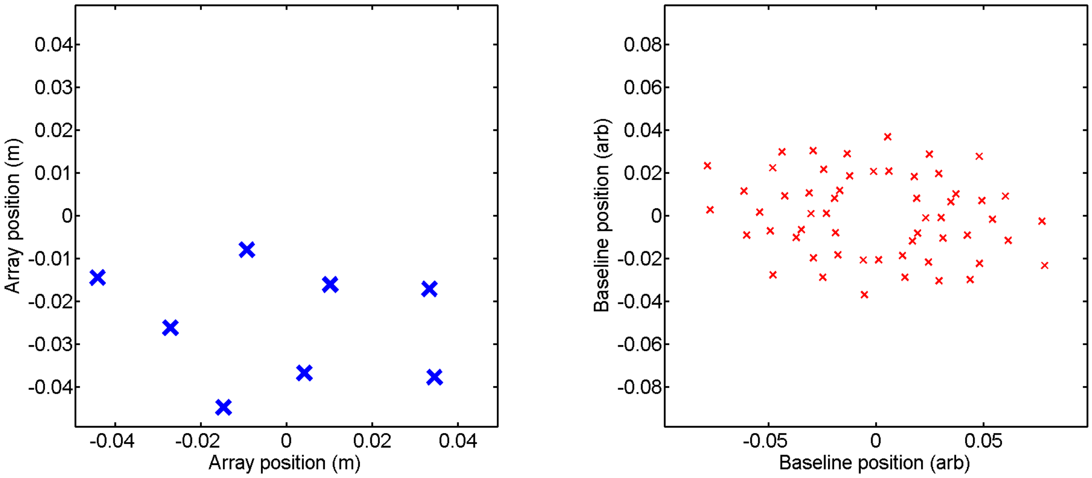

FIGURE 5.34: Left to right: i) Current (as of August 2013) EBW SAMI system array, ii) Baselines.

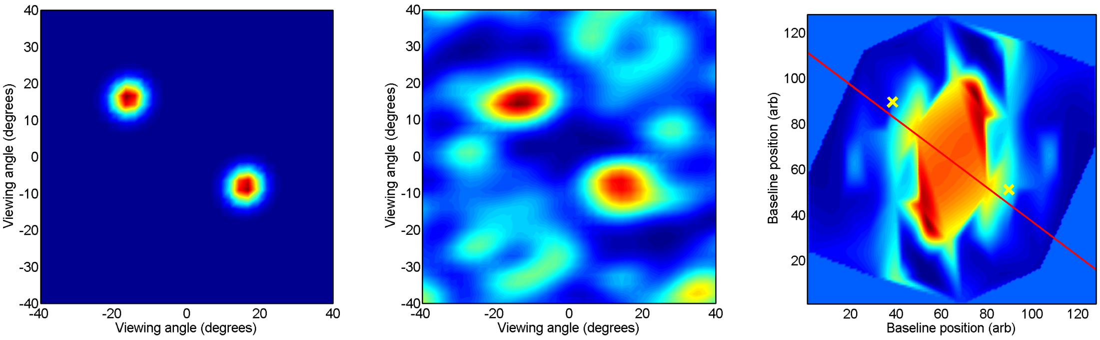

FIGURE 5.35: Left to right: i) Pristine, ii) Synthetic aperture reconstruction at 20 GHz with 8 antennas, iii) The sampled Fourier magnitude. The red line indicates the pitch angle.

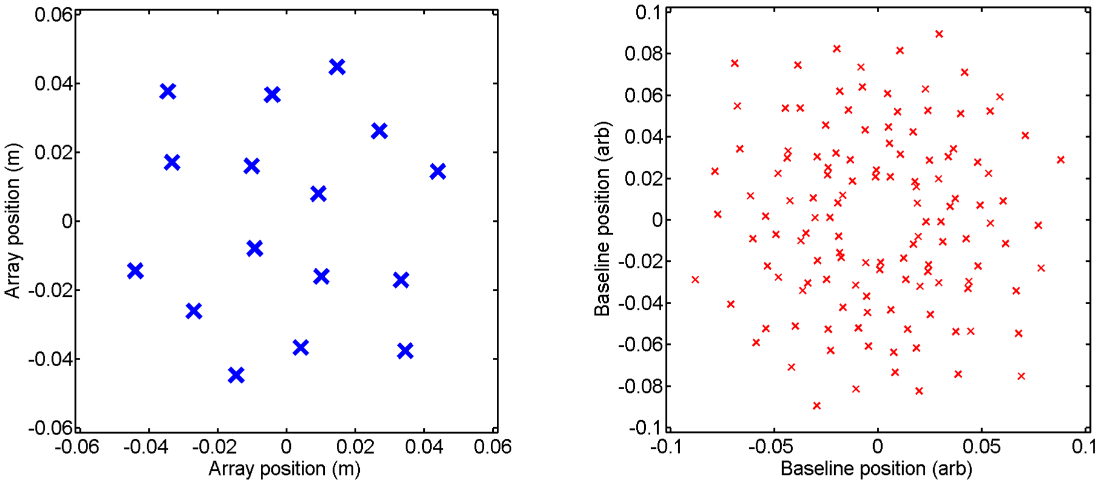

FIGURE 5.36: Left to right: i) Example 16 antenna array, ii) Baselines with larger ($\sim 4\times$) Fourier space coverage.

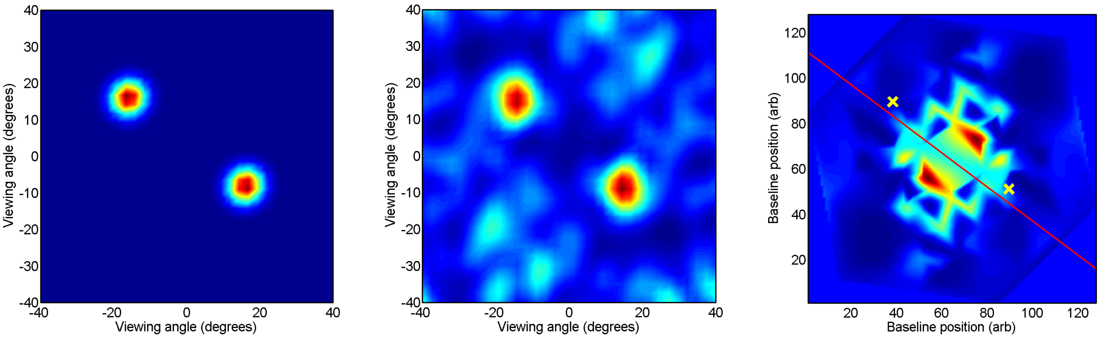

FIGURE 5.37: Left to right: i) Pristine, ii) Synthetic aperture reconstruction at 20 GHz with 16 antennas, iii) The sampled Fourier magnitude. The red line indicates the pitch angle.

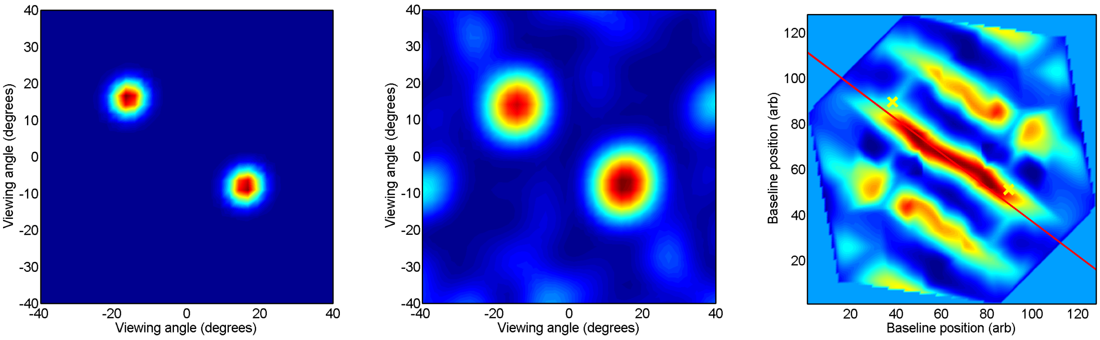

FIGURE 5.38: Left to right: i) Pristine, ii) Synthetic aperture reconstruction at 10 GHz with 16 antennas, iii) The sampled Fourier magnitude. The red line indicates the pitch angle.

5.6 Summary

EBW is interesting for spherical tokamaks which have overdense plasmas where traditional heating and current drive methods such as ECRH are not efficient. EBW is also important for reactors where conditions are harsh. LHCD requires contact with the plasma which is a problem for a reactor environment. The theory of EBW was presented which describes mode conversion windows which are imaged using synthetic aperture imaging by the EBW SAMI system. The high speed, high bandwidth capability of FPGAs has been used to good effect in the SAMI system which took advantage of some of the latest FPGA technology. Intensity intereferometry with HCR phase retrieval has been simulated and it has been shown that this imaging method probably requires at least 64 antennas. An alternative method is presented for imaging the pitch angle using intensity information and a small number (~ 16) of antennas assuming two seperate sources as predicted by EBW theory. This method is more phase insensitive than synthetic aperture imaging and so may be a more robust way of measuring the pitch angle, particularly in harsh reactor environments.

Chapter 6

Conclusion

FPGA technology is being used for advanced diagnostics in fusion. FPGA technology is progressing at a rapid pace with faster, larger devices combined with on board processing power leading to opportunities to develop ever more sophisticated diagnostics and real-time plasma control sensors and actuators. This thesis has discussed some of the recent advances of FPGAs and their application in a number of systems.

Embedded Linux is a very useful feature of FPGA devices and allows an expanded capability particularly for remote control and management. This utility has been recognised with the recent release of an FPGA called the ZYNQ, with an embedded dual-core ARM processor running a mainline Linux distribution. This massively opens up the amount of software an FPGA can interface and provides exciting opportunities for future systems, such as communications over WiFi networks. High level tools have been used to speed up the design of complex DSP algorithms, such as the implementation of a combined FIR bandpass and Hilbert transform filter for real-time single sideband signal generation.

The closed loop real-time control prototype for the ITER Thomson Scattering system has demonstrated the capability to combine multiple lasers onto a single beam-path for higher laser pulse repetition rate, on the order of 100 Hz with an RMS pointing stability well below 25 μrad. These results show that for ITER a high reliability beam combiner with good pointing stability is technically feasible.

The TAE system on MAST using FPGA based frequency sweeping signal generator for the TAE coil power supplies has allowed increased capabilities on the TAE antenna driving system and results show evidence of TAE resonance detection. This opens up an opportunity for further TAE experiments with the MAST Upgrade with the aim to develop a diagnostic that can report useful information about the plasma such as toroidal β and q-profile.

The EBW data acquisition system made use of advanced FPGA capabilities, such as the AXI bus to allow record high speed data streaming capabilities. This enabled the diagnostic to acquire in real-time 4 GB of data in 0.5 seconds. The EBW single sideband generator demonstrates the large bandwidth capability (over 250 MHz) of an FPGA with advanced digital signal processing to improve upon analogue microwave components. The EBW emission from an overdense spherical tokamak plasma forms two emission windows which is anagolous to imaging binary stars in astronomy. As part of an investigation into phase insensitive measurements, the intensity interferometry results showed that in principle 16 antennas can be used on the EBW SAMI system to detect the diffraction pattern from correlations of intensity fluctuations between antenna pairs, and that the well known diffraction pattern from two sources will give intereference fringes directly related to the pitch angle. Such a phase insensitive measurement could be a more robust way of making this measurement.

The learning curve for working with FPGA technology is quite steep and requires a different way of thinking to conventional programming. Even an expert programmer who knows multiple languages may take a good 6 months to get familiar with FPGAs and potentially a couple of years to achieve a high level of expertise. This is one of the big challenges in fusion since it requires fusion laboratories to invest in this technology. It is evident that currently this expertise is scarce and needs more attention in fusion. Working with CERN and other labs inside and outside of fusion research allows sharing of hardware to enable the fusion community to develop and maintain advanced FPGA systems more easily.

On MAST an FPGA system has been used by Tom O'Gorman to reduce the size of undesirable Neoclassical Tearing Modes (NTMs) which can result in plasma disruptions. These disruptions have been prevented by using a real-time feedback system to change the vertical position of the plasma. The changing vertical position forces a transition of the plasma from H-mode to L-mode and then back to H-mode [78]. This type of experimentation is important on overdense plasma devices such as MAST. Since although NTMs can be suppressed using ECCD [79, 80], ECCD cannot be used on MAST when the plasma is overdense and instead EBW current drive or vertical kicks may be needed.

Other systems include NBI beam notching for real-time feedback to control β_{toroidal} which will enable new ways of controlling experiments.

The future of FPGAs in plasma control for fusion may be enhanced by the inclusion of C to VHDL software (High Level Synthesis) in FPGA tools enabling the capability for advanced algorithms using floating point calculations to be more easily incorporated into FPGAs, providing potentially a huge benefit for higher frequency real-time control in plasma systems, such as real-time calculation of the last closed flux surface (LCFS) or other useful plasma calculations. In summary FPGAs are a very exciting technology and this thesis has barely scratched the surface of their applications on MAST. I hope that they are used to great benefit to help further fusion research and help us in our goal to build a fusion power plant.

Appendix A

Appendix A

A.1 Cauchy Riemann 1D MATLAB Code

I am grateful to Paul Nunez who supplied example C-Code to understand how CR can be implemented. Below is MATLAB code I have created for CR reconstruction. For 2-D reconstruction the algorithm is applied to each slice of the 2-D array and then a perpendicular slice is used to set the relative phases.

CR_Slice_1D.m

```
% Given the Fourier magnitude this returns the Cauchy Riemann
% reconstructed phase.

function [phase_dat] = CR_Slice_1D(mag_data)

  absI = mag_data;
  x    = [1:length(ds)];
  ds   = diff(log([absI; absI(1)]));
  dp   = 2*pi/length(x);

  fa = zeros(1,length(x)); fb = zeros(1,length(x));
  fma = fa; fmb = fb;
  intc = 0; ints = 0;

  % Integrate the radial differences to get the coefficients
  % for the general solution
  for j=1:length(x)-1
    intc = sum((ds.*cos(j*dp*[1:length(x)]’)));
```

```
    ints = sum((ds.*sin(j*dp*[1:length(x)]')));
    fa(j) = intc/pi; fb(j) = ints/pi;
  end

  for j=1:length(x)-1
    intc = sum((ds.*cos(-j*dp*[1:length(x)]')));
    ints = sum((ds.*sin(-j*dp*[1:length(x)]')));
    fma(j) = intc/pi; fmb(j) = ints/pi;
  end

  rp = zeros(1,length(x));

  % Reconstruct the general solution
  for j=1:length(x)-1

    div = (j*dp);
    tmp_rp = ((fa(j).*cos(j*dp*[1:length(x)])) + ...
                    (fb(j).*sin(j*dp*[1:length(x)])))/div;
    rp = rp + tmp_rp;

  end

  rp = dp*rp;

  % piston = rp(1);
  % tilt = (rp(1)-rp(end))/length(x)
  % rp = rp - piston + [1:length(x)].*tilt;

  % Return the phase
  phase_dat = rp;

end
```

A.2 HLS Code

fir.h

```
#include <stdio.h>
#include <stdlib.h>
```

```
#include <hls_stream.h>

#define TAPS 21
#define RUN_LENGTH 100

void fir_hw(hls::stream<int> &input_val,
            hls::stream<int> &output_val);
```

fir.c

```
#include "fir.h"

void fir_hw(hls::stream<int> &input_val,
            hls::stream<int> &output_val)
{
    int i;
    static short shift_reg[TAPS] = {0};
    const short coeff[TAPS] = {6,0,-4,-3,5,6,-6,-13,7,44,64,
                               44,7,-13,-6,6,5,-3,-4,0,6};

    for (i=0; i < RUN_LENGTH; i++) {

#pragma AP PIPELINE II=1 rewind

        int sample;
        sample = input_val.read();

        // Shift register
        for (int j=0; j < TAPS-1; j++) {
            shift_reg[j] = shift_reg[j+1];
        }

        shift_reg[TAPS-1] = sample;

        // Filter operation
        int acc = 0;
        for (int k=0; k < TAPS; k++) {
            acc += shift_reg[k] * coeff[k];
        }
        output_val.write(acc);
```

```
        }
}
```

Appendix B

Appendix B

B.1 Laser beam combiner circuits

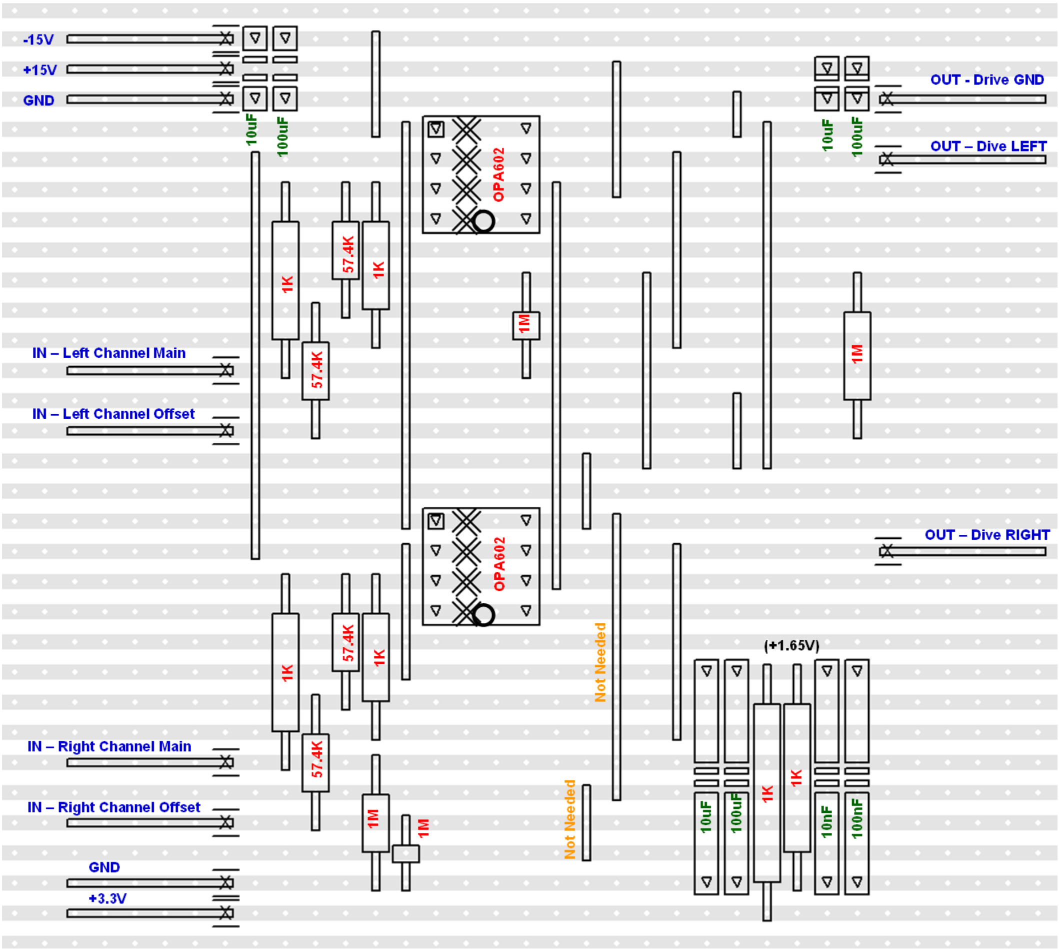

FIGURE B.1: Converts the main and offset signals from the FPGA (IN) into a differential drive signal that is sent to the scanning mirror.

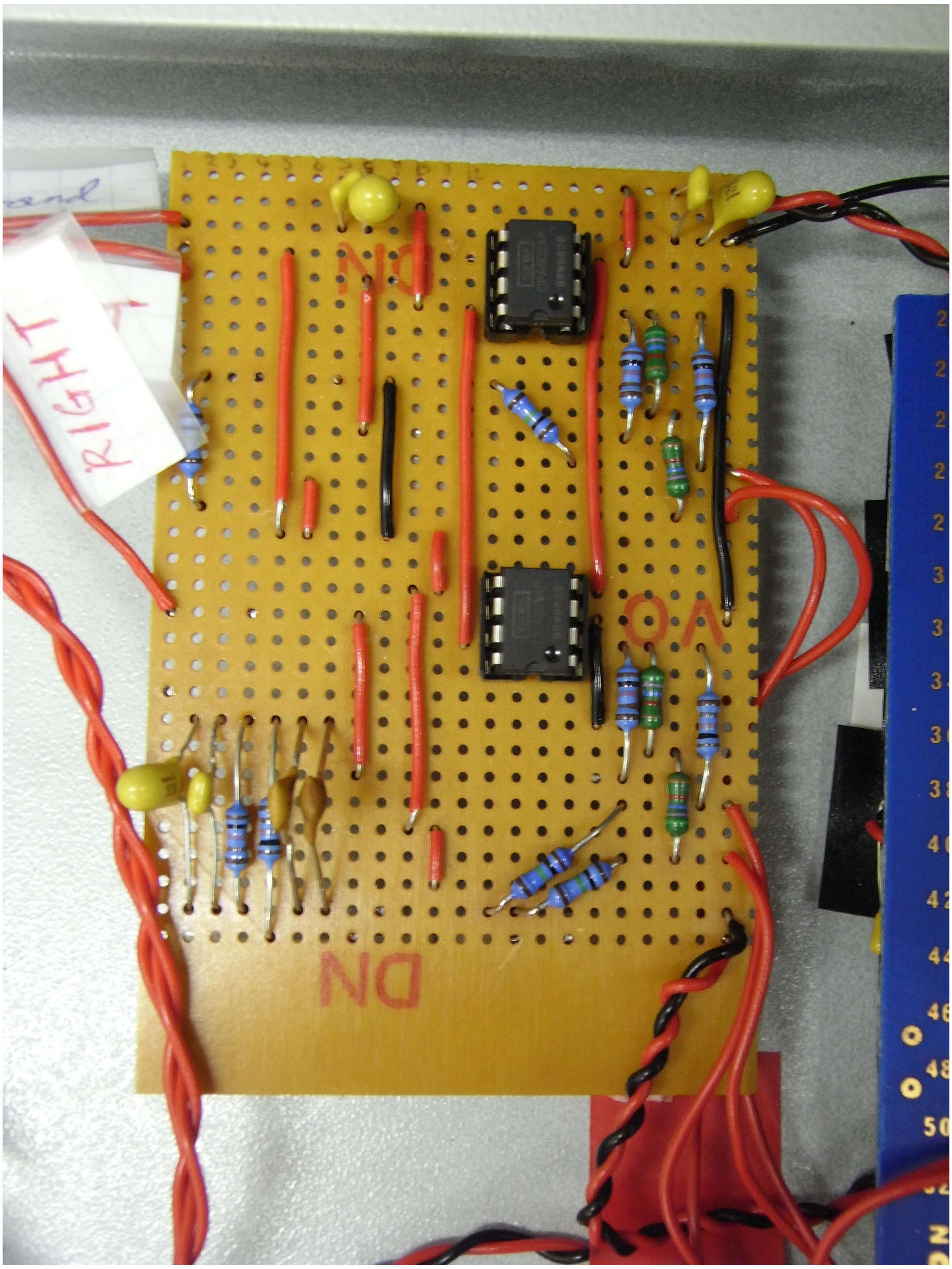

Figure B.2: A photo of Circuit A. See the schematic for more detail.

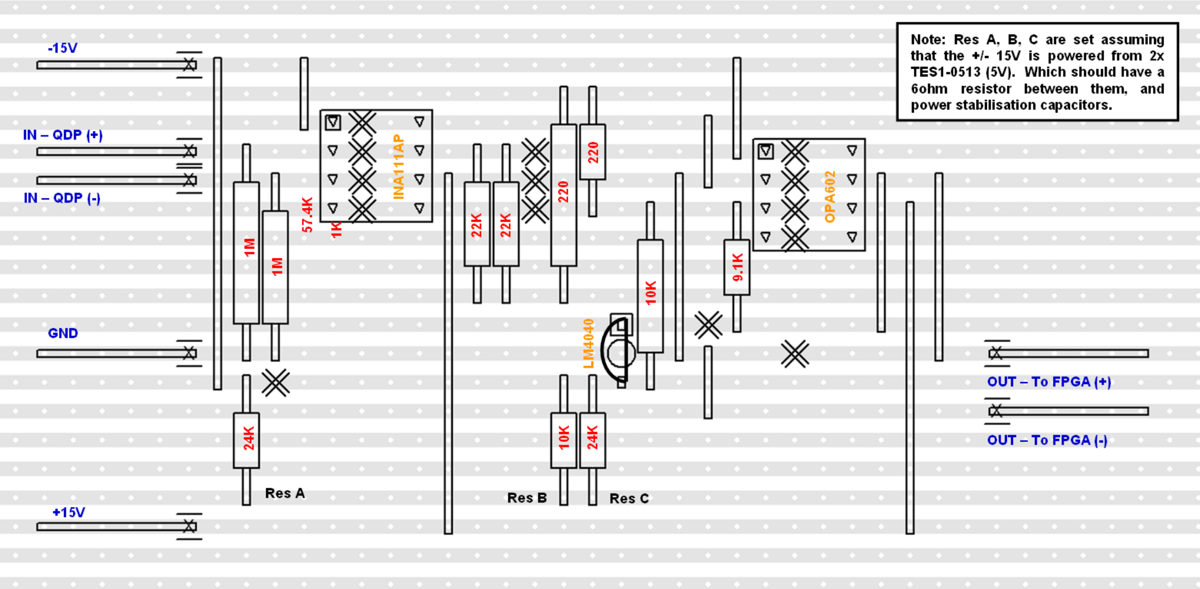

Note: Res A, B, C are set assuming that the +/- 15V is powered from 2x TES1-0513 (5V). Which should have a 6ohm resistor between them, and power stabilisation capacitors.

Figure B.3: Converts the ±2V signal from the QPD to 0-3.3V for the Pmod AD1 Card that is attached to the FPGA.

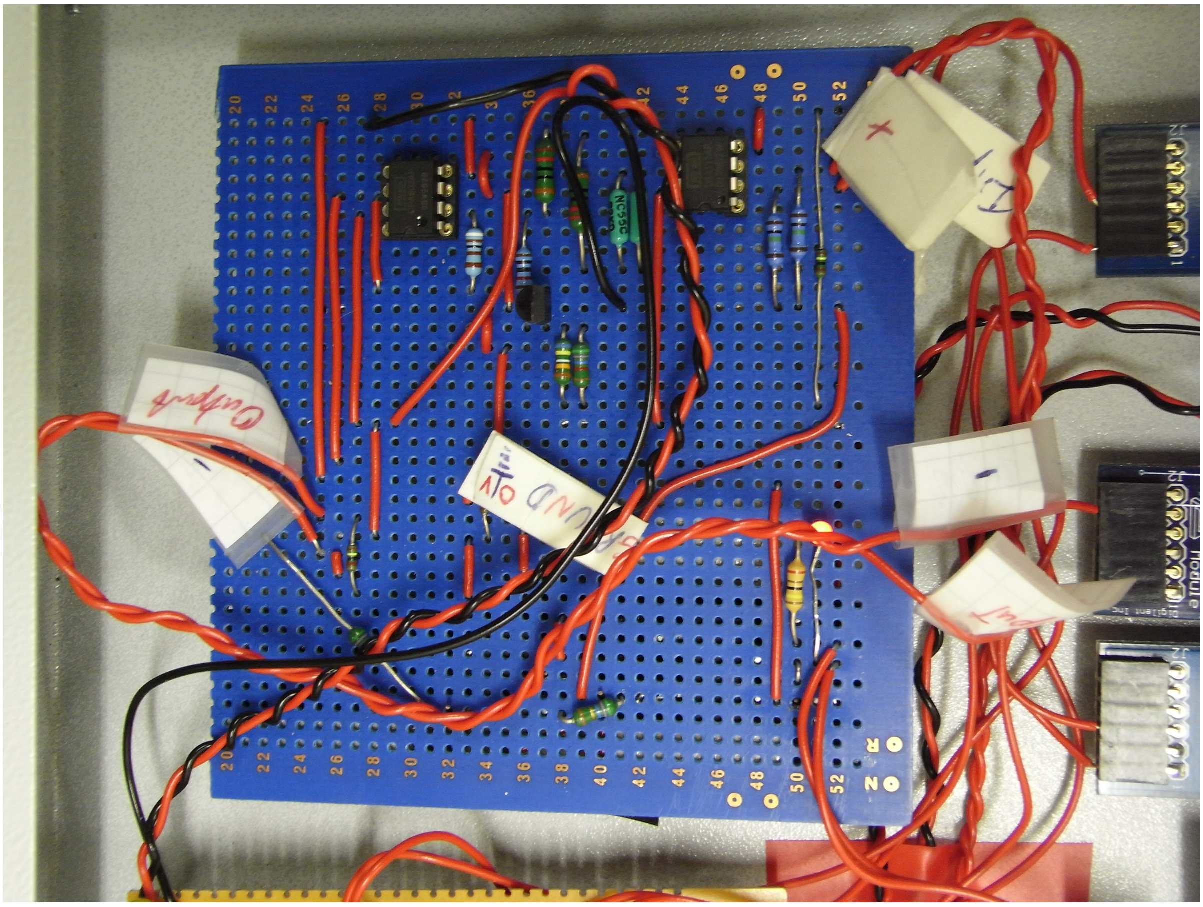

Figure B.4: A photo of Circuit B. See the schematic for more detail.

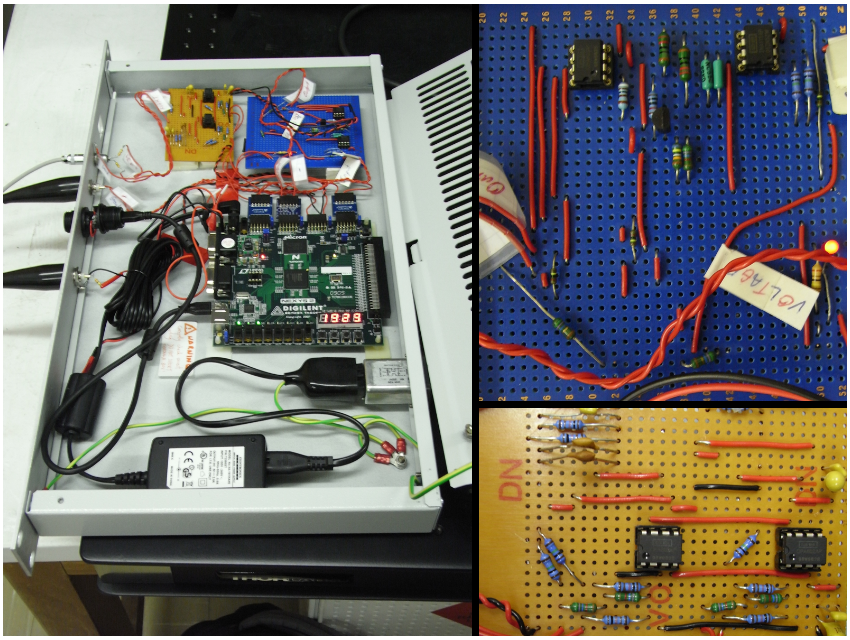

Figure B.5: Left: The fully assembled feedback control system containing the circuits used for analogue signal modification, Nexys2 FPGA and 5V power supply. Right top: Circuit B, for converting the ±2V QPD signal to 0-3.3V for input to the PMOD AD1 Board. Right bottom: Circuit A, for adding the main and offset waveforms to create the scanning mirror driver signal.

Appendix C

Appendix C

C.1 Publications

C.1.1 Primary publications

Huang et al. *FPGA-based embedded Linux technology in fusion: The MAST microwave imaging system*. IAEA Fus. Eng. Design (**2012**). [62].

Balboa, Huang et al. *Laser Beam Combiner for Thomson Scattering Core LIDAR*. Rev. Sci. Instruments. AIP. (**2010**). [24].

Svoboda, Huang et al. *Multi-mode Remote Participation on the GOLEM Tokamak*. Fusion Eng. and Design. Elsevier (**2011**). [81].

Huang et al. *Embedded Linux on FPGA Instruments for Control Interface and Remote Management*. ICALEPCS Proceedings (**2011**). [82].

Huang et al. *FPGA-based hardware instrumentation development on MAST*. ICALEPCS Proceedings (**2011**). [83].

C.1.2 Non-Journal

Huang et al. *Bottling a Star Using ARMs AXI Bus in an FPGA*. Xcell Journal: Issue 76 (**2011**).

C.1.3 Other Publications

T. O'Gorman, G. Naylor, K. J. Gibson, B. Huang et al. *A field programmable gate array unit for the diagnosis and control of neoclassical tearing modes on MAST*. AIP (**2012**). [78].

V. F. Shevchenko, R. G. L. Vann, S. J. Freethy, B. K. Huang. *Synthetic aperture microwave imaging with active probing for fusion plasma diagnostics*. Journal of Instrumentation. (**2012**). [84].

Bibliography

[1] G. Y. Fu and J. W. Van Dam. Excitation of the toroidicity induced shear alfvén eigenmode by fusion alpha particles in an ignited tokamak. *Physics of Plasmas, Phys. Fluids B*, 1:1984–1993, 1989.

[2] Stefaan Poedts and Elisabeth Schwartz. Computation of the ideal-mhd continuous spectrum in axisymmetric plasmas. *Journal of Computational Physics*, 105(1):165 – 168, 1993. ISSN 0021-9991. doi: 10.1006/jcph.1993.1061. URL `http://www.sciencedirect.com/science/article/pii/S0021999183710612`.

[3] V. F. Shevchenko. ECE measurements via B-X-O mode conversion: A proposal to diagnose the q profile in spherical tokamaks. *Plasma Physics Reports*, 26(12): 1000–1004, 2000.

[4] H Igami, H Tanaka, and T Maekawa. A survey of mode-conversion transparency windows between external electromagnetic waves and electron bernstein waves for various plasma slab boundaries. *Plasma Physics and Controlled Fusion*, 48(5):573, 2006. URL `http://stacks.iop.org/0741-3335/48/i=5/a=006`.

[5] A.C. Darke, J.R. Harbar, J.H. Hay, J.B. Hicks, J.W. Hill, J.S. McKenzie, A.W. Morris, M.P.S. Nightingale, T.N. Todd, G.M. Voss, and J.R. Watkins. MAST: A Mega Amp Spherical Tokamak. *Fusion Technology*, 1:799–802, 1994. Proceedings of the 18th Symposium on Fusion Techonology, Karlsruhe, Germany, 22-26 August 1994.

[6] R J Akers, J W Ahn, G Y Antar, L C Appel, D Applegate, C Brickley, C Bunting, P G Carolan, C D Challis, N J Conway, G F Counsell, R O Dendy, B Dudson, A R Field, A Kirk, B Lloyd, H F Meyer, A W Morris, A Patel, C M Roach, V Rohzansky, A Sykes, D Taylor, M R Tournianski, M Valovic, H R Wilson, K B Axon, R J Buttery, D Ciric, G Cunningham, J Dowling, M R Dunstan, S J Gee, M P Gryaznevich, P Helander, D L Keeling, P J Knight, F Lott, M J Loughlin, S J Manhood, R Martin, G J McArdle, M N Price, K Stammers, J Storrs, M J Walsh, the MAST, and NBI Team. Transport and confinement in the mast plasma.

Plasma Physics and Controlled Fusion, 45(12A):A175, 2003. URL http://stacks.iop.org/0741-3335/45/i=12A/a=013.

[7] J. Wesson and D.J. Campbell. *Tokamaks*. International series of monographs on physics. Clarendon Press, 2004. ISBN 9780198509226. URL http://books.google.com/books?id=iPlAwZI6HIYC.

[8] Xing Z. Li, Qing M. Wei, and Bin Liu. A new simple formula for fusion cross-sections of light nuclei. *Nuclear Fusion*, 48(12):125003, 2008. URL http://stacks.iop.org/0029-5515/48/i=12/a=125003.

[9] J. D. Huba. NRL plasma formulary. Naval Research Laboratory, Washington, D.C., 2009.

[10] R. Reichle, D. Guilhem, R. Mitteau, J.C. Vallet, C. Balorin, P. Bibet, M. Chantant, E. Delchambre, C. Desgrange, L. Ducobu, A. Ekedahl, F. Escourbiac, F. Faisse, A. Geraud, M. Goniche, M. Jouve, M. Lipa, G. Martin, P. Messina, D. Moulin, C. Pocheau, H. Roche, A. Saille, F. Saint-Laurent, J. Schlosser, E. Thomas, and E. Tsitrone. Status of power balance monitoring for long pulse operation at Tore Supra. *Nuclear Fusion*, 43(9):797, 2003. URL http://stacks.iop.org/0029-5515/43/i=9/a=301.

[11] P. Sichta, J. Dong, R. Marsala, G. Oliaro, and J. Wertenbaker. Developments to supplant CAMAC with industry standard technology at NSTX. *Fusion Engineering and Design*, 71:129–133, 2004.

[12] Mikyung Park, K.H. Kim, M.C. Kyum, and M. Kwon. Development of a prototype time synchronization system for KSTAR with a VME-bus system. *Fusion Engineering and Design*, 81(15-17):1817 – 1821, 2006. ISSN 0920-3796. doi: DOI:10.1016/j.fusengdes.2006.04.025. URL http://www.sciencedirect.com/science/article/B6V3C-4JW7WWR-1/2/de08cd9c532215136e96bdab754277b3. 5th IAEA TM on Control, Data Acquisition, and Remote Participation for Fusion Research - 5th IAEA TM.

[13] J. Liptac, R. Parker, V. Tang, Y. Peysson, and J. Decker. Hard x-ray diagnostic for lower hybrid experiments on Alcator C-Mod. *Review of Scientific Instruments*, 77(10):103504, 2006. doi: 10.1063/1.2214695. URL http://link.aip.org/link/?RSI/77/103504/1.

[14] A. Lohs, K. Behler, K. Lddecke, and G. Raupp. The ASDEX upgrade UTDC and DIO cards–a family of PCI/cPCI devices for real-time DAQ under Solaris. *Fusion Engineering and Design*, 81(15-17):1859 – 1862, 2006. ISSN 0920-3796. doi: DOI:10.1016/j.fusengdes.2006.04.062. URL http://www.sciencedirect.com/science/

article/B6V3C-4K5JVT7-2/2/cf21b6f63a04525d1fe7be7cfca7b365. 5th IAEA TM on Control, Data Acquisition, and Remote Participation for Fusion Research - 5th IAEA TM.

[15] S. Palazzo, A. Murari, G. Vagliasindi, P. Arena, D. Mazon, A. De Maack, and JET-EFDA Contributors. Image processing with cellular nonlinear networks implemented on field-programmable gate arrays for real-time applications in nuclear fusion. *Review of Scientific Instruments*, 81(8):083505, 2010. doi: 10.1063/1.3477994. URL http://link.aip.org/link/?RSI/81/083505/1.

[16] Jeremy M. Hanson, Bryan De Bono, Royce W. James, Jeffrey P. Levesque, Michael E. Mauel, David A. Maurer, Gerald A. Navratil, Thomas Sunn Pedersen, and Daisuke Shiraki. Feedback suppression of rotating external kink instabilities in the presence of noise. *Physics of Plasmas*, 15, 2008.

[17] J. M. Hanson, A. J. Klein, M. E. Mauel, D. A. Maurer, G. A. Navratil, and T. Sunn Pedersen. A digital control system for external magnetohydrodynamic modes in tokamak plasmas. *Review of Scientific Instruments*, 80, 2009.

[18] G. Naylor. Synchronization of Thomson scattering measurements on MAST using an FPGA based “Smart” trigger unit. *Review of Scientific Instruments*, 81(10): 10E110, 2010. doi: 10.1063/1.3479120. URL http://link.aip.org/link/?RSI/81/10E110/1.

[19] Y. Kawamata, O. Naito, K. Kiyono, K. Itami, T. Totsuka, H. Akasaka, M. Sueoka, T. Sato, T. Oshima, S. Sakata, M. Sato, H. Takenaga, T. Suzuki, N. Oyama, M. Takechi, T. Ozeki, Y. Kamada, and K. Kurihara. Design study of the JT-60SA supervisory control system. *Fusion Engineering and Design*, 83(2-3): 198 – 201, 2008. ISSN 0920-3796. doi: DOI:10.1016/j.fusengdes.2007.12.014. URL http://www.sciencedirect.com/science/article/B6V3C-4RTCPS4-2/2/a0357b90ac20e2c4f7f8cd8b30035212. Proceedings of the 6th IAEA Technical Meeting on Control, Data Acquisition, and Remote Participation for Fusion Research.

[20] M. Mitri, D. Nicolai, O. Neubauer, H.T. Lambertz, I. Schmidt, A. Khilchenko, B. Schweer, U. Maier, and U. Samm. Optimised plasma stabilisation at TEXTOR with an advanced, real-time digital control scheme. *Fusion Engineering and Design*, 84(7-11):1329 – 1332, 2009. ISSN 0920-3796. doi: DOI:10.1016/j.fusengdes.2009.02.039. URL http://www.sciencedirect.com/science/article/B6V3C-4VXJVYN-2/2/f4923af049590e79c75938993ee31f12. Proceeding of the 25th Symposium on Fusion Technology - (SOFT-25).

[21] Yichun Wu, Lingzhi Wang, Jiarong Luo, Zhenshan Ji, Xiaoyang Sun, and Yong Wang. Upgrading of the EAST distributed synchronization and timing system. *Nuclear Science, IEEE Transactions on*, 57(3):1522 –1527, 2010. ISSN 0018-9499. doi: 10.1109/TNS.2010.2045897.

[22] L. Esteban, M. Sánchez, J.A. López, O. Nieto-Taladriz, and J. Sánchez. Continuous plasma density measurement in TJ-II infrared interferometer - Advanced signal processing based on FPGAs. *Fusion Engineering and Design*, 85(3-4):328 – 331, 2010. ISSN 0920-3796. doi: 10.1016/j.fusengdes.2010.03.036. URL `http://www.sciencedirect.com/science/article/pii/S0920379610001079`. ¡ce:title¿Proceedings of the 7th IAEA Technical Meeting on Control, Data Acquisition, and Remote Participation for Fusion Research¡/ce:title¿.

[23] PR Alvarez, M Cattin, J Lewis, J Serrano, and T Wlostowski. FPGA mezzanine cards for CERNs accelerator control system. oai:cds.cern.ch:1215572. Technical Report CERN-ATS-2009-097, CERN, Geneva, Nov 2009.

[24] I. Balboa, B. Huang, G. Naylor, M. Walsh, A. Sirinelli, P. Parsons, J. Fessey, M. Townsend, M. Beurskens, N. Conway, J. Flanagan, M. Kempenaars, and A. Kirk. Laser beam combiner for Thomson scattering core LIDAR. *Review of Scientific Instruments*, 81(10):10D534, 2010. doi: 10.1063/1.3485081. URL `http://link.aip.org/link/?RSI/81/10D534/1`.

[25] M. J. Walsh, M. Beurskens, P. G. Carolan, M. Gilbert, M. Loughlin, A. W. Morris, V. Riccardo, Y. Xue, R. B. Huxford, , and C. I. Walker. Design challenges and analysis of the ITER core LIDAR thomson scattering system. *Review of Scientific Instruments*, 77(10), 2006.

[26] J. Figueiredo, G. Naylor, M. Walsh, M. Dunstan, R. Scannell, and F. Serra. Mast yag thomson scattering upgrade alignment system. *Review of Scientific Instruments*, 81(10):10D521, 2010. doi: 10.1063/1.3475377. URL `http://link.aip.org/link/?RSI/81/10D521/1`.

[27] Hannes Alfvén. Existence of electromagnetic-hydrodynamic waves. *Nature*, 150:405–406, 1942.

[28] D. Tsiklauri and V. M. Nakariakov. Wide-spectrum slow magnetoacoustic waves in coronal loops. *Astronomy and Astrophysics*, 379:1106–1112, December 2001. doi: 10.1051/0004-6361:20011378.

[29] W. W. Heidbrink. Basic physics of Alfvén instabilities driven by energetic particles in toroidally confined plasmas. *Physics of Plasmas*, 15(5):055501, 2008. doi: 10.1063/1.2838239. URL `http://link.aip.org/link/?PHP/15/055501/1`.

[30] H A Holties, J P Goedbloed, G T A Huysmans, and W Kerner. Dependence of the mhd spectrum on the safety factor profile. *Plasma Physics and Controlled Fusion*, 39(1):73, 1997. URL `http://stacks.iop.org/0741-3335/39/i=1/a=005`.

[31] D. Testa, A. Fasoli, E. Solano, and JET-EFDA Contributors. Diagnosis and study of alfvén eigenmodes stability in JET (invited). *Review of Scientific Instruments*, 74 (3):1694–1700, 2003. doi: 10.1063/1.1534920. URL `http://link.aip.org/link/?RSI/74/1694/1`.

[32] Neil F. Cramer. *The Physics of Alfvén Waves*. John Wiley and Sons, 2011.

[33] S. D. Pinches, H. L. Berk, D. N. Borba, B. N. Breizman, A. Fasoli S. Briguglio, G. Fogaccia, M. P. Gryaznevich, V. Kiptily, S. E. Sharapov M. J. Mantsinen, D. Testa, R. G. L. Vann, G. Vlad, F. Zonca, and JET-EFDA Contributors. The role of energetic particles in fusion plasmas. *Plasma Physics and Controlled Fusion*, 46:B187–B200, 2004.

[34] Simon Pinches. *Nonlinear Interaction of Fast Particles with Alfvén Waves in Tokamaks*. PhD thesis, University of Nottingham, 1996.

[35] K. L. Wong, R. J. Fonck, S. F. Paul, D. R. Roberts, E. D. Fredrickson, R. Nazikian, H. K. Park, M. Bell, N. L. Bretz, R. Budny, S. Cohen, G. W. Hammett, F. C. Jobes, D. M. Meade, S. S. Medley, D. Mueller, Y. Nagayama, D. K. Owens, and E. J. Synakowski. Excitation of toroidal Alfvén eigenmodes in TFTR. *Phys. Rev. Lett.*, 66:1874–1877, Apr 1991. doi: 10.1103/PhysRevLett.66.1874. URL `http://link.aps.org/doi/10.1103/PhysRevLett.66.1874`.

[36] S.D. Pinches, L.C. Appel, J. Candy, S.E. Sharapov, H.L. Berk, D. Borba, B.N. Breizman, T.C. Hender, K.I. Hopcraft, G.T.A. Huysmans, and W. Kerner. The {HAGIS} self-consistent nonlinear wave-particle interaction model. *Computer Physics Communications*, 111(1-3):133 – 149, 1998. ISSN 0010-4655. doi: http://dx.doi.org/10.1016/S0010-4655(98)00034-4. URL `http://www.sciencedirect.com/science/article/pii/S0010465598000344`.

[37] S. E. Sharapov. Toroidal alfvén eigenmodes and fast particles in tokamaks. *Fusion Science and Technology*, 61(2T):104–112, February 2012. URL `http://www.new.ans.org/pubs/journals/fst/a_9406`.

[38] Ph. Lauber, I.G.J. Classen, D. Curran, V. Igochine, B. Geiger, S. da Graça, M. García-Mu noz, M. Maraschek, P. McCarthy, and the ASDEX Upgrade Team. Nbi-driven alfvénic modes at asdex upgrade. *Nuclear Fusion*, 52(9):094007, 2012. URL `http://stacks.iop.org/0029-5515/52/i=9/a=094007`.

[39] S. E. Sharapov. Fast particle driven alfvén eigenmodes in tokamaks. *Fusion Science and Technology*, 57(2T):156–163, February 2010. URL http://www.new.ans.org/pubs/journals/fst/a_9406.

[40] R. S. Hemsworth, A. Tanga, and V. Antoni. Status of the iter neutral beam injection system (invited). *Review of Scientific Instruments*, 79(2):02C109, 2008. doi: 10.1063/1.2814248. URL http://link.aip.org/link/?RSI/79/02C109/1.

[41] K Appert, R Gruber, F Troyuon, and J Vaclavik. Excitation of global eigenmodes of the alfvén wave in tokamaks. *Plasma Physics*, 24(9):1147, 1982. URL http://stacks.iop.org/0032-1028/24/i=9/a=010.

[42] C. E. Kieras and J. A. Tataronis. The shear Alfvén continuous spectrum of axisymmetric toroidal equilibria in the large aspect ratio limit. *Journal of Plasma Physics*, 28:395, December 1982. doi: 10.1017/S0022377800000386.

[43] G. Y. Fu and C. Z. Cheng. Theory of a high-n toroidicity-induced shear alfvén eigenmode in tokamaks. *Physics of Fluids B: Plasma Physics*, 2(5):985–993, 1990. doi: 10.1063/1.859245. URL http://link.aip.org/link/?PFB/2/985/1.

[44] M. Brix, N. C. Hawkes, A. Boboc, V. Drozdov, S. E. Sharapov, and JET-EFDA Contributors. Accuracy of EFIT equilibrium reconstruction with internal diagnostic information at JET. *Review of Scientific Instruments*, 79(10):10F325–10F325–4, 2008. ISSN 0034-6748. doi: 10.1063/1.2964180.

[45] J. A. Snipes, N. Basse, C. Boswell, E. Edlund, A. Fasoli, N. N. Gorelenkov, R. S. Granetz, L. Lin, Y. Lin, R. Parker, M. Porkolab, J. Sears, S. Sharapov, V. Tang, and S. Wukitch. Active and fast particle driven alfvén eigenmodes in alcator c-mod. *Physics of Plasmas*, 12(5):056102, 2005. doi: 10.1063/1.1865012. URL http://link.aip.org/link/?PHP/12/056102/1.

[46] H.T. Kim and A.C.C. Sips. *Criterion for Plasma Burn-through in Tokamaks*. EFDA, 2012. URL http://books.google.co.uk/books?id=pvwUkgEACAAJ.

[47] V. Shevchenko, G. Cunningham, A. Gurchenko, E. Gusakov, B. Lloyd, M. O'Brien, A. Saveliev, A. Surkov, F. Volpe, and M. Walsh. Development of electron bernstein wave research in MAST. *Fusion science and technology*, 52(2):202–215, 2007. ISSN 1536-1055. URL http://cat.inist.fr/?aModele=afficheN&cpsidt=19013899.

[48] V.F. Shevchenko, M.R. O'Brien, D. Taylor, A.N. Saveliev, and MAST team. Electron Bernstein wave assisted plasma current start-up in MAST. *Nuclear Fusion*, 50 (2):022004, 2010. URL http://stacks.iop.org/0029-5515/50/i=2/a=022004.

[49] M. Brambilla. Slow-wave launching at the lower hybrid frequency using a phased waveguide array. *Nuclear Fusion*, 16(1):47, 1976. URL `http://stacks.iop.org/0029-5515/16/i=1/a=005`.

[50] J.A. Wesson and A. Sykes. Tokamak beta limit. *Nuclear Fusion*, 25(1):85, 1985. URL `http://stacks.iop.org/0029-5515/25/i=1/a=008`.

[51] Alan Sykes. High beta produced by neutral beam injection in the start (small tight aspect ratio tokamak) spherical tokamak. *Physics of Plasmas*, 4(5):1665–1671, 1997. doi: 10.1063/1.872271. URL `http://link.aip.org/link/?PHP/4/1665/1`.

[52] V Erckmann and U Gasparino. Electron cyclotron resonance heating and current drive in toroidal fusion plasmas. *Plasma Physics and Controlled Fusion*, 36(12): 1869, 1994. URL `http://stacks.iop.org/0741-3335/36/i=12/a=001`.

[53] A.G. Litvak, E.V. Suvorov, and M.D. Tokman. On the possibility of current drive in tokamaks by bernstein modes. *Physics Letters A*, 188(1):64 – 67, 1994. ISSN 0375-9601. doi: http://dx.doi.org/10.1016/0375-9601(94)90118-X. URL `http://www.sciencedirect.com/science/article/pii/037596019490118X`.

[54] Heinrich Peter Laqua. Electron bernstein wave heating and diagnostic. *Plasma Physics and Controlled Fusion*, 49(4):R1, 2007. URL `http://stacks.iop.org/0741-3335/49/i=4/a=R01`.

[55] Francesco Volpe. *Electron Bernstein emission diagnostic of electron temperature profile at W7-AS Stellarator*. PhD thesis, University of Greifswald, 2003.

[56] J. A. Tataronis and F. W. Crawford. Cyclotron harmonic wave propagation and instabilities: I. perpendicular propagation. *Journal of Plasma Physics*, 4:231–248, 5 1970. ISSN 1469-7807. doi: 10.1017/S0022377800004979. URL `http://journals.cambridge.org/article_S0022377800004979`.

[57] J. Preinhaelter and V. Kopecký. Penetration of high-frequency waves into a weakly inhomogeneous magnetized plasma at oblique incidence and their transformation to bernstein modes. *Journal of Plasma Physics*, 10:1–12, 7 1973. ISSN 1469-7807. doi: 10.1017/S0022377800007649. URL `http://dx.doi.org/10.1017/S0022377800007649`.

[58] E. Mjølhus. Coupling to z mode near critical angle. *Journal of Plasma Physics*, 31:7–28, 1 1984. ISSN 1469-7807. doi: 10.1017/S0022377800001392. URL `http://dx.doi.org/10.1017/S0022377800001392`.

[59] F. R. Hansen, J. P. Lynov, C. Maroli, and V. Petrillo. Full-wave calculations of the o-x mode conversion process. *Journal of Plasma Physics*, 39:319–337, 4 1988. ISSN

1469-7807. doi: 10.1017/S0022377800013064. URL `http://journals.cambridge.org/article_S0022377800013064`.

[60] Simon Freethy. *Synthetic aperture imaging of B-X-O mode conversion*. PhD thesis, York Plasma Institute, University of York, 2012.

[61] M. Born and E. Wolf. *Principles of Optics 6th Ed.* Pergamon Press, 1986.

[62] B.K. Huang, R.G.L. Vann, S. Freethy, R.M. Myers, G. Naylor, R.M. Sharples, and V.F. Shevchenko. Fpga-based embedded linux technology in fusion: The mast microwave imaging system. *Fusion Engineering and Design*, 87(12):2106 – 2111, 2012. ISSN 0920-3796. doi: 10.1016/j.fusengdes.2012.06.004. URL `http://www.sciencedirect.com/science/article/pii/S0920379612003079`. ¡ce:title¿Proceedings of the 8th IAEA Technical Meeting on Control, Data Acquisition, and Remote Participation for Fusion Research¡/ce:title¿.

[63] R. Hanbury Brown and R. Q. Twiss. Interferometry of the intensity fluctuations in light. i. basic theory: The correlation between photons in coherent beams of radiation. *Proceedings of the Royal Society of London. Series A. Mathematical and Physical Sciences*, 242(1230):300–324, 1957. doi: 10.1098/rspa.1957.0177. URL `http://rspa.royalsocietypublishing.org/content/242/1230/300.abstract`.

[64] R. Hanbury Brown and R. Q. Twiss. Interferometry of the intensity fluctuations in light ii. an experimental test of the theory for partially coherent light. *Proceedings of the Royal Society of London. Series A. Mathematical and Physical Sciences*, 243(1234):291–319, 1958. doi: 10.1098/rspa.1958.0001. URL `http://rspa.royalsocietypublishing.org/content/243/1234/291.abstract`.

[65] P.H van Cittert. Die wahrscheinliche schwingungsverteilung in einer von einer lichtquelle direkt oder mittels einer linse beleuchteten ebene. *Physica*, 1(1-6):201 – 210, 1934. ISSN 0031-8914. doi: 10.1016/S0031-8914(34)90026-4. URL `http://www.sciencedirect.com/science/article/pii/S0031891434900264`.

[66] F. Zernike. The concept of degree of coherence and its application to optical problems. *Physica*, 5(8):785 – 795, 1938. ISSN 0031-8914. doi: 10.1016/S0031-8914(38)80203-2. URL `http://www.sciencedirect.com/science/article/pii/S0031891438802032`.

[67] M. Daniel. Towards the intensity interferometry stellar imaging system. *arXiv*, 2009.

[68] B.E. Zhilyaev. Bispectral technique for reconstruction the astronomical images with an intensity interferometer. *arXiv*, 2008.

[69] J. C. Dainty and J. R. Fienup. *Phase retrieval and image reconstruction for astronomy*. Academic Press, 1987.

[70] Hideya Gamo. Triple correlator of photoelectric fluctuations as a spectroscopic tool. *Journal of Applied Physics*, 34(4):875–876, 1963. doi: 10.1063/1.1729553. URL http://link.aip.org/link/?JAP/34/875/1.

[71] A.W. Lohmann and B. Wirnitzer. Triple correlations. *Proceedings of the IEEE*, 72 (7):889 – 901, july 1984. ISSN 0018-9219. doi: 10.1109/PROC.1984.12946.

[72] Takuso Sato, Shusou Wadaka, Jiro Yamamoto, and Junichi Ishii. Imaging system using an intensity triple correlator. *Appl. Opt.*, 17(13):2047–2052, Jul 1978. doi: 10.1364/AO.17.002047. URL http://ao.osa.org/abstract.cfm?URI=ao-17-13-2047.

[73] H. Bartelt, A. W. Lohmann, and B. Wirnitzer. Phase and amplitude recovery from bispectra. *Appl. Opt.*, 23(18):3121–3129, Sep 1984. doi: 10.1364/AO.23.003121. URL http://ao.osa.org/abstract.cfm?URI=ao-23-18-3121.

[74] Paul Nu nez. *Towards Optical Intensity Interferometry For High Angular Resolution Stellar Astrophysics*. PhD thesis, The University of Utah, 2012.

[75] R. B. Holmes and Mikhail S. Belen'kii. Investigation of the cauchy–riemann equations for one-dimensional image recovery in intensity interferometry. *J. Opt. Soc. Am. A*, 21(5):697–706, May 2004. doi: 10.1364/JOSAA.21.000697. URL http://josaa.osa.org/abstract.cfm?URI=josaa-21-5-697.

[76] R. B. Holmes, S. Lebohec, and P. D. Nu nez. Two-dimensional image recovery in intensity interferometry using the cauchy-riemann relations. volume 7818, page 78180O. SPIE, 2010. doi: 10.1117/12.858438. URL http://link.aip.org/link/?PSI/7818/78180O/1.

[77] H. Jensen, D. Dravins, S. Lebohec, and P. D. Nuñez. Stellar intensity interferometry: optimizing air Cherenkov telescope array layouts. In *Society of Photo-Optical Instrumentation Engineers (SPIE) Conference Series*, volume 7734 of *Society of Photo-Optical Instrumentation Engineers (SPIE) Conference Series*, July 2010. doi: 10.1117/12.856412.

[78] T. O'Gorman, G. Naylor, K. J. Gibson, B. Huang, G. J. McArdle, R. Scannell, S. Shibaev, J. A. Snape, and N. Thomas-Davies. A field programmable gate array unit for the diagnosis and control of neoclassical tearing modes on mast. *Review of Scientific Instruments*, 83(10):10E312, 2012. doi: 10.1063/1.4732057. URL http://link.aip.org/link/?RSI/83/10E312/1.

[79] H. Zohm, G. Gantenbein, G. Giruzzi, S. Gunter, F. Leuterer, M. Maraschek, J. Meskat, A.G. Peeters, W. Suttrop, D. Wagner, M. Zabiego, ASDEX Upgrade Team, and ECRH Group. Experiments on neoclassical tearing mode stabilization by ECCD in ASDEX Upgrade. *Nuclear Fusion*, 39(5), 1999.

[80] H. Zohm, G. Gantenbein, A. Gude, S. Gunter, F. Leuterer, M. Maraschek, J.P. Meskat, W. Suttrop, Q. Yu, ASDEX Upgrade Team, and ECRH Group (AUG). The physics of neoclassical tearing modes and their stabilization by ECCD in ASDEX Upgrade. *Nuclear Fusion*, 41, 2001.

[81] V. Svoboda, B. Huang, J. Mlynar, G. Pokol, J. Stockel, and G. Vondrasek. Multi-mode remote participation on the GOLEM tokamak. *Fusion Engineering and Design, accepted.*, 2011.

[82] B.K. Huang, R.M. Myers, R.M. Sharples, G. Cunningham, G.A. Naylor, O. Goudard, J.J. Harrison, and R.G.L. Vann. Embedded Linux on FPGA instruments for control interface and remote management. 2011.

[83] B.K. Huang, G.A. Naylor, R.M. Myers, R.M. Sharples, N. Ben Ayed, G. Cunningham, A. Field, and S. Khilar R.G.L. Vann. FPGA based hardware instrumentation development on MAST. 2011.

[84] V F Shevchenko, R G L Vann, S J Freethy, and B K Huang. Synthetic aperture microwave imaging with active probing for fusion plasma diagnostics. *Journal of Instrumentation*, 7(10):P10016, 2012. URL `http://stacks.iop.org/1748-0221/7/i=10/a=P10016`.